DISSERTATION

Study of a Positron Emission Mammograph

ausgeführt zum Zwecke der Erlangung des akademischen Grades eines Doktors der technischen Wissenschaften unter der Leitung von

Univ. Prof. Dr. Christian Fabjan
Atominstitut der Österreichischen Universitäten (E141)

eingereicht an der Technischen Universität Wien
Technisch-Naturwissenschaftliche Fakultät

von

Dipl.-Ing. Julia Trummer
Matr.Nr. 9625630
Axerweg 49
A - 7000 Eisenstadt

Diese Arbeit wurde unterstützt vom Österreichischen Bundesministerium für Bildung, Wissenschaft und Kultur

Genf, am 21. Feber 2007

in loving memory
of my grandfather

Kurzfassung

Brustkrebs ist gegenwärtig eine der häufigsten Todesursachen bei Frauen. Bei jeder achten Frau wird im Laufe ihres Lebens mindestens einmal ein Tumor in der Brust diagnostiziert. Früherkennung ist ausschlaggebend für Genesung und Überleben der Patientin; deshalb ist es notwendig, ein Untersuchungsmethode mit hoher Ortsauflösung und Effizienz zur Verfügung zu haben.

In dieser Doktorarbeit werden zwei Aspekte eines speziell zur Mammographie bestimmten Positronenemissionstomographen behandelt, dem von der Crystal Clear Collaboration entwickelten ClearPEM.
Der erste Teil dieser Arbeit befasst sich mit den experimentiellen Versuchen mit Szintillationskristallen, die den aktiven Bestandteil des Detektors darstellen. Der zweite Teil beschäftigt sich mit Computersimulationen sowohl des aktuellen Designs eines kompletten Systems als auch mögliche zukünftige Erweiterungen der Maschine, z.B. einer Kombination des Mammographen mit einer Ultraschallsonde oder einem Vetozähler kombiniert werden.

Die entscheidenden Punkte zur Erreichung exzellenter Detektorleistung sind die Qualität der verwendeten Szintillatorkristalle und deren Eigenschaften, die der Anwendung angepasst sein müssen. Um die Szintillationseigenschaften verschiedener Kristalle zu verbessern, ist es wichtig diese Eigenschaften und ihre zugrunde liegenden Mechanismen besser zu verstehen. Das beinhaltet auch äußere Einflüsse des Produktionsprozesses. Die Materialien dreier verschiedener Produzenten werden in Bezug auf Lichtausbeute, Abklingzeit und Transmission miteinander verglichen. Das nichtproportionale Energieverhalten und die intrinsische Energieauflösung werden ebenfalls abgehandelt.
Zusätzlich zu den schon erwähnten Eigenschaften spielt bei den Kristallen, die im ClearPEM Verwendung finden, noch eine weitere Eigenschaft eine wichtige Rolle, nämlich die Ortsauflösung der Wechselwirkungstiefe des Gammaphotons im Kristall. Zwei Szintillationsmaterialien wurden daraufhin getestet, ob mit ihnen die erforderliche Auflösung der Wechselwirkungstiefe erreicht werden kann. Auch der Einfluss der Beschaffenheit der Kristalloberfläche wird untersucht.

Die Positronenemissionstomographie besitzt zwei nicht unwesentliche Einschränkungen: Erstens können bei dieser Technik keine anatomischen Strukturen dargestellt werden, nur Informationen über den Zellstoffwechsel werden wiedergegeben. Um diese Hürde zu überwinden soll eine Ultraschallsonde in das ClearPEM-system integriert werden. Zweitens kommt es durch die Anreicherung der anderen Organe des Körpers mit dem radioaktiven Indikator zu einer erhöhten Rate zufälliger Koinzidenzen im Detektor. Vor allem Tumore in der Nähe der Brustwand und damit des Herzens können dadurch übersehen werden. Eine mögliche Lösung des Problems brächte ein Vetozähler oberhalb des Rückens der Patientin. In einer Reihe von Monte Carlo Simulationen lassen sich die positiven und negativen Aspekte notwendiger Änderungen der Detektorgeometrie erkennen, die der Einbau eines Ultraschallgerätes oder eines Vetozählers mit sich bringen würden.

Abstract

Today breast cancer is among the most common causes of death for women. One in eight women will develop a tumour in her breast at least once in her lifetime. An early detection of the cancer is crucial to the patient's survival and recovery. For early detection it is necessary to have an instrument with high spatial resolution and efficiency.

The scope of this thesis is two aspects of a dedicated PET scanner for mammography developed by the Crystal Clear Collaboration, the ClearPEM.
The first half of the thesis deals with the experimental work on scintillation crystals which constitute the main part of the detector. The second part looks into the design of the whole system and the possibility of future enhancements by adding an ultrasound probe and /or a veto-counter. The effects of these changes are studied by employing simulation tools.

The key to excellent detector performance is to use scintillation crystals with properties best matched to the requirements of a given application. To better understand the scintillation characteristics of the crystals, how they are influenced by their production history and how to improve their properties, this study compares scintillation materials of three producers in respect to light yield, decay time and transmission characteristics. The non-proportional response to different photon energies and the intrinsic energy resolution of the scintillation crystals is also studied.
In addition to the already mentioned properties scintillation crystals for the ClearPEM detector have to be able to resolve the position of the interaction of the photon in the crystal with high precision. Two different scintillation materials are studied with the objective of reaching the necessary depth of interaction resolution. The influence of the surface condition on the depth of interaction resolution is also examined.

Two major constraints exist in PET imaging. A PET image shows only the metabolism of the cells in the patient, no morphological information can be obtained. For this purpose an ultrasound probe is going to be integrated into the ClearPEM system. The second issue is organ activity, which is especially relevant in breast imaging because of the closeness of the region of interest to the heart. This is the main source for random coincidences. A veto counter on the patient's back is proposed to reduce the random coincidence rate. A series of Monte Carlo simulations was performed which show the negative and positive changes in sensitivity caused by changes in the scanner geometry necessary to implement the ultrasound probe and random background reduction with the veto-counter.

Acknowledgements

First of all I would like to thank Prof. Christian Fabjan for giving me the opportunity to carry out my PhD at CERN and his constant support throughout my stay.

Sincere thanks are given to Paul Lecoq and Etiennette Auffray, my supervisors at CERN, for sharing their knowledge and ideas in many discussions. They never failed to encourage me when experiments did not again work or another core was dumped. Also Etiennette spent a lot of time correcting my thesis.
I am grateful to everyone from the CMS Ecal group, technicians and engineers and physicists alike, for welcoming me into their middle and helping out whenever I needed them.
In the same spirit I would like to thank my colleagues from the Crystal Clear Collaboration.
I want to thank all the other PhD and technical students, interns and summer students in my group, who became good friends and shared the joys and pains of physics with me, especially Cecile, for endless girl talk, Pepe, for many "kaffeenieren expeditions", Matthias, who not only shared an office with me but also the same kind of humour, Alessandro, who is better than any LaTeX book and last but not least everyone from the 10 o'clock coffee gang.
A big "thanks!" to Mike Lamont, Dave Barney and Richard Ecclestone who sacrificed their spare time to proofread two chapters of my thesis each and correct my English.

These past two and a half years have been a wonderful time for me owing to so many friends, old and new: all the Austrians with whom I never felt so far away from home, the many people from the climbing list, who showed great patience teaching me and passed their passion for mountains on to me.

I also want to express my gratitude to my parents for always believing in me and urging me on.

This last line belongs to a very special person, Fadmar, who is always there for me - despite myself.

Contents

Chapter 1

Introduction

"Physics technologies" have become an essential part of modern medicine. Contributions are made by various fields of physics, such as high energy physics, particle and detector physics, solid state physics, acoustics and even quantum mechanics.
Extensive imaging of the human anatomy started in the Renaissance but the first revolution for medical imaging was brought about by the discovery of X-rays by Röntgen in 1895 [1] and the discovery of radionuclides by Marie and Pierre Curie and Becquerel for nuclear medicine [2].
The progress in medical imaging went hand in hand with the advancements in experimental physics and computing. The discovery of the positron, scintillation radiation detectors and photomultiplier tubes, digital electronics and more and more powerful computers were important steps towards present day technologies. The second revolution began in 1972 with the introduction of the CAT (Computer Assisted Tomography) scanner by Hounsfield, now known as CT, which not only provides two dimensional reconstructed images but also better contrast between different tissues [3].

1.1 Thesis overview

The work described in this thesis was carried out at CERN as part of the Crystal Clear Collaboration. The aim was the evaluation of a new project - a dedicated positron emission tomography (PET) scanner for mammography. This thesis deals with the experimental work on scintillation crystals which constitute the main part of any PET detector and looks into the design of the whole system with the aim of evaluating possible future enhancements using Monte Carlo simulations (integration of an ultrasound probe and/or veto counter).

This thesis is organized as follows. After a short presentation of CERN and the Crystal Clear Collaboration (CCC), an introduction to medical imaging and positron emission tomography scanners in general, and the PET projects of the CCC in particular, is

given.The principles of scintillation and the main characteristics of scintillators are explained in Chapter 2. Chapter 3 describes the experimental techniques used to study scintillation materials. The results are presented and discussed in the following chapter. Chapter 5 gives an overview of the simulation software and other software tools employed to investigate the PEM scanner. Chapter 6 is dedicated to the results and conclusions drawn from the computer simulations. The thesis is summarized in the last chapter which gives also a short outlook of future CCC activities.

1.2 CERN, the LHC and CMS

CERN is the European Organization for Nuclear Research. It was created in 1954 to help re-establish Europe's leading role in physics. The laboratory was one of Europe's first joint ventures and now unites twenty Member states, eight Observer States and Organizations and twenty-eight Non-Member States. The current Member states are: Austria, Belgium, Bulgaria, Czech Republic, Denmark, Finland, France, Germany, Greece, Hungary, Italy, The Netherlands, Norway, Poland, Portugal, Slovak Republic, Spain, Sweden, Switzerland and The United Kingdom.

CERN exists primarily to provide European physicists with the tools to study elementary particles and their governing forces at unprecedented energies and look for new physics. The latest of these tools is the Large Hadron Collider (LHC) which has a planned start-up in 2007. This machine will collide proton beams with energies of 7-on-7 TeV and interaction rates of $6{\cdot}10^8$ collisions per second at the high luminosity interaction points. ALICE, ATLAS, CMS and LHCb are the four experiments. The high nominal luminosity of $10^{34}\mathrm{cm}^{-2}\mathrm{s}^{-1}$ makes challenging demands on the detectors. For

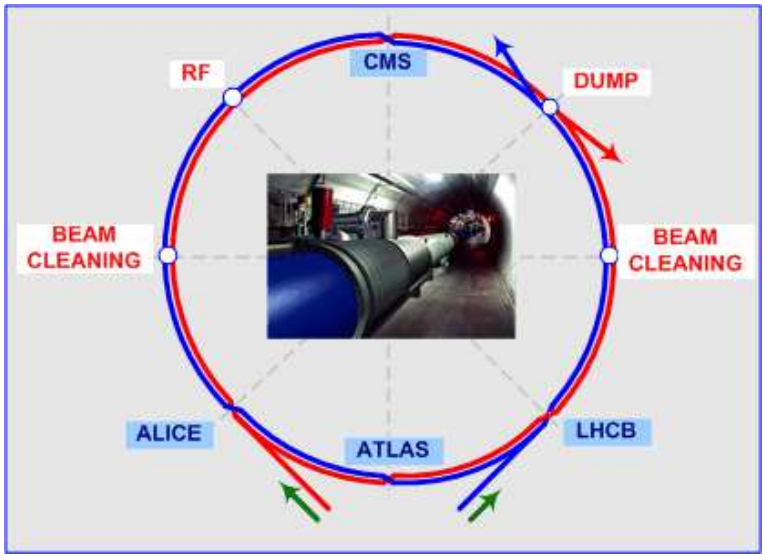

Figure 1.1: Schematic drawing of the LHC [4]

example, the CMS (Compact Muon Solenoid) experiment is using an electromagnetic calorimeter based on lead-tungstate (PWO) crystals equipped with avalanche photodiodes and electronics. The components have to operate in a magnetic field of 4 T, at a rate of 40 MHz (a time of 25 ns between bunch crossings) and withstand a radiation dose of 1 to 2 kGy/year.

To help meet this challenges the Crystal Clear Collaboration (CCC) was set up at CERN in 1990 to study and develop new scintillating materials suitable for the LHC [5]. The CCC works closely together with the Technology Transfer Department at CERN which helps protect the intellectual property, submit patents, establishes contacts with private companies, but also takes an active part in R&D.

1.3 Crystal Clear Collaboration

The Crystal Clear Collaboration was set-up as an interdisciplinary collaboration between material scientists, detector experts in high energy physics and more recently medical imaging groups. The CCC comprises research institutes from around the world. Its members are CERN, Forschungszentrum Jülich, the Institute of Nuclear Problems in Minsk, the Institute for Physical Research in Ashtarak, the Laboratório de Instrumentação e Física Experimental de Partículas (LIP) in Lisbon, Sungkyunkwan University School of Medicine in Seoul, the Université Claude Bernard in Lyon and the Vrije Universiteit Brussel (VUB) and a number of guest laboratories. Its goal was to develop new scintillator materials suitable for the challenging LHC operating environment, but also to perform fundamental research to better understand scintillation processes and explore new possible candidate materials for scintillation crystals.
Among the many achievements of the CCC are:

- an in-depth study of PWO to understand its scintillation and radiation damage mechanisms;
- to demonstrate the excellent properties of cerium fluoride (CeF_3) as a scintillator for high energy physics;
- the development of new scintillator materials: fluoride glasses, yttrium aluminate perovskite (YAP) and lutetium aluminate perovskite (LuAP) [6].

In 1995 the CCC shifted its main focus from high energy physics to applications for medical imaging. A small animal positron emission tomography (PET) scanner, the ClearPET^{TM} [7, 8], has been developed and is now commercially available through the German company Raytest GmbH[1].
Another project - the ClearPEM [9, 10] - deals with the development and construction of a dedicated PET scanner for mammography.

[1] Raytest GmbH, Benzstr. 4, 75339 Straubenhardt, Germany

The contribution of CERN to these projects lies in the profound knowledge of scintillation materials and new technologies developed for detectors for high energy physics experiments. The goal is to apply these technologies in medical imaging and to collaborate with industrial partners to use them in commercial PET scanners.

1.4 Positron Emission Tomography - PET

Positron emission tomography (PET) is a medical imaging technique that reveals a body's functions and not its anatomy. Although some PET devices have been around since 1950, Dr. Michael Phelps is considered as the inventor of the first PET brain camera in 1973 at Washington University in St. Louis [11, 12].

In a conventional set-up the patient lies on a bed in the centre of field of view (FOV) of one or more detector rings (Fig. 1.2). Usually, each detector consists of scintilla-

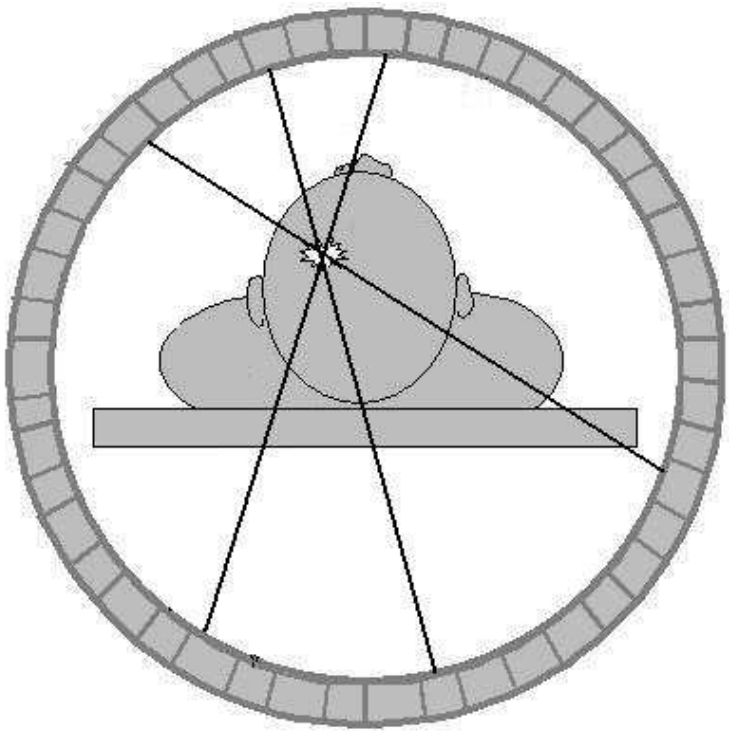

Figure 1.2: Conventional PET set-up - the patient lies in the centre of a ring of detectors

tion crystals which are read out by photomultiplier tubes (PMTs) connected to the electronics and data acquisition software which includes coincidence sorting and image reconstruction. Lately PMTs being replaced by avalanche photodiodes (APDs) in view of operating a PET in a magnetic field of a MRI (Magnetic Resonance Imaging).

Principle of PET imaging

A radioactive labelled organic molecule (tracer) is injected into the patient and left to accumulate in the body's tissue for approximately an hour. The distribution of the tracer in the body is mapped by the PET scanner. The most common tracer used in oncology nowadays is FluoroDeoxyGlucose (FDG), a sugar analogue labelled with the positron emitting radioisotope of fluorine F-18. Fast growing tumours exhibit a more elevated glucose metabolism than healthy tissue and accumulate a higher amount of the radioactive tracer. Thus they show up as an area of high FDG concentration in the PET image [13].
The positron annihilates with an electron in the body and two resulting 511 keV photons leave the body in opposite direction due to momentum conservation (if the positron is not at rest at the moment of annihilation the angle between the two photons is slightly different from 180° which is called acollinearity). When two detectors simultaneously detect one 511 keV photon each, a positron must have annihilated on a straight line connecting those two detectors. Such an event is called a coincidence and the line is the line of response (LOR) (Fig. 1.3 A). Each LOR is characterized by its angle of orientation ϕ with respect to the horizontal plane (parallel to the patient's bed in the gantry) and the shortest distance between the LOR and centre of the gantry s.
If for many LORs originating from one point the displacements s are plotted versus the angles the result is half a sine rotated 180° (Fig. 1.3 B). The exercise is repeated for all the points of the object. Thus a sinogram is constructed (Fig. 1.3 C). Each set of values in the sinogram for a given angle ϕ represent data collected from parallel LORs is called a projection [14, 15].

There are four possible types of coincidences: true, scattered, random (see Fig. 1.4(a)) and multiple coincidences.

true : A coincidence is referred to as true when both photons originate from the same positron, neither photon undergoes any kind of interaction before being detected and no other detection occurs in the same time window.

scattered : In the event of one or both of the two annihilation photons from the same positron scattering in the tissue, the recorded coincidence is called scattered.

random : When two photons from different sources hit the detectors in the time window a random coincidence is said to have taken place.

multiple : Three or more simultaneously detected photons in a given time window are called a multiple coincidence.

Image noise

True coincidences are the only desirable coincidences. Random and scattered coincidences lead to misidentification of LORs and hence to blurring of the reconstructed

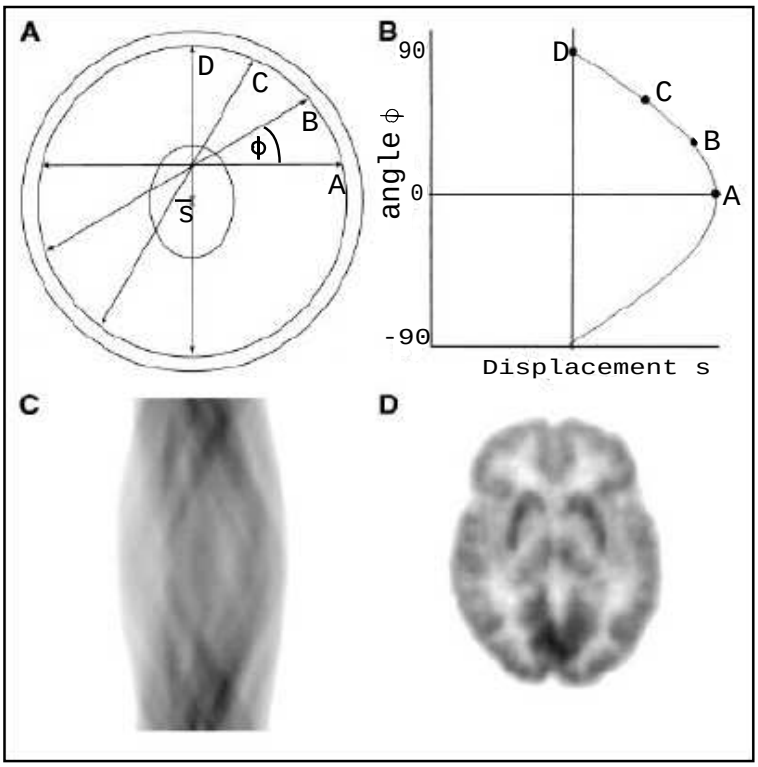

Figure 1.3: Sinogram formation and image reconstruction [14]

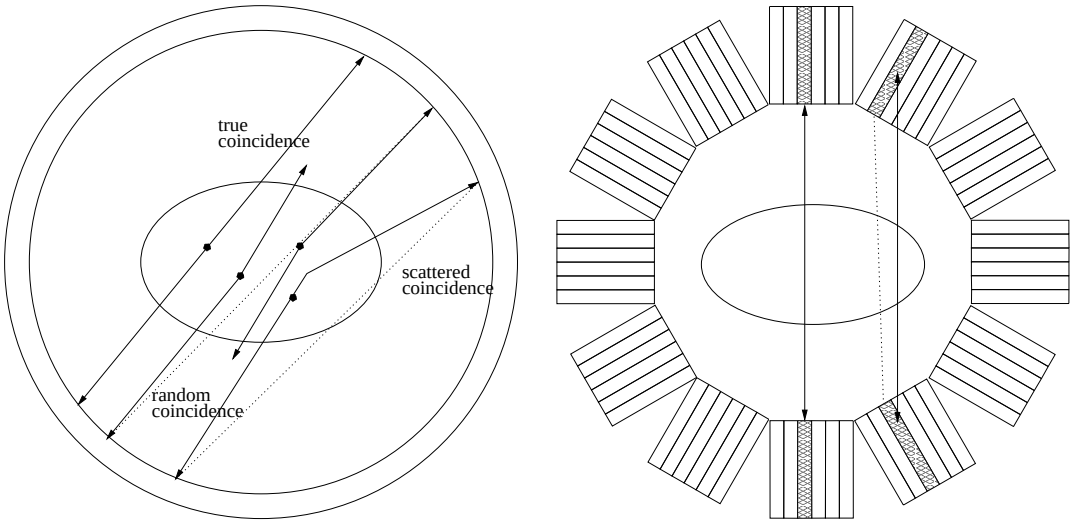

(a) (b)

Figure 1.4: Illustration of the different types of coincidences (a) and of parallax errors caused by positron annihilation far away from the centre of field of view (b)

image.
Random coincidences pose the biggest problem effecting the signal-to-noise ratio. Their number can be reduced by shielding the detectors from the rest of the body, by using an optimized injected dose value or by good timing properties of the system.
To avoid scattered events as much as possible an energy threshold is applied to the detectors. Multiple coincidences do not contribute to image noise because they are rejected a priori on the basis that at least two photons must result from different annihilation events.
Another error can arise from coincidences taking place at the margin of the FOV (Fig. 1.4b). When a photon does not impinge perpendicular on the crystal's surface but enters from an oblique angle it has a high probability to enter deeper into the crystal, traverse it with a negligible loss of energy and deposit most of its energy in a neighbouring crystal. A wrong detector position and consequently a false LOR is attributed to the two photons.
To overcome this problem several solutions have been proposed:

- the implementation of septa, where a septum is a thin band made from lead or tungstate that separate the crystal rings from each other and absorb photons which arrive askew.

- the determination the depth of interaction (DOI) of the photon in the crystal using two different types of scintillation crystals in a Phoswich combination.
  A Phoswich detector is a combination of two back-to-back scintillators with different properties, e.g. fast and slow decay time constants or different emission wavelengths. The signals from the individual pixels are electronically analysed to determine the crystal of interaction.

- via a light sharing technique in which one scintillator is read out at both ends and the difference in signal magnitude is used to calculate the DOI.

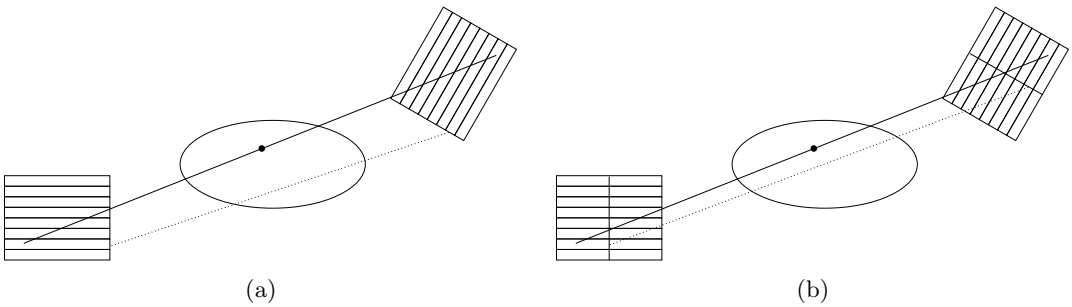

Figure 1.5: Illustration of the parallax error without information of the depth of interaction (a) and with information of the depth of interaction (b) using a Phoswich detector

PET scanners are used in various fields of medicine as well as in research. Clinical scanners are usually whole body PETs for diversified use. Medical applications can be found in cardiology to monitor the cardiac metabolism and blood flow; in neurology to

investigate epilepsy or strokes; and in oncology to search for tumours.
PETs are used in research on humans and animals alike to study brain activity or oxygen and glucose metabolism. In pharmacology and cancer research tests are typically performed on small animals like rats and mice. For this purpose dedicated small animal scanners were developed because the resolution of a whole body PET is too inaccurate for a mouse or rat [16].

1.5 Small animal imaging

Whole body PETs used in medicine have a spatial resolution of about 1 cm. This is mainly due to the coarse segmentation of the detector. Typically values of the cross section of the crystals used in whole-body PETs vary from 4x4 mm^2 to 10x10 mm^2. A better resolution is needed for small animal scanners used in pharmacology where new medication and cancer treatments are tested on rats and mice. Demands for high resolution small animal scanners opened up a new market and the Crystal Clear Collaboration decided to use their knowledge and expertise on the use of scintillating materials in HEP detectors to develop such a machine - the ClearPET^{TM}.

1.5.1 The ClearPET^{TM}

The ClearPET^{TM} is a high-resolution small animal PET scanner designed and built by the Crystal Clear Collaboration. Five different prototypes have been built [17]:

- the ClearPET^{TM} Neuro (Fig. 1.6), designed to perform brain studies on primates in a sitting position;
- the ClearPET^{TM} Rodent, a rodent version;
- PlanTIS for imaging plants;
- and two research prototypes with only a limited number of detector modules.

All are based on eight by eight crystal matrices of LSO and LuYAP crystals in a Phoswich combination coupled to a multi-anode photomultiplier tube. Such an arrangement is called a detector head. The crystal dimensions are either 2x2x10 mm^3 or 2x2x8 mm^3. Four detector heads, arranged in a line, build a module. Four modules together with the readout electronics are assembled in one cassette and twenty cassettes form four complete detector rings with a diameter of 120 mm. The gantry can rotate 360°. Free running ADCs are used to sample the signal from each photomultiplier continuously [20]. Events are stored in List Mode Format (LMF) [21] and are then sorted off-line into coincidences.
The ClearPET^{TM} has been commercialized by the German company Raytest GmbH, Straubenhardt, Germany. The commercial ClearPET^{TM} has a maximum sensitivity of

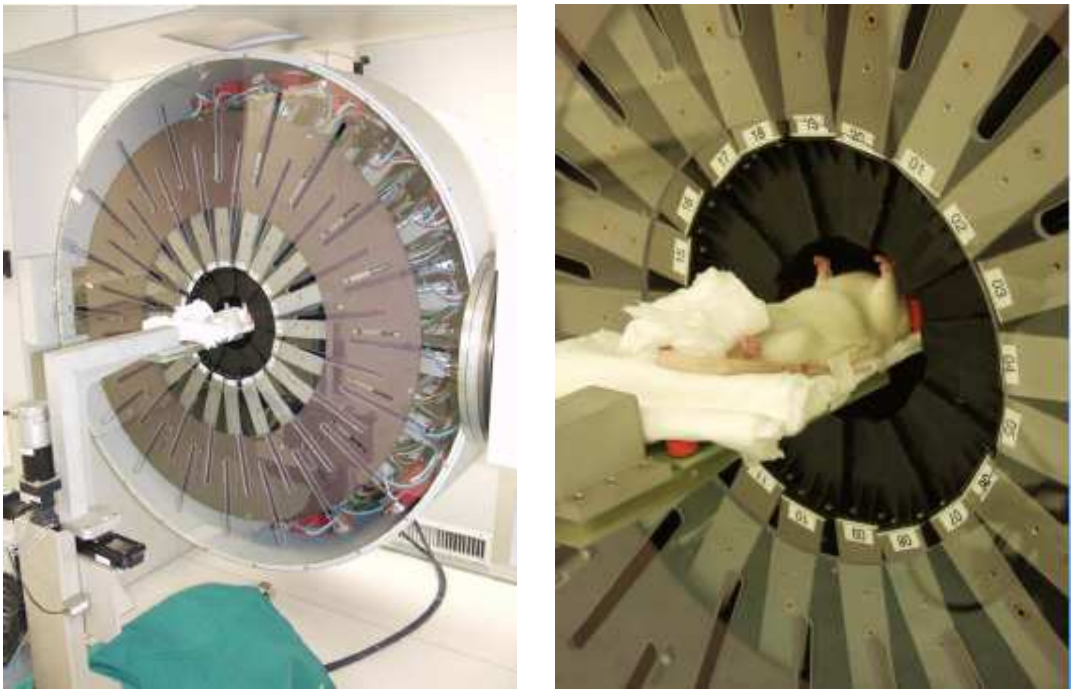

(a) (b)

Figure 1.6: Picture of the ClearPET^{TM} Neuro prototype Forschungszentrum Jülich (a) and detail (b) [18, 19]

3.8% at the centre of FOV. The FWHM spatial resolution ranges from 1.25 mm on axis to 2.0 mm at a point 3 cm off-axis [22]. The timing resolution is 5.7 ns at FWHM [23]. Fig. 1.7 shows one of the first images taken with the ClearPET^{TM} Neuro in Germany. The excellent spatial resolution allows to differentiate between various parts in the brain of a rat.

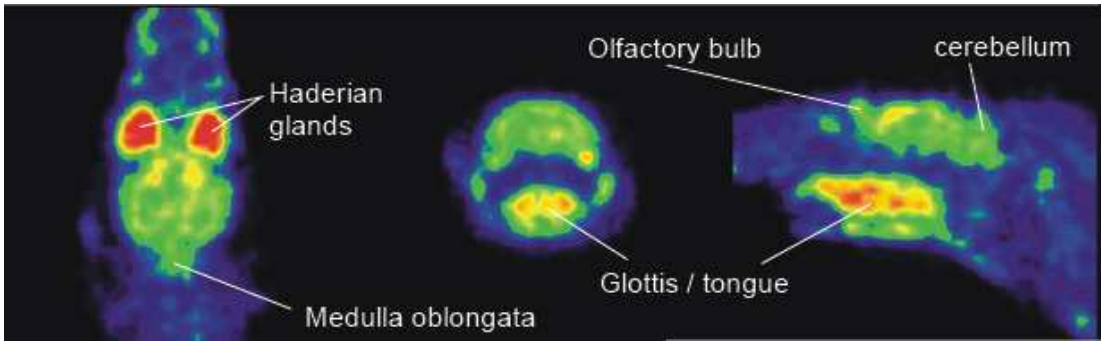

Figure 1.7: Reconstructed images from a rat scan taken with ClearPET^{TM} Neuro at Forschungszentrum Jülich [19]

1.6 Breast imaging

Early detection of breast cancer is vital, impacting critical on the chances of a success for the cure. X-ray mammography, ultrasound (US), magnetic resonance imaging, positron emission tomography, gamma camera imaging, sentinel lymph node imaging and computer tomography are some of the methods used to detect tumours in the breast. In all cases biopsies are made to confirm the diagnosis.
Each method has its own advantages and field of application. X-ray mammography is the common screening technique for all women over forty years of age. If a suspicious mass is found, an ultrasound is made to characterize the tissue of the lesion. High risk patients and patients whose physical characteristics cause insensitivity to X-ray mammography are examined further with MRI. PET is used to monitor therapy and detect recurring tumours [24].

Current limitations in breast imaging techniques are the high false diagnostics rate of X-ray mammography (30%) and the poor resolution of whole-body PETs. X-ray mammography is particularly limited in women with dense breast tissue (40% of the female population) or breast implants. If the tumour and the surrounding tissue are of the same density the tumour will not show up on a X-ray. The advantage of the a PET scanner over a X-ray scanner in the case of dense breast tissue is the different technique which is independent of variations of the tissue density.

These considerations led the Crystal Clear Collaboration to develop a prototype for a dedicated positron emission camera for mammography - the ClearPEM (PEM - Positron Emission Mammography). Motivated by the excellent spatial resolution the ClearPET^{TM} the CCC decided to aim for a clinical PET dedicated to mammography. A dedicated system is expected to have superior spatial resolution by using a smaller crystal size and finer detector segmentation, a higher sensitivity and therefore a shorter acquisition time because of the closeness to the region of interest, and, last but not least, it will use less material and be less expensive than a whole-body PET [9].

1.6.1 The ClearPEM

The ClearPEM is a PET imaging system dedicated to breast cancer diagnostics. At present the development of a prototype for a dedicated PET scanner for mammography, the ClearPEM is one of the main projects of the CCC, benefiting from the knowledge gained from the construction and commercialization of the ClearPET^{TM}. The advantage of a small dedicated machine is that it has a high spatial resolution using small pixels while still having low construction costs. High resolution enables the imaging of very small tumours, still in their early stages of growth when chances of cure are still high.
Fig. 1.8 is a view of the prototype model. The patient lies in a prone position on her stomach on the examination table. The table has an opening for the breast to pass

through. The scanner is mounted on a dedicated robotic system that allows the rotation of the detector heads around the breast and to change the configuration from a breast exam to an exam of the axilla region. The ClearPEM consists of two parallel

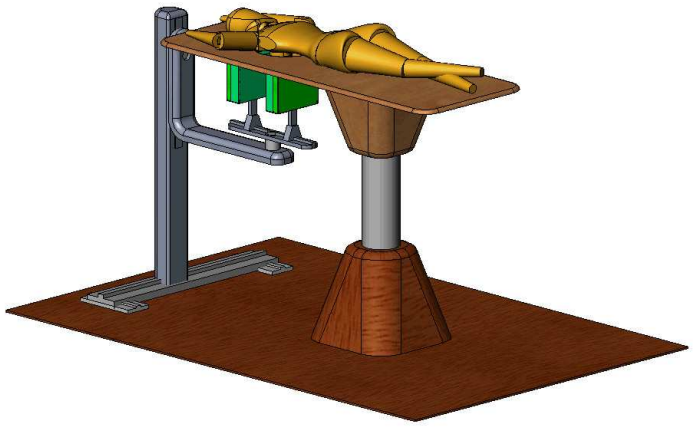

Figure 1.8: Schematic of the ClearPEM system

plates (17x15 cm^2) with 96 detector modules each rotating around the breast to allow 3D tomographic image reconstruction (Fig. 1.9 (a) and (b) show the design drawings of the plates and a detector module).
To achieve such a spatial resolution, small crystal pixels (2x2x20 mm^3) are chosen. The depth of interaction has to be known with a precision of at least 2 mm. The chosen method of DOI measurement is the light sharing method. The crystal is read out at both ends and the difference in light yield is used to determine the coordinate of the interaction along the length of the crystal (cf. 3.2).
$Lu_{2(1-x)}Y_{2x}SiO_5$:Ce (LYSO) crystals were chosen for the first ClearPEM prototype. LYSO is a dense material (7.1 g/cm^3) and thus gives large photon interaction probability and the detector can be kept compact. Moreover LYSO has a high light yield and fast decay time (40 ns) which fits the required timing resolution and expected count rates. Finally LYSO was widely commercially available at a reasonable price at the start of the project. Each module consists of a 4x8 crystal matrix of slightly depolished LYSO crystals optically isolated from each other and coupled on both sides to 32-pixel avalanche photo diodes (APDs) (its dimensions are shown in Fig. 1.10) [10]. A dedicated digital trigger and data acquisition system is used for on-line selection of coincidence events with high efficiency, large bandwidth and small dead time [25]. A short summary of the main ClearPEM requirements is given below:

- two plate system (17x15 cm^2) with rotation

- sensitivity: 10% at centre of FOV (plates 10 cm apart)
- spatial resolution: < 2 mm
- 6144 LYSO:Ce crystals (2x2x20 mm^3)
- 12288 APD channels
- low noise electronics: < 1000 e^- rms
- low power dissipation: 1 mW - 2 mW per channel
- event rate: singles 10 MHz, coincidences 1 MHz
- data rate: 200 Mb/s
- time resolution: 1 ns
- few percent dead time

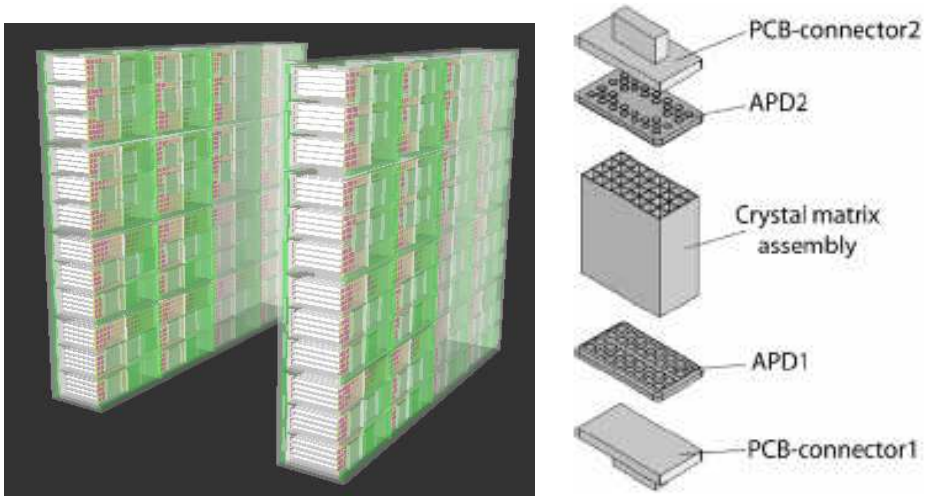

(a) (b)

Figure 1.9: Schematic of PEM detector plate (a) and PEM detector module (b)

The aim of the ClearPEM is to be sensitive to small tumours with a diameter of 2 mm to 3 mm in the breast and axilla region. One way to improve the image quality of the ClearPEM is to reduce the number of random coincidences. This could be done by mounting another detector above the patient's back and use it as a veto counter. A veto counter would reject all coincidence events in the ClearPEM that occur at the same time as an event in the veto counter. The evaluation of the performance of such a combined system is one of the topics of this thesis.

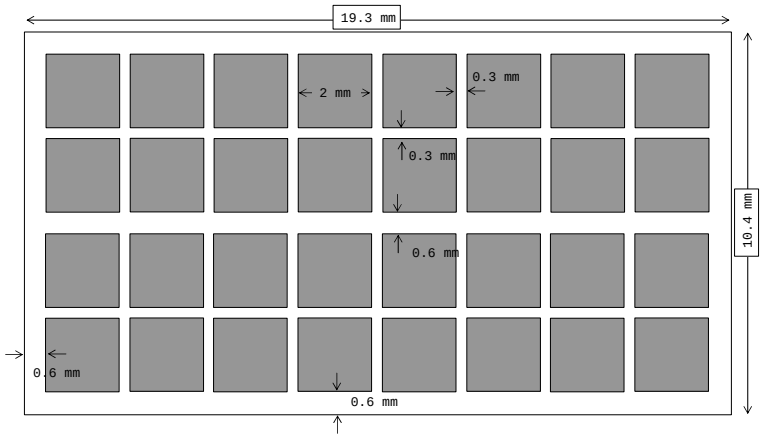

Figure 1.10: Dimension of a LYSO matrix

1.7 Multimodality

A new trend in medical imaging is to combine two different imaging techniques into one machine, e.g. PET/CT, PET/MRI, PET/US or PET/SPECT (SPECT - Single Photon Emission Computed Tomography). The idea of the first three combinations is to obtain morphological and functional images at the same time or shortly after one another with the patient still in the same position. Image fusion is made easier. Examination times and costs can be reduced as well. In a combined PET/SPECT system different radio tracers can be administered at the same time to monitor separate metabolisms or cell receptors.

1.7.1 The ClearPEM Sonic

Further improvement will result from combining metabolic information obtained by PET imaging with anatomical information. For the ClearPEM, ultrasonography is chosen as the means to this end, hence the name ClearPEM Sonic. This will improve diagnosis and follow up examinations. Moreover, this low dose system could in the future supersede conventional x-ray mammography for breast screening. Ultrasonography permits an anatomical reproduction of the breast with a spatial resolution of 0.5 mm. It does not require radioactive substances and is insensitive to the breast density. Together with PET mammography it helps in reducing the number of false-positive diagnoses. The ultrasound system has to be fully integrated in the PET mammography machine and operated completely automatically. Two different state-of-the-art devices for ultrasonography are being envisaged as part of the project:

- an next generation echograph capable of quantitatively mapping the elastic properties of the tissue. This system, designed by SuperSonic Imagine [26] is able

to generate a shear wave (by super fast focusing of longitudinal waves) in the medium and to measure the induced displacement of the tissue.

- a tomographic ultrasound system dedicated to breast imaging that allows 3D rendering of the uncompressed breast immersed in a water tank is under development by CNRS LMA [27].

Preparatory studies for an implementation of an ultrasound system in the ClearPEM are discussed later in this work.

Bibliography

[1] M.Hoheisel, Review of medical imaging with emphasis on X-ray detectors. Nucl Instr and Meth A563 (2006) 215. Martin Hoheisel

[2] R.Nutt, The History of Positron Emission Tomography. Molecular Imaging and Biology 4 (2002) 11. Ronald Nutt

[3] C.Guy, D.Ffytche, An Introduction to The Principles of Medical Imaging. London: Imperial College Press, 2000. 1-8.

[4] LHC machine outreach. http://lhc-machine-outreach.web.cern.ch/lhc-machine-outreach, Sept 2006.

[5] R&D proposal for the study of new fast and radiation hard scintillators for calorimetry at LHC, Crystal Clear Collaboration, project RD 18. CERN/DRDC/P27/91-15.

[6] The Crystal Clear Collaboration. http://crystalclear.web.cern.ch/crystalclear, Oct 2006.

[7] E.Auffray, P.Bruyndonckx, O.Devroede, A.Fedorov, U.Heinrichs, M.Korjik, M.Krieguer, C.Kuntner, C.Lartizien, P.Lecoq, S.Leonard, Ch.Morel, J.B.Mosset, Ch.Pedrini, A.Petrosian, U.Pietrzyk, M.Rey, S.Saladino, D.Sappey-Marinier, L.Simon, M.Streun, S.Tavernier, J.M.Vieira, K.Ziemons, The ClearPET project. Nucl Instr and Meth A 527 (2004) 171.

[8] K.Ziemons, A.Auffray, R.Barbier, G.Brandenburg, P.Bruyndonckx, Y.Choi, D.Christ, N.Costes, Y.Declais, O.Devroede, C.Dujardin, A.Fedorov, U.Heinrichs, M.Korjik, M.Krieguer, C.Kuntner, G.Largeron, C.Lartizien, H.Larue, P.Lecoq, S.Leonard, J.Marteau, Ch.Morel, J.B.Mosset, Ch.Parl, Ch.Pedrini, A.G.Petrosyan, U.Pietrzyk, M.Rey, S.Saladino, D.Sappey-Marinier, L.Simon, M.Streun, S.Tavernier, J.M.Vieira, The ClearPET project: development of a 2nd generation high-performance small animal PET scanner. Nucl Instr and Meth A 537 (2007) 307.

[9] P.Lecoq, J.Varela, ClearPEM, a dedicated PET camera for mammography. Nucl Instr and Meth A 486 (2002) 1.

[10] J.Varela, A PET imaging system dedicated to mammography. Radiation Physics and Chemistry, In Press, Corrected Proof, Available online 5 June 2006.

[11] M.E.Phelps, E.J.Hoffman, N.A.Mullani M.M. Ter-Pogossian, Application of Annihilation Coincidence Detection to Transaxial Reconstruction Tomography. J Nucl Med 16 (1975) 210.

[12] M.M.Ter-Pogossian, M.E.Phelps, E.J.Hoffmann, N.A.Mullani, A positron-emission transaxial tomograph for nuclear imaging (PETT). Radiology 114 (1975) 89.

[13] P.Olivier, Nuclear oncology, a fast growing field of nuclear medicine. Nucl Instr and Meth A 527 (2004) 4.

[14] F.H.Fahey, Data Acquisition in PET Imaging. J Nucl Med Technol 30 (2002) 39.

[15] A.Alessio and P.Kinahan, PET Image Reconstruction. In: Nuclear Medicine (2nd ed.). Henkin et al., Eds., Philadelphia, Elsevier 2006.

[16] A.F.Chatziioannou, PET Scanners Dedicated to Molecular Imaging of Small Animal Models. Molecular Imaging and Biology 4 (2002) 47.

[17] E.Auffray, M.Boutemeur, G.Brandenburg, P.Bruyndonckx, Y.Choi, Y.DAsseler, O.Devroede, O.Dietzel, C.Dujardin, A.Fedorov, M.Janier, J.H.Jung, M.Khodaverdi, M.Korjik, M.Krieguer, C.Lartizien, H.Larue, P.Lecoq, C.Lematre, J.F.Loude, C.Morel, J.B.Mosset, C.Parl, C.Pautrot, C.Pedrini, A.G.Petrosyan, U.Pietrzyk, M.Rey, D.Sappey-Marinier, P.Sempere Roldan, T.Y.Song, S.Staelens, M.Streun, S.Tavernier, J.Trummer, S.Vandenberghe, R.Van Holen, J.M.Vieira, S.Weber, E.Wieors, M.Wisniewska, D.Wisniewski, Y.Wu, K.Ziemons, First results with the ClearPET small animal PET scanners. in:Radiation Detectors for Medical Application. NATO Security through Science Series, published by Springer Netherlands, 2006. 149-164.

[18] M.Khodaverdi et al, High Resolution Imaging with ClearPET^{TM} Neuro - First Animal Images, 2005 IEEE NSS-MIC Conference Record, 23.-29.Oct.2005, Wyndham El Conquistador Resort, Puerto Rico.

[19] M.Khodaverdi, Status of and first scans with the ClearPET Neuro. 42nd General meeting CCC, CERN, Geneva, 2-3 March 2005.

[20] M.Streun, G.Brandenburg, H.Larue, E.Zimmermann, K.Ziemons, H.Halling, A PET system with free running ADCs. Nucl Instr and Meth A 486 (2002) 18.

[21] P.Musmann, U.Pietrzyk, N.Schramm, S.Weber, List-Mode Image reconstruction for the High Resolution ClearPET Neuro System. 2005 IEEE NSS-MIC Conference Record, 23.-29.Oct.2005, Wyndham El Conquistador Resort, Puerto Rico.

[22] P.Sempere Roldan, E.Chereul, O.Dietzel, L.Magnier, C.Pautrot, L.Rbah, D.Sappey-Marinier, A.Wagner, L.Zimmer, M.Janier, V.Tarazona, G.Dietzel, Raytest ClearPET^{TM}, a new generation small animal PET scanner. Nucl Instr and Meth A 571 (2007) 498.

[23] Raytest - ClearPET Peformances. http://raytest.com/index2.html, Feb 2007.

[24] A.M.Wallace, C.Comstock, C.K.Koh, D.R.Vera, Breast imaging: a surgeon's prospective. Nucl Med Biol 32 (2005) 781.

[25] M.C.Abreu, D.Aguiar, E.Albuquerque, F.G.Almeida, P.Almeida, P.Amaral, E.Auffray, P.Bento, P.Bruyndonckx, R.Bugalho, B.Carrico, H.Cordeiro, M.Ferreira, N.C.Ferreira, F.Goncalves, P.Lecoq, C.Leong, F.Lopes, P.Lousa, J.Luyten, M.V.Martins, N.Matela, P.R.Mendes, R.Moura, J.Nobre, N.Olifeira, C.Ortigao, L.Peralta, J.Rego, R.Ribeiro, P.Rodrigues, A.I.Santos, J.C.Silva, M.M.Silva, S.Tavernier, I.C.Teixeira, J.P.Teixeira, A.Trindade, J.Trummer, J.Varela, Clear-PEM: A PET imaging system dedicated to breast cancer diagnostics. Nucl Instr and Meth A (In Press, Corrected Proof, Available online 7 November 2006.

[26] C.Cohen-Bacrie, Design and operation of the elastometry probe. SuperSonic Imagine, 13857 Aix-en-Provence

[27] E.Franceschini, M.C.Pauzin, S.Mensah, J.P.Lefebvre, P.Lasaygues, E.Debieu, The US tomographic system. CNRS-LMA, Equipe PI, 31 Chemin Joseph Aiguier, 13402 Marseille

Chapter 2

Scintillators

One of the most important parts of a PET detector are the scintillator crystals. The requirements on the scintillation materials for a good detector performance are very stringent. In this chapter a short review of the physics of scintillation in inorganic crystals is given and the most important properties of scintillation material are explained. Basically a scintillator is a material that converts absorbed energy into a light pulse usually in the visible or UV range.

Scintillation materials have been used to detect radiation for almost one hundred years. Röntgen in 1895 and later Crookes in 1904 were the first to use screens covered with scintillation materials (calcium tungstate ($CaWO_4$) and zinc sulfide (ZnS) respectively) to detect radiation. however, the beginning of the rise of scintillation counters was not until the year 1940 when photomultiplier tubes were introduced to detect the light flashes. Nowadays they are widely used in high energy physics (mostly for calorimetry) and for medical imaging.

Most applications require single crystal scintillators. The crystals are used in various sizes and shapes. The technology of crystal growth does not depend on the subsequent application, but quite often there are certain demanding requirements imposed on the growth process by the application: homogeneous properties, purity of the material and minimum amount of defects. Great care has to be exercised during the process of crystal growing [1].

2.1 Crystal growth techniques

Crystal growing is a complicated process. A variety of parameters such as temperature, stoichiometric composition, pulling velocity, material purity and dopant distribution have to be carefully monitored and stabilized during the process. Many methods for single crystal growth exist but they all fall into one of two categories:

- single crystal pulling from a melt, e.g. the Czochralski method [2];
- single crystal growth in an ampoule, e.g. the Bridgman-Stockbarger technique [3, 4].

2.1.1 Czochralski method

The Czochralski method was serendipitously discovered in 1916 by Jan Czochralski. The powdered raw materials are melted in a crucible. The dopant can be added to the melt in precise amounts. A small seeding crystal is attached to the point of a rotating metal rod. The crystal has to be placed with the desired orientation. Only the tip of the seed is dipped into the melt. The melt crystallizes at the phase boundary between the solid and liquid phase because of the temperature gradient. The crystal is slowly pulled from the melt. The pulling rate and the temperature determine the crystal diameter and should be kept constant. Fig. 2.1 (a) shows a schematic drawing of this method.

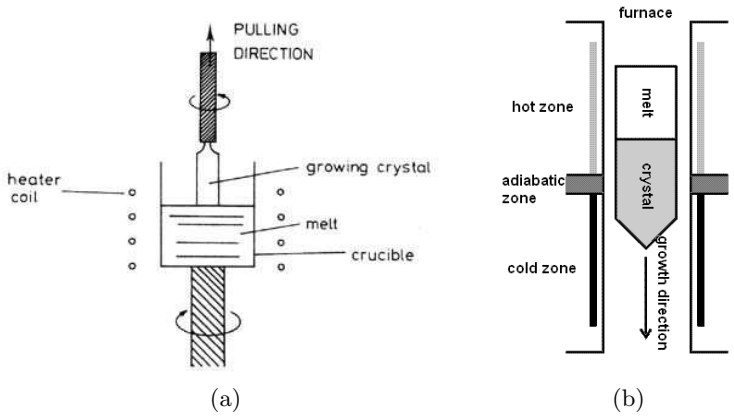

Figure 2.1: Schematic drawing of the Czochralski method (a) and the Bridgman-Stockbarger technique (b)

2.1.2 Bridgman-Stockbarger technique

In the Bridgman-Stockbarger technique the crystal is grown in an ampoule. A picture of the technique is shown in Fig 2.1 (b). In the furnace there is a hot zone where the temperature is above the melting point of the crystal, a cold zone and an adiabatic loss zone in the middle. The raw material is first put in the high temperature zone to melt and then the ampoule is slowly pulled through the furnace towards the cold zone to crystallize. The crystal can be grown with or without a seed. Without a seed the orientation of the crystal is difficult to control because crystallization happens spontaneously in all directions.

2.2 Inorganic scintillators

Scintillation materials can be divided in organic and inorganic solids, liquids and gases. Organic scintillators are not considered in medical applications because the scintillation intensity of organic materials is only one half to one third as bright as of inorganic materials. Furthermore the probability for photoelectric events is very low.
The inorganic scintillators can themselves be separated in different categories: intrinsically or extrinsically luminescent or in another manner according to their chemical composition: halides, oxides, chalcogenides and glasses. Some widely used scintillators in high energy physics and medical imaging and their main properties are listed in Table 2.1. All types of scintillators have in common the presence of luminescence centres

Table 2.1: Properties of scintillators used in high energy physics and medical imaging: density, number of emitted photons per energy unit, peak wavelength of the emitted light and decay time of the scintillation pulse

Scintillator	Name	Density [g/cm^2]	Light yield [ph/MeV]	Peak emission λ [nm]	Decay time τ [ns]	Ref.
NaI:Tl	Sodium Iodide	3.67	43000	415	230	[5]
$Bi_4Ge_3O_{12}$ (BGO)	Bismuth Germanate	7.1	9000	480	300	[6, 7]
$PbWO_4$ (PWO)	Lead Tungstate	8.3	200	420	15	[8]
Lu_2SiO_5:Ce (LSO)	Lutetium Oxyorthosilicate	7.4	26000	420	40	[9, 10, 11]
$Lu_{2(1-x)}Y_{2x}SiO_5$:Ce (LYSO)	Lutetium Yttrium Oxyorthosilicate	7.1	31200	420	40	[12]
$LuAlO_3$:Ce (LuAP)	Lutetium Aluminate	8.34	11400	365	17 + 120	[13]
$Lu_{0.7}Y_{0.3}AlO_3$:Ce (LuYAP)	Lutetium Yttrium Aluminate	7.1	8200	375	25 + 250	[14, 15]
$LaBr_3$:Ce^{3+}	Barium Fluoride	5.29	61000	356 + 387	30	[16]

in the lattice. The nature of these luminescence centres differs from scintillator type to scintillator type (activator ions, defects or impurities) but the effect is always the same: the origin of scintillation light.

2.2.1 Active centres

The model used to describe inorganic crystals is the collective electron or band theory developed by Felix Bloch in 1928. It is based on the solution of the Schrödinger equation for an electron in a periodic potential. The discrete energy levels of an isolated atom are broadened by the perturbations caused by mutual interaction of atoms in a crystal to a continuous series of energy bands. In an ideal crystal, free of defects a forbidden band of electron energies exists between the last occupied states, the valence band and the first empty level, the conduction band (Fig 2.2 (a)). The width of the band is some eV.
Electrons can be raised from the valence to the conduction band if enough energy is provided, the movement of electrons from the valence band to the conduction band leaves holes in the valence band. Defects, intentional and unintentional impurities can create additional energy levels in the forbidden band between the valence and conduc-

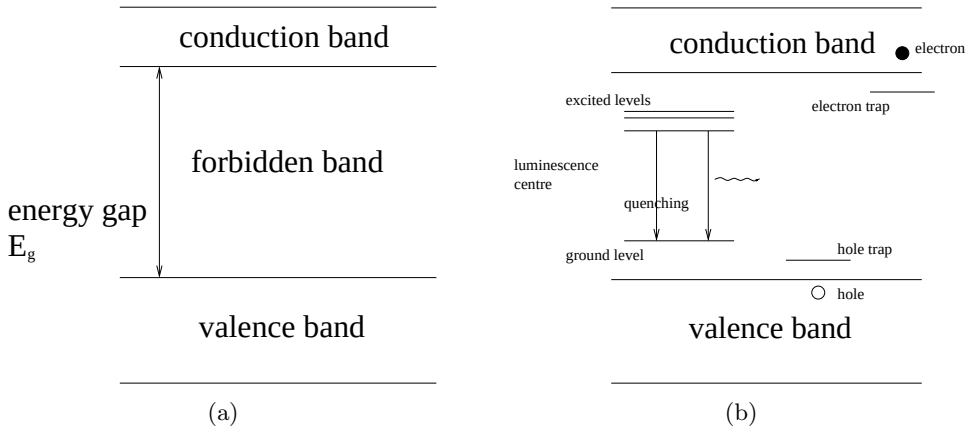

Figure 2.2: Energy band model of a perfect crystal (a) and with impurities (b)

tion band (Fig. 2.2 (b)). If they are unoccupied, electrons, holes or excitons may enter these centres. Three different types of centres exist:

1. Luminescence centres: the presence of luminescence centres in ionic crystals or semiconductors turns the material into a scintillator. The transition from the excited to the ground state occurs with the emission of a photon. The nature of the centres defines the properties of the scintillator. Two different types of luminescence centres exist: intrinsic and extrinsic. Intrinsic scintillation is caused by defects in the crystal lattice whereas for extrinsic scintillation is caused by the presence of especially added ions in the lattice.

2. Quenching centres: at a quenching centre a radationless transition from the excited to the ground state takes place via phonons.

3. Traps: shallow traps can exist in the forbidden band which are metastable levels from which the trapped electrons can escape either to the conduction band by acquiring extra energy or fall back into the valence band without emitting a photon. As the carriers migrate through the crystal they can also be trapped by deep traps (impurities, lattice defects, ...) and are so lost for the scintillation process.

The net effectiveness of a luminescence centre is measured as number of emitted photons over the number of absorbed photons, which is called the quantum efficiency q of the luminescence centre. It is a function of the probabilities for radiative and non-radiative transition p_r and p_{nr} respectively, (eq. 2.1).

$$q(T) = \frac{p_r}{p_r + p_{nr}} = \frac{1}{1 + C \cdot e^{(-\frac{E_q}{k_B T})}} \tag{2.1}$$

E_q is the quenching energy and k_B the Boltzmann constant.

2.3 Scintillation process

When a photon passes through matter, it loses energy through three fundamental electro-magnetic processes:

- photo absorption;
- Compton scattering;
- and pair production.

The attenuation of a beam of γ-rays in matter follows the exponential law

$$I(x) = I_0 e^{-\mu x} \tag{2.2}$$

where I_0 is the initial intensity and μ is the attenuation coefficient. μ includes the cross sections of all interaction processes. Depending on the energy of the particle and the effective Z of the material, one process will dominate over the others.

Scintillation in inorganic crystals takes place in a the following stages [17]:

1. - Absorption of the incident radiation and production of primary electrons and holes
   - Relaxation of electronic excitations (primary electrons and holes) which leads to secondary electrons, holes, photons, plasmons and other electronic excitations
   - Thermalization of the secondary electrons resulting in electron-hole (e-h) pairs with an approximate energy of the band gap
2. Energy transfer from the e-h pairs to the luminescence centres and their excitation
3. Photon emission

In Fig. 2.3 the elementary processes that take place in a scintillating crystals after absorption of a photon are illustrated. A resulting fast electron from a photoelectric event will relax by further ionization and creating more free electrons and holes and scattering on other electrons or phonons. It can also interact with the electrons in the valence band and produce plasmons which in turn decay into e-h pairs. The atom with an ionized inner shell can itself relax by emitting a x-ray photon or an Auger electron where both particles can again take part in the creation of even more electrons and holes. The avalanche process continues until the energy of the particles fall below the ionization threshold. This marks the end of the electron-electron relaxation stage and the beginning of electron-phonon or thermalization stage.

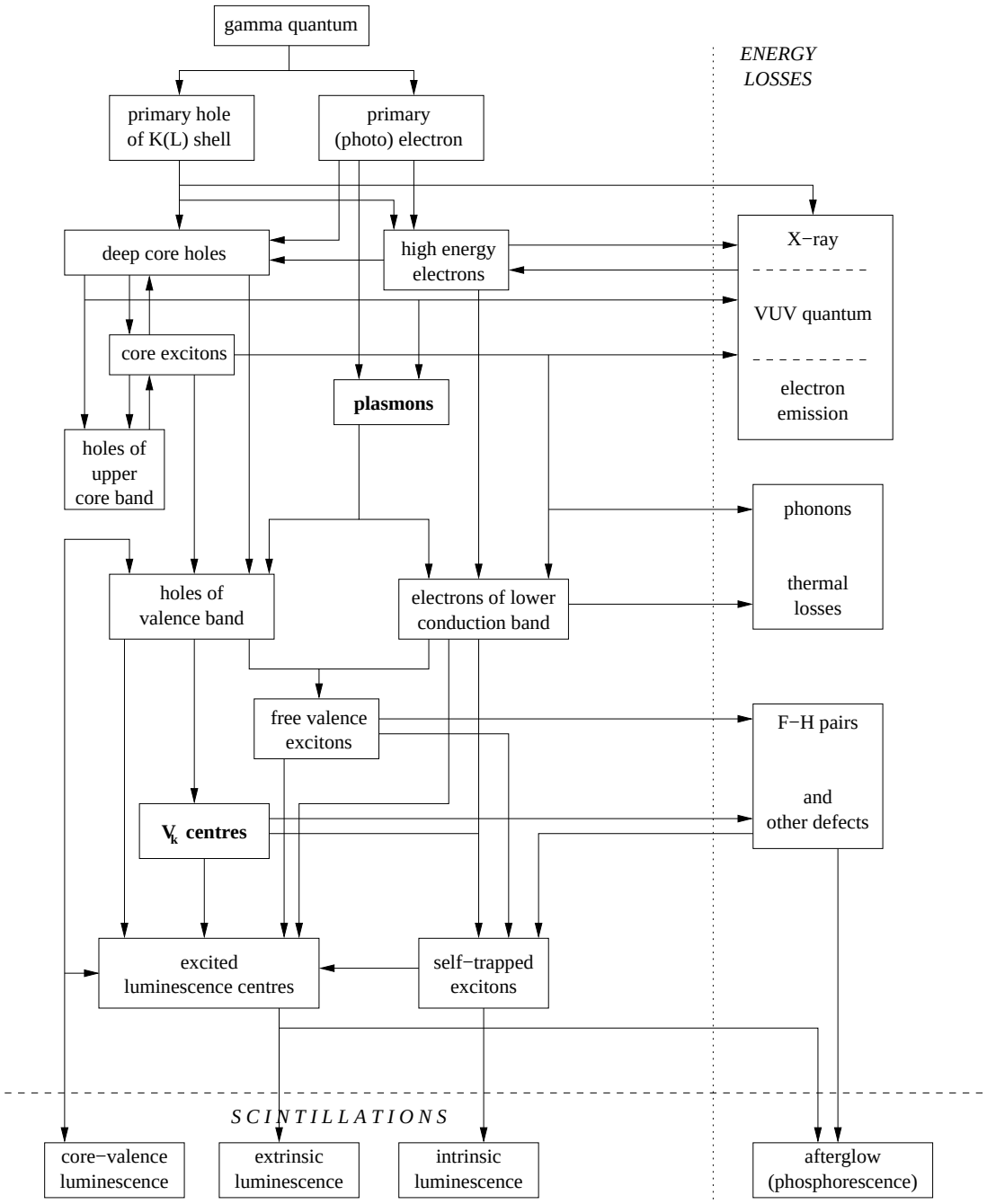

Figure 2.3: Elementary processes in an inorganic scintillator [17]

The electrons move down to the bottom of the conduction band and the holes to the top of the valence band. Thus the number of N_{eh} of electron-hole pairs is fixed to:

$$N_{eh} = \frac{E_\gamma}{E_{eh}} \tag{2.3}$$

where E_γ is the absorbed energy of the incident photon and E_{eh} the energy necessary to create a thermalized energy-hole pair which is approximately 2-3 times the energy of the band gap. When an electron is lifted from the valence to the conduction band and stays bound with its hole the result is a so called exciton with an energy slightly smaller than the band gap.
The last two stages include migration, localization, energy transfer to luminescence centres and recombination.
The following enumeration lists the possible recombination reactions:

1. $e^- + hole \rightarrow h\nu$
2. $e^- + hole \rightarrow ex \rightarrow h\nu$
3. $V_k + e^- \rightarrow V_k + exiton \rightarrow h\nu$
4. $V_k + exiton \rightarrow h\nu$
5. $A \rightarrow A^* \rightarrow A + h\nu$

In the first two cases the luminescence centre is excited by the successive capture of an electron and a hole or vice versa or by the capture of an exciton. Another option is the involvement of so-called self-trapped excitons (STE) or self-trapped holes (STH or V_k centres). When a hole or a hole associated with an exciton is localized between two anions in the lattice a STH or STE is formed. The luminescence arises from the recombination of V_k centres with free electrons or through direct energy transfer from an STE to a luminescence centre. The last case represents electronic transitions from energy levels of activator ions with which the crystal has been doped, e.g the transition from 5d→4f in Ce^{3+}.
The emission of photons from the excited luminescence centres is the final stage in the scintillation process. Table 2.2 lists the different processes involved, together with their average duration.

Table 2.2: Time scale for the processes involved in scintillation

Process	Time [s]
Absorption	10^{-13} to 10^{-15}
Electron-electron relaxation	10^{-15} to 10^{-13}
Electron-phonon relaxation	10^{-11} to 10^{-12}
Formation of STHs and STEs	10^{-11} to 10^{-12}
Decay of luminescence centres	$>10^{-9}$

2.3.1 Cerium-activated crystals

Cerium-doped Lutetium-Aluminiumperovskite (LuAP:Ce), cerium-doped Lutetium-Yttrium-Aluminiumperovskite (LuYAP:Ce) and cerium-doped Lutetium-Yttrium Oxyorthosilicate (LYSO:Ce) are the materials which are used in the present study.
Rare earth (RE) ions are very good activators for many materials. Europium Eu^{3+}, cerium Ce^{3+} and neodymium Nd^{3+} ions are usually used. The ground state electron configuration of cerium is: $[Xe].4f^1.5d^1.6s^2$. The free Ce^{3+} ion has one electron in the ground state 4f and the excited states are 5d and 6s. The energy gap between the 4f ground state and the excited 5d states is a few eV, depending on the host material. 4f-5d transitions are parity-allowed and give rise to an emission in the UV or visible range of the spectrum. The spin-orbit interaction splits the ground and the excited state into two pairs of levels, $^2F_{7/2}$ and $^2F_{5/2}$ and $^2D_{5/2}$ and $^2D_{3/2}$ separated by 2250 cm^{-1} and 2500 cm^{-1} respectively. That corresponds to an energy of 0.28 eV and 0.31 eV. In crystals with low local symmetry of Ce^{3+} sites, such as LuAP, the excited 5d level splits into five Stark components [17] but only in three levels for LSO compounds [18]. At room temperature not all the emission bands can always be resolved. Two processes contribute to the scintillation:

$$(Ce^{3+})^* \rightarrow Ce^{3+} + h\nu$$

$$Ce^{3+} + hole \rightarrow Ce^{4+} + e \rightarrow (Ce^{3+})^* \rightarrow Ce^{3+} + h\nu$$

In Lu(Y)AP and L(Y)SO the Ce 4f level and excited levels lie in the forbidden gap either just above the valence band or below the conduction band. This increases the hole capture probability and leads to very efficient scintillators. The excited levels of the Ce^{3+} ion usually lie in the forbidden band as well (Fig. 2.4 (a)). In narrow band-gap crystals they can fall into the conduction band and then the Ce^{3+} luminescence is quenched. In addition to Ce^{3+} ions, Ce^{4+} ions can also be present in the crystal

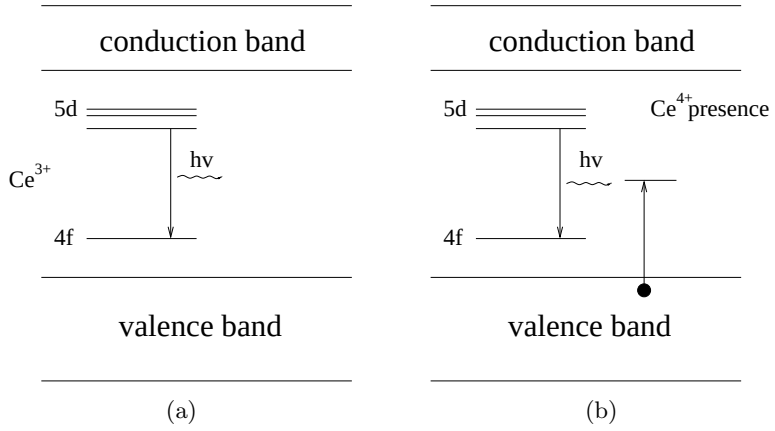

Figure 2.4: Optimal case with only Ce^{3+} ions (a) and negative influence of Ce^{4+} ions(b) in the lattice

(Fig. 2.4 (b)). Ce^{4+} has no electron in the 4f shell but can capture an electron from the valence band and form a charge transfer state (CTS). A CTS can be described as a Ce^{3+} ion with a nearby hole in the valence band.

$$Ce^{4+} + h\nu \rightarrow Ce^{3+} + hole$$

The CTS can relax non-radiatively to the ground state [1].

2.3.2 Light loss

Energy is lost for the scintillation process at all stages. Particles, such as x-ray photons or backscattered electrons leave the crystal. Traps capture free electrons and holes. Phonons are created and lead to thermal losses. And finally the scintillation photons are absorbed in the crystal itself.

Thermal quenching

Quenching is the undesirable effect of de-excitation of a luminescence centre without photon emission. A general model to describe the energy levels of ions taking into account interactions with the lattice is the configuration coordinate diagram in Fig. 2.5 (a). The energy E is plotted versus the configuration coordinate Q which is the mean inter-atomic distance between the luminescence centre and the neighbouring ions in the crystal lattice. The potential energies of the ground and excited state of the ion are represented by parabolas. The horizontal lines represent the electron levels separated by a distance $\hbar\omega$. The equilibrium position of the ion in the ground state is not the same as in the excited state. This shift between the emission and the absorption bands is called Stokes shift. At the crossing point between the two parabolas the radiationless transition back to the ground state can take place. An electron can acquire the necessary energy E_q thermally. In eq. 2.1 only p_{nr} is temperature-dependant with the Boltzmann factor. That means that thermal quenching becomes more important with rising temperature. In the case of weak or no Stokes shift a non-radiative process can still happen with the creation of phonons.

Concentration quenching

The probability of an interaction between luminescence centres increases with their distribution density of the dopant. Energy can transfer from centre to centre until it gets lost in a quenching centre. The critical concentration, above which concentration quenching becomes relevant, is a few atomic percent of dopant ions in the crystal.

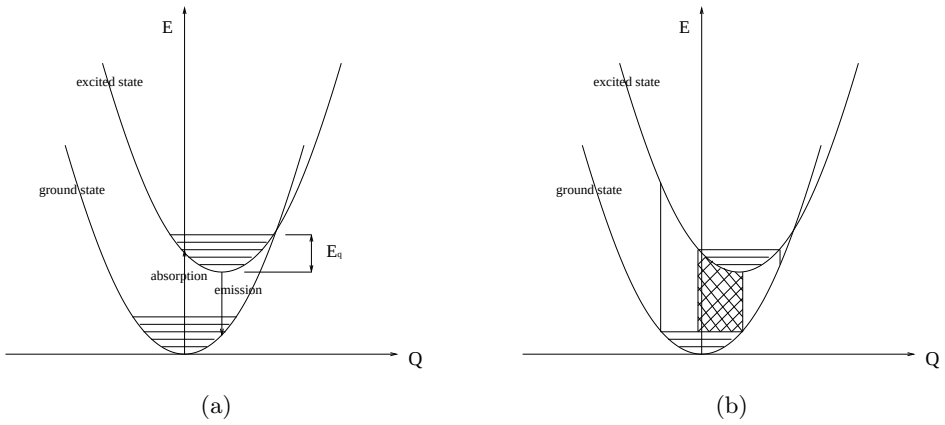

Figure 2.5: Configurational coordinate diagram. The ground state and an excited state are represented by potential curves (a) and overlapping of the absorption and emission bands (b)

Absorption

The scintillator should ideally be transparent to the wavelength of its emitted photons. Nevertheless the scintillation light can be absorbed by impurities or defects in the crystal (background absorption) or by the same luminescence centres (reabsorption). Background absorption can be reduced by carefully controlling the crystal growth environment, by using pure raw materials, the appropriate crucible material and a stable temperature. The absorption varies with the impurity concentration and can be very different for crystals cut from the same ingot but from different positions. As can be seen in Fig. 2.5 (b) reabsorption is connected to the Stokes shift, it becomes less dominant with increasing displacement from the equilibrium position because of a smaller overlap between the absorption and emission bands. Reabsorbed and re-emitted photons do not decrease the light yield but only lengthen the decay time.

Radiation damage

Ionizing radiation causes damage in the crystal. This can be the creation of point defects, colour centres or traps and changes in the luminescence centres. The most important effect on the crystal properties is a deterioration of the optical transmission. Some irradiated crystals show recovery from radiation damage although with a very slow healing rate at room temperature. Thermal bleaching at 200°C to 350°C or irradiation with ultraviolet or visible light are two methods with which a near full recovery can be achieved.

2.4 Scintillator requirements in PET

The general properties of inorganic scintillators are [17]:

- Conversion efficiency and scintillation yield;
- Decay time;
- Phosphorescence;
- Temperature stability;
- Transmission and index of refraction;
- Radiation hardness;
- Density and stopping power;
- Wavelength of emission;
- Hardness, ruggedness and cleavage;
- Hygroscopicity;
- Availability;
- Cost;
- Homogeneity and uniform distribution of impurities ;
- Proportionality between the absorbed energy and number of emitted photons.

Depending on the application some of the above mentioned properties are more important than others. It should also be understood that no material meets all criteria and the best possible compromise has to be found for each application. Some advantages and disadvantages of scintillators used in PET are listed in Table 2.3.

For a scintillator used in medical imaging the most important properties are:

High density and high atomic number

Crystals utilized for PET should have a high density and an absorption length for 90% of the energy of a 511 keV γ-photon should be smaller than 30 mm. High density materials usually have high Z ions in the lattice which increases the photoelectric fraction ($\sim \quad \rho Z_{eff}^{n} E_{\gamma}^{n}$, where n is 4 at 100 keV and increases to 4.6 at 3 MeV and m is 3 at 100 keV and decreases to 1 at 5 MeV). If a photon which scattered in the patient is absorbed via the photoelectric effect it, it can be rejected by an energy discriminator. Compton scattering in the crystal reduce the effectiveness of the energy discrimination. High Z is also important to guarantee high stopping power for 511 keV photons. This requirement keeps the scanner compact and achieves good spatial resolution.

Table 2.3: Advantages and disadvantages of scintillators used in PET

Scintillator	bright	fast	phosphorescent	dense	hygroscopic	cost	rugged
NaI	☺	☹	no ☺	☹	☹	☺	no ☹
BGO	☺	☹	no ☺	☺	☺	☺	yes ☺
L(Y)SO	☺	☺	yes ☹	☺	☺	☺	yes ☺
Lu(Y)AP	☹	☺	no ☺	☺	☺	☹	yes ☺
LaBr	☺	☺	no ☺	☹	☹	☹	no ☹

Fast decay time

The scintillator response should be fast in order to minimize dead time. A short dead time reduces the examination time and the cost. A short decay time also improves the timing resolution. Typically the length of the coincidence window is twice the timing resolution, $2\Delta t$. A good timing resolution allows to use shorter coincidence time windows which reduces the random coincidence rate which is given by $2\Delta t S^2$ where S is the singles rate per detector.

High light yield

A high light yield is important for good timing and energy resolution. For a given decay time a higher light yield leads to a higher initial intensity and better timing resolution. If the light yield increases by a factor of two, both the time and energy resolution increase by 30%.
Another important point is the that a high light yield can help reduce the background noise due to Compton scattered photons in the patient. The energy resolution is directly influenced by the light yield.

Good energy resolution

As already mentioned good energy resolution is important to reject photons that scattered in the patient before arriving at the detector which only contribute to the background noise. Only events that lie in the full-energy peak of the pulse height spectrum are accepted. The better the energy resolution, the better the background reduction.

Recent improvements

Current research interests lie in the development of brighter and faster scintillation materials. A new promising material is $LaBr_3:Ce^{3+}$ [16] which has a light yield of 61000 photons/MeV and a deacy time constant of 30 ns. Unfortunately the crystal has a low density and is hygroscopic.Another approach is adding intentional impurities to existing scintillators. Petrosyan et al [19] reported reduced light absorption in LuAP and LuYAP crystals by adding some ppm of hafnium, zirconium or tantalum ions.

2.5 General characteristics

2.5.1 Light yield

The light yield is dependant on the efficiency with which the energy of an incident γ-photon is converted to scintillation photons. The overall efficiency η can be written as a product of three parameters [20] which defines the three steps of the scintillation process described in 2.3:

$$\eta = \beta SQ \qquad\qquad 0 \leq \eta, \beta, S;\ Q \leq 1 \tag{2.4}$$

The first parameter β describes the conversion of the energy of the γ photon to electron-hole pairs, in other words, the ratio between the actually number of e-h pairs produced and the maximum possible number n_{e-h}.
The minimum energy required to produce one e-h pair in a material with band gap E_g is:

$$\xi_{min} = bE_g \tag{2.5}$$

where b is a specific parameter dependant on the crystal structure and the type of chemical bonds in the material. The value of b is around 1.5 to 2.0 for ionic crystals and 3 to 4 for semiconductors. The maximum possible number of e-h pairs is then given by:

$$n_{e-h} = \frac{E_\gamma}{\xi_{min}} = \frac{E_\gamma}{bE_g} \tag{2.6}$$

The second parameter S in eq. 2.4 specifies the efficiency of the energy transfer from the e-h pairs to the luminescence centres and the third parameter Q is called the luminescence efficiency or quantum efficiency of the luminescence centre, the probability of emission of a photon from the luminescence centre. The number of photons generated by a single γ-particle will be:

$$n_{ph} = n_{e-h}SQ = \frac{E_\gamma}{bE_g}\ \beta SQ \tag{2.7}$$

Hence the light yield (LY) in photons/MeV can be expressed as:

$$LY = \frac{n_{ph}}{E_\gamma[MeV]} = \frac{\beta SQ}{bE_g} \tag{2.8}$$

E_g and Q are standard measurements in optical spectroscopy of solids, β can be found using Monte-Carlo calculations of the energy dissipation in crystals and proper material constants and the only unknown, S, can then be derived from eq. 2.8 [21, 22]. For many materials Q is found to be close to unity.

Eq. 2.8 also implies that for band gap energies close to zero the light yield should rise to large values. This is only valid up to a certain point. Since the scintillator should be transparent for its own light, E_g should always be greater than the energy of the emitted photons $h\nu_{max}$.
If S and Q were equal to 1, eq. 2.8 gives the maximum reachable light yield and the number of photons/MeV were equal to the number of electron-hole pairs. Table 2.4 shows the values for the theoretical and actual light yield together with the conversion efficiency for some scintillator materials. The above statement is evidently only true in the case of CsI:Tl. For LuAP and LSO it has been shown that Q equals indeed unity, thus identifying the transfer efficiency S as the responsible parameter for the lower than possible light yield.

Table 2.4: Theoretical, actual light output and conversion efficiency for selected scintillators (taken from [23])

Material	Calculated e-h pairs per MeV	Observed light output per MeV	η
CsI:Tl	69444	65000	0.936
NaI:Tl	75330	38000	0.504
$Bi_4Ge_3O_{12}$ (BGO)	88889	8500	0.096
Lu_2SiO_5:Ce (LSO)	69444	27300	0.393
$LuAlO_3$:Ce (LuAP)	55556	11300	0.20

Non-proportionality

The basic assumption which underlies all scintillation counters is that the light output is linearly proportional to the absorbed energy. However, some scintillation crystals show non-proportional behaviour, especially at low energies. This non-proportionality has been observed in many halide and oxide scintillation crystals [25]. In halides (NaI:Tl, CsI:Tl, CsI:Na) the relative light output decreases with increasing energy, in oxides (LSO, LYSO, LuYAP) this trend is reversed. The phenomenon is strongly connected to the number and energy distribution of secondary electrons. Different theories that have been proposed and investigated can be found in the literature [24, 26, 27]. It is presently impossible to predict the response function of any given material.
The non-proportional response curves for LuAP, LuYAP and LYSO crystals are shown in section 1.3.

2.5.2 Energy resolution

For the evaluation of the energy resolution one has to take into account the whole system of scintillator and photomultiplier tube. Statistical fluctuations $v(Q_0)$ in the processes that lead to an output pulse of Q_0 electrons at the anode of the PMT determine the energy resolution. According to Birks [28] the mean output pulse is:

$$\overline{Q}_0 = \overline{N}\,\overline{p}\,\overline{M} \tag{2.9}$$

$\overline{N}$ is the mean number of photons created in the scintillator, $\overline{p}$ is the mean photon transfer efficiency[1] and $\overline{M}$ is the mean overall gain of the PMT. The variance $v(Q_0)$ is:

$$v(Q_0) = v(p) + [1 + v(p)]\left[v(N) - \frac{1}{\overline{N}}\right] + \frac{1 + v(M)}{\overline{N}\,\overline{p}} \tag{2.10}$$

and may be approximated by:

$$v(Q_0) \approx \left[v(N) - \frac{1}{\overline{N}}\right] + v(p) + \frac{1 + v(M)}{\overline{N}\,\overline{p}} \tag{2.11}$$

The term in square brackets in eq. 2.11 represents the fluctuations in the number of photons due to other effects than Poisson statistics. It is also referred to as the intrinsic resolution R_i. The second term corresponds to the transfer resolution R_p (transfer process of the photons from the scintillator to the photomultiplier) and the last term to the photomultiplier resolution R_M [24]. The energy resolution R is commonly expressed as $(\Delta E/E)_{FWHM}$ and is related to the variance of Q_0 by

$$R = \left(\frac{\Delta E}{E}\right)_{FWHM} = 2.36\sqrt{v(Q_0)} \tag{2.12}$$

or

$$R^2 = R_i^2 + R_p^2 + R_M^2 \tag{2.13}$$

The intrinsic resolution itself can be split into two terms, one is associated with the non-proportional response of the scintillator to different photon energies and the second is connected to inhomogeneities of the crystal causing different light yields at different interaction points in the crystal.

$$R_i^2 = R_{np}^2 + R_{inh}^2 \tag{2.14}$$

The transfer resolution is influenced by many factors: the wavelength of the photon, the quantum efficiency of the PMT, the optical properties of the scintillator, the angle of incidence on the photocathode and the properties of the photocathode. For modern scintillation counters R_p is assumed to be negligible compared to the other factors and R^2 becomes:

$$R^2 = R_i^2 + R_M^2 \tag{2.15}$$

[1] $p = g_c m C_{pe} G$, G...fraction of N photons that impinge on the photocathode, mC_{pe}...conversion efficiency of photons into electrons, g_c...collection efficiency of electrons at the first dynode

where the statistical term R_M is given by:

$$R_M = 2.36\sqrt{\frac{1+v(M)}{\overline{N}\overline{p}}} \tag{2.16}$$

The energy resolution of a scintillator is proportional to one over the square root of the number of emitted scintillation photons:

$$\Delta E \propto \frac{1}{\sqrt{N_{ph}}} \tag{2.17}$$

Typical values for LuAP and LuYAP crystals are 4% at 662 keV.

2.5.3 Depth of interaction resolution

In a crystal read-out as shown in Fig. 2.6 the signal E_1 from PMT 1 can be written as:

$$E_1 = N_0 P e^{-\mu(\frac{L}{2}+x)} \tag{2.18}$$

And similarly the signal from PMT 2 is:

$$E_2 = N_0 P e^{-\mu(\frac{L}{2}-x)}, \tag{2.19}$$

where μ is the light absorption coefficient, $2N_0$ the number of photons generated by the γ interaction, P the probability that light produced at one end of the crystal will generate a photoelectron and L and x the length of the crystal and the displacement of the interaction from the middle respectively (see Fig. 2.6). The inverse of μ is called the attenuation length λ. By dividing the difference between the left and the right signal

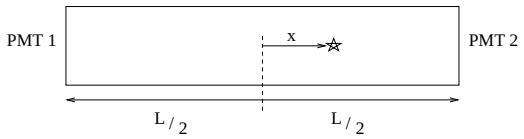

Figure 2.6: Schematic drawing of a crystal read out at both ends for depth of interaction measurements

$E_1 - E_2$ by the sum of both signals $E_1 + E_2$ and expanding the equation

$$\frac{E_1 - E_2}{E_1 + E_2} = \frac{e^{-\mu(\frac{L}{2}+x)} - e^{-\mu(\frac{L}{2}-x)}}{e^{-\mu(\frac{L}{2}+x)} + e^{-\mu(\frac{L}{2}-x)}} \tag{2.20}$$

one arrives at

$$\frac{E_1}{E_2} = e^{2\mu x} \tag{2.21}$$

From eq. 2.21 follows that the position x of the interaction is given by:

$$x = \frac{1}{2\mu} \ln\frac{E_1}{E_2} \tag{2.22}$$

With

$$\frac{\Delta E_1}{E_1} = \frac{1}{\sqrt{E_1}} \qquad and \qquad \frac{\Delta E_2}{E_2} = \frac{1}{\sqrt{E_2}} \tag{2.23}$$

it follows from the Gaussian law of error propagation that the DOI resolution Δx equals:

$$\Delta x = \frac{1}{2\mu\sqrt{N_0 P}}\, e^{\frac{\mu L}{4}}\, \sqrt{e^{-\mu x} + e^{\mu x}} \tag{2.24}$$

If E_1 and E_2 are replaced by the actual equation one finds that Δx not only depends on the number of generated photons, the position x and the attenuation μ. The best spatial resolution is obtained in the middle of the crystal. Assuming a crystal length of 20 mm, a light absorption coefficient of 1/20 mm and 1000 electrons reaching each photomultiplier, a $\Delta x/x$ of approximately 3% can be achieved.

2.5.4 Decay time

The decay time is the time interval that elapses between the excitation of the crystal and the emission of the scintillation light. The decay time constant is inversely proportional to the probability of de-excitation which can be radiative or non-radiative as explained in section 2.2.1:

$$\tau \propto \frac{1}{p_r + p_{nr}} \tag{2.25}$$

and is given by [17]:

$$\tau = \frac{c m_e}{8\pi e^2} \cdot \frac{\lambda^2}{f n} \left(\frac{3}{n^2 + 2} \right)^2 \tag{2.26}$$

where λ is the wavelength of the transition, f is the oscillator strength of the transition and n is the refractive index of the material. Eq. 2.26 shows that with increasing wavelength the decay time decreases. If only one type of luminescence centre exists in the crystal, the decay is exponential with only one time constant. The intensity of the emission at any moment $J(t)$ in photons/s is:

$$J(t) = J(0) e^{-\frac{t}{\tau}} \tag{2.27}$$

In reality many scintillators have a finite rise time and can exhibit more than one time constant. The decay curve can then be described as the sum of the individual exponential decays with their individual time constants. This is caused by delayed decay from secondary luminescence centres which is described by second-order kinetics. The finite rise time arises when the excitation energy is first concentrated in traps and only after some delay transferred to the luminescence centres.
The amplitude of the intensity after a certain time, e.g. ten times the decay time, is called afterglow.

2.5.5 Time resolution

To obtain a good timing resolution the scintillation pulse should be short (fast rise and decay time) and intense. The time resolution is directly proportional to the square root

of the decay time constant τ and indirectly proportional to the square root of the light yield:

$$\Delta t \propto \sqrt{\frac{\tau}{N_{ph}}} \tag{2.28}$$

Timing precision is a very important factor in a PET system. With better timing resolution the image quality increases because random coincidences can be reduced. The duration of the exam can be reduced thus making it more cost efficient. The initial activity of the radiotracer is smaller and the patient is exposed to a lesser dose.

A good timing resolution of the scintillator is not enough. The readout electronics and data acquisition systems have to be able to keep up with the speed of the scintillator and still be largely available and reasonably priced.

2.5.6 Transmission

The theoretical transmittance and reflectance can be calculated using:

$$T_{th} = \frac{(1-R)^2}{1-R^2} \qquad with \qquad R = \left(\frac{n-1}{n+1}\right)^2 \tag{2.29}$$

The formula takes into account repeated reflection on the exit surfaces.

The wavelength dependence of the refractive index n of a transparent optical material can be described by the Sellmeier formula eq: 2.30 using Sellmeier coefficients A_j, B_j which can be obtained from dispersion curves:

$$n(\lambda) = \sqrt{1 + \sum_j \frac{A_j \lambda^2}{\lambda^2 - B_j}} \tag{2.30}$$

The theoretical transmission can be quite different from the experimental values because it assumes an ideal crystal without any absorption. Knowing both the theoretical and the experimental transmittance the absorption coefficient $\mu(\lambda)$ can be calculated.

$$\mu(\lambda) = \frac{1}{L} \ln\left(\frac{T_{th}(\lambda)}{T_{exp}(\lambda)}\right) \tag{2.31}$$

L is the length of the crystal.
Fig. 2.7 shows an example of a transmission curve. The cut-off wavelength is obtained from the maximum of the first derivative of the fitted transmission curves (see section 1.5). The wavelength at the turning point of the transmission curve, the cut-off wavelength $\lambda_{cut\text{-}off}$ can be associated to the band gap energy E_g via the following equation:

$$E_g = \frac{hc}{\lambda_{cut\text{-}off}} \tag{2.32}$$

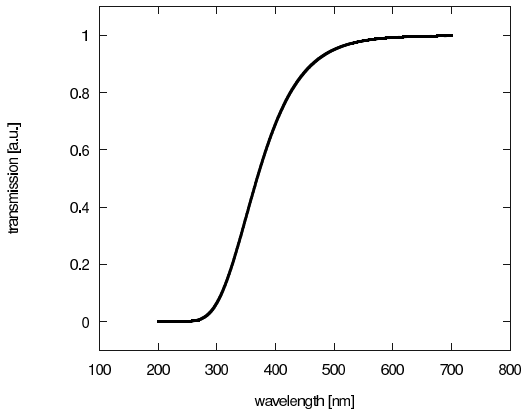

Figure 2.7: Idealized experimental transmission curve

Although in the case of cerium-doped scintillators this is not true. In this particular case the wavelength of the turning point is completely governed by the cerium concentration.

The theory of scintillation and the most important properties of scintillation crystals have been explained. The next chapter explains how to go about measuring them.

Bibliography

[1] P.Lecoq, A.Annenkov, A.Gektin, M.Korzhik, C.Pedrini, Inorganic Scintillators for Detector Systems - Physical Principles and Crystal Engineering. Berlin Heidelberg: Springer-Verlag, 2006.

[2] J.Czochralski, Z Physik Chem. 92 (1917) 219.

[3] P.W.Bridgman, Proc Am Acad Arts Sci 60 (1925) 303.

[4] D.C.Stockbarger, Rev Sci Instr 7 (1963) 133.

[5] E.Sakai, IEEE Trans Nucl Sci NS-34 (1987) 418.

[6] I.Holl, E.Lorenz, G.Magrans, A measurement of the light yield of common inorganic scintillators. IEEE Trans Nucl Sci NS-35 (1988) 105.

[7] M.J.Weber, R.R.Monchamp, Luminescence of $Bi_4Ge_3O_{12}$: Spectral and decay properties. J Appl Phys 44 (1973) 5495.

[8] E.Auffray, F.Cavallari, P.Lecoq, P.Sempere, M.Schneegans, Status of the PWO crystal production from Russia for CMS-ECAL. Nucl Instr and Meth A 486 (2002) 111.

[9] C.L.Melcher, US Patent No. 4,958,080 (1990).

[10] C.L.Melcher, J.S.Schweitzer, Cerium-doped lutetium oxyorthosilicate: a fast, efficient new scintillator. IEEE Trans Nucl Sci NS-39 (1992) 502.

[11] L.C.Melcher, M.Schmand, M.Eriksson, L.Eriksson, M.Casey, R.Nutt, J.L.Lefaucheur, B.Chai, Scintillation properties of LSO:Ce boules. IEEE NSS Conference Record. Volume 1, 8.-14. Nov. 1998 154.

[12] Data sheet, Photonic Materials Ltd (PML), Glasgow, UK.

[13] A.Moszynski, D.Wolski, T.Ludziejewski, M.Kapusta, A.Lempicki, C.Brecher, D.Wisniewski, A.J.Wojtowicz, Properties of the new LuAP:Ce scintillator. Nucl Instr and Meth A 385 (1997) 123.

[14] C.Kuntner, E.Auffray, D.Bellotto, C.Dujardin, N.Grumbach, I.A.Kamenskikh, P.Lecoq, H.Mojzisova, C.Pedrini,M.Schneegans, Advances in the scintillation performance of LuYAP:Ce single crystals. Nucl Instr and meth A 537 (2005) 295.

[15] W.P.Trower, M.V.Korzhik, A.A.Fedorov et al, Cerium-doped lutetium-based single crystal scintillators. In: P.Dorenbos, C.W.E.van Eijk, Inorganic scintillators and their applications. Delft University Press (1995) 355.

[16] E.V.D.van Loef, P.Dorenbos, C.W.E.van Eijk, K.W.Krämer, H.U.Güdel, Scintillation properties of $LaBr_3$:Ce^{3+} crystals: fast, efficient and high-energy-resolution scintillators. Nucl Instr and Meth A 486 (2002) 254.

[17] P.A.Rodnyi, Physical Processes in Inorganic Scintillators. New York: CRC Press, 1997.

[18] J.D.Naud, T.A.Tombrello, C.L.Melcher, J.S.Schweitzer, The role of Cerium sites in the scintillation mechanism of LSO. IEEE Trans Nucl Sci NS-43 (1996) 1324.

[19] A.G.Petrosyan, M.Derdzyan, K.Ovanesyan, P.Lecoq, E.Auffray, J.Trummer, M.Kronberger, C.Pedrini, C.Dujardin, P.Anfre, Properties of LuAP:Ce scintillator containing intentional impurities. Nucl Instr and Meth A 571 (2007) 325.

[20] D.J.Robbins, J Electrochem Soc 127 (1980) 2694.

[21] A.Lempicki, A.J.Wojtowicz, E.Berman, Fundamental limits of scintillator performance. Nucl Instr and Meth A 333 (1993) 304.

[22] W.van Roosbroeck, Phys Rev A 139 (1965) 1702.

[23] A.Lempicki, J.Glodo, Ce-doped scintillators: LSO and LuAP. Nucl Instr and Meth A 416 (1998) 333.

[24] P.Dorenbos, J.T.M.de Haas, C.W.E.van Eijk, Non-Proportionality in the Scintillation response and the Energy Resolution Obtainable with Scintillation Crystals. IEEE Trans Nucl Sci NS-42 (1995) 2190.

[25] W.W. Moses, Current trends in scintillator detectors and materials. Nucl Instr and Meth A 487 (2002) 123.

[26] R.B.Murray, A.Meyer, Scintillation response of activated inorganic crystals to various charged particles. Phys Rev 122 (1961) 815.

[27] G.C.Meggit, The effect of the crystal surface on the derived electron scintillation response in NaI(Tl). Nucl Instr and Meth 83 (1970) 313.

[28] J.B.Birks, The Theory and Practice of Scintillation Counting. Oxford: Pergamon Press, 1964.

[29] R.F.Post, L.I.Schiff, Statistical limitations on the resolving time of a scintillation counter. Phys Rev 80 (1950) 1113.

[30] G.Ranucci, Time statistics of the photoelectron emission process in scintillation counters. Nucl Instr and Meth A 335 (1993) 121.

Chapter 3

Experimental techniques

In this chapter the experimental techniques to characterize scintillating crystals are presented. The results of the measurements are presented and discussed in chapter 4.

3.1 Light yield and energy resolution

The purpose of the light yield measurements is to know how many photons are emitted by any particular crystal when excited with γ-radiation and with which accuracy the energy of the incident particle can be obtained.
The measurement of the light yield depends on many conditions, such as the temperature, high voltage or energy used. Then there are influences from the crystal itself. The photons created in the scintillating crystal undergo many reflections before they reach a detector and are converted into electrons. The geometry and surface condition of the scintillator, its self-absorption, the reflector material and the coupling to the photodetector have to be taken into account. Second, the type of photodetector used (usually a photomultiplier or photodiode) and its properties, such as size, quantum efficiency, sensitivity to the emitted wavelength of the scintillator and the window material play another important role. And last, changes in temperature and high voltage can influence the results.

Different direct and indirect methods exist for light yield measuring e.g. the pulse method, the single-electron method, the comparison method or a method based on the measuring of the intrinsic resolution of the photomultiplier [1]. The pulse method consists of measuring the signal amplitude at the output of the photodetector and calculating the light yield directly, assuming all PMT parameters and particle energies as known. The comparison method works by comparing the pulse amplitude of the PMT with the amplitude of a crystal with known light yield.

In this laboratory the single-electron method is used to measure the light yield. The

single-electron method compares the charge generated by the irradiation of known energy of a scintillator to the mean charge of a photoelectron spontaneously emitted by the photocathode [2].
The light yield measurements are performed with the crystal either horizontally or vertically positioned on the PMT. The set-up is shown in Fig. 3.1. In horizontal geometry the crystal is placed directly on the window of the PMT and centered above the photocathode to maximize the light collection on the cathode. It is optically coupled with silicone grease (Rhodorsil Silicones pâte 4) and covered with seven layers of Teflon^{TM} tape. The refractive index of the grease matches the refractive indices of the crystal and the window of the photomultiplier better than air. The angle of refraction between the different media is smaller and thus more photons are collected in the PMT.
In vertical geometry the crystal is wrapped in 6 cm of Teflon^{TM} tape, put in a Teflon^{TM} cylinder and the small end face is optically coupled to the PMT with silicone grease. In both cases the source is placed directly on top the crystal. A Cs-137 source with a monochromatic energy of 662 keV serves as γ excitation. The energy of the γ-particle is converted in the scintillator to visible photons. When a photon with enough energy reaches the photocathode of the PMT it knocks out a photoelectron, which gets amplified through several stages by the PMT. The signal from the PMT is first attenuated

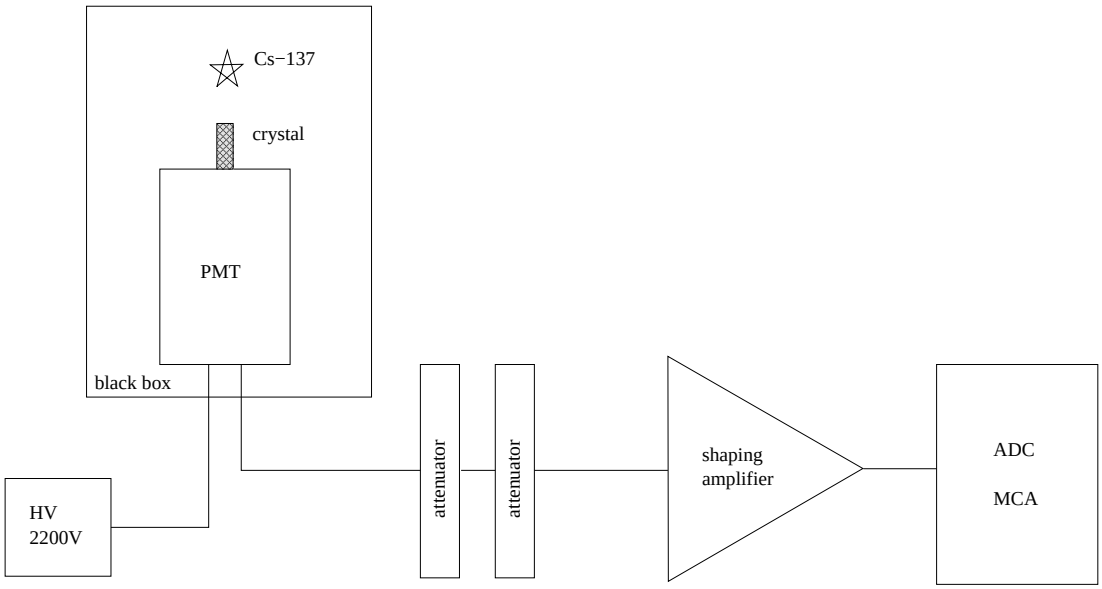

Figure 3.1: Schematic drawing of the light yield bench and data acquisition

(to be in the linear region of the shaping amplifier), fed into a shaping amplifier with 2.1 μs shaping time (to fulfil the input conditions of the analyser) and into an adjacent multi-channel analyser (MCA) and analogue-to-digital converter (ADC) (ORTEC TRUMP-PCI-8k) and PC. The acquisition and the parameters, such as delay and acquisition time, number of measurements, upper and lower discriminator are controlled from the PC with a software package called MAESTRO-32. The standard acquisition time is ten minutes and a minimum of three spectra is taken with each crystal to reduce

the measurement errors and the mean value is used for further discussion.
A typical photospectrum of a LuAP crystal is shown in Fig. 3.2. The number of pho-

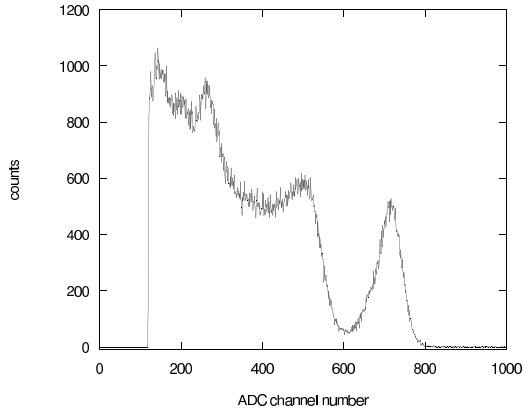

Figure 3.2: Typical photospectrum of a LuAP crystal acquired over ten minutes in horizontal geometry

toelectrons per energy unit is calculated using

$$N_{phe} = \frac{position\,of\,photopeak - pedestal}{position\,of\,single\,photoelectron\,peak - pedestal} \cdot \frac{A}{E_i} \tag{3.1}$$

The position of the photopeak is scaled up after the attenuation with an amplification A, given as

$$A = e^{\frac{dB}{20}} \tag{3.2}$$

and E_i the energy of the incident photon. The position of the photo peak and the single-electron peak are given in ADC channel numbers. The light yield of a scintillator is usually expressed as the number photons per MeV (N_{ph}/MeV). To convert the number of photoelectrons into photons the quantum efficiency (QE) of the PMT for the emission wavelength specific of the scintillator has to be known. In this study it is determined from the spectral sensitivity curves of the XP2020Q PMT provided by the producer [3]. The QE values used are 22 % and 25 % for L(Y)SO and Lu(Y)AP crystals respectively.

$$N_{ph}/MeV = \frac{N_{phe}}{QE} \tag{3.3}$$

To get the position of the peak, the main part of the energy spectrum was fitted with a Gaussian and a Fermi-function, which represents the background (eq. 3.4).

$$y(x) = \frac{p}{e^{\frac{(x-c)}{r}} + 1} + ae^{-\frac{(x-\mu)^2}{2\cdot\sigma^2}} \tag{3.4}$$

c is the calculated position of the Compton edge, p is the height of the Compton edge, $1/r$ is proportional to the slope and a is the height of the photo peak.

The energy resolution is also calculated from the Gaussian fit according to the conventional formula

$$R = \frac{FWHM\,of\,photopeak}{centroid\,of\,photopeak - pedestal} \tag{3.5}$$

As an indication of self-absorption the ratio between the light yields in vertical and horizontal positions is calculated.

3.2 Depth of interaction resolution

The goal of these measurements is to determine with which accuracy the coordinate along the crystal axis can be determined. For this purpose the crystal is excited only in a very small region and read out on both sides by photomultipliers.
The crystal is wrapped in Teflon^{TM} tape and mounted between two photomultiplier tubes. The PMTs are masked and optical grease is again used as coupling. Only a small section of the crystal is irradiated at once. The 511 keV γ-photons from a positron annihilation of a 3.8 MBq Na-22 source are electronically collimated into a beam. The collimation is achieved via a third scintillation crystal (BGO) coupled to a PMT positioned at a certain distance perpendicular to the crystal. All three PMTs are operated in coincidence (Fig. 3.3). This set-up allows only the photons produced in a small volume of the total crystal length to be studied. Whenever a positron annihilates in the plastic surrounding the Na-22 source, two 511 keV gammas are emitted in opposite directions. If one of the two γ-photons hits the BGO crystal, the second γ-photon will cause scintillation in a small volume of the crystal under study.
The beam width r results from the following geometric relation (3.6) and lies between 1.1 mm and 1.2 mm.

$$r = s + \frac{b}{a} \cdot (s + d) \tag{3.6}$$

s is the source diameter, a is the distance between the source and the surface of the BGO crystal on the third PMT, b is the distance between the source and the surface of the crystal between the first and second PMT and d is the side length of the BGO (see also Fig. 3.3). The values are listed in Table 3.1. To scan the whole crystal, the

Table 3.1: Tagging bench parameters

Parameter	Value
s	1 mm
a	900 mm
b	25 mm
d	6.3 mm

crystal and the two readout PMTs are mounted together on a support movable with a millimetre screw. The start position $z = 0\ mm$ is at the end of the crystal attached to PMT 1. The crystal, the source and the BGO are aligned with the aid of a laser. The particular crystal is wrapped in Teflon^{TM} and coupled to the PMTs with optical grease. Measurements are performed with the excitation of the crystal by the collimated beam at five different positions, $z = 2\ mm$, $z = 5\ mm$, $z = 10\ mm$, $z = 15\ mm$ and $z = 18\ mm$. The start position $z = 0\ mm$ is assigned to the end of the crystal closest to

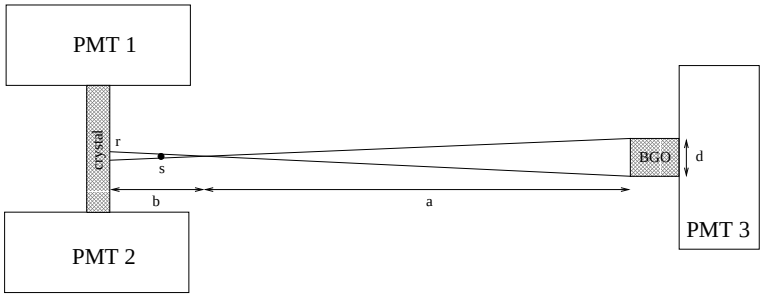

Figure 3.3: Schematic drawing of the tagging bench

PMT 1. Two spectra are recorded at each position on the scope (see Fig. 3.5). Fig. 3.4 shows an example of such spectra. Depending on the distance of the interaction point

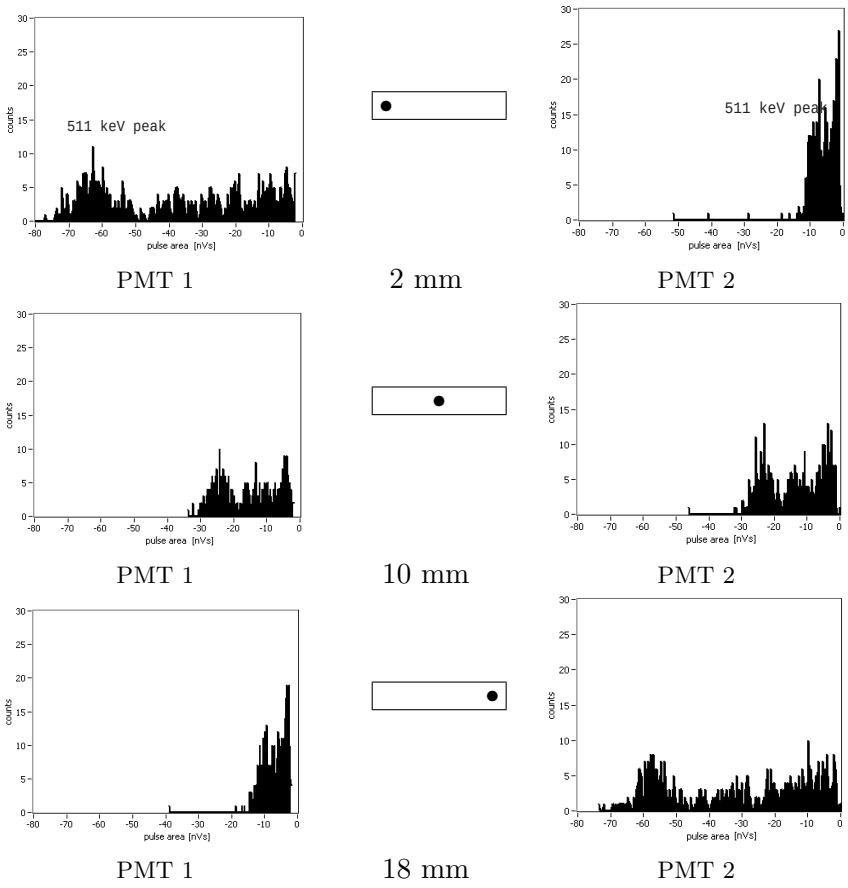

Figure 3.4: Series of light yield spectra taken at both ends of the crystal. the crystal is excited by the collimated γ-beam at three different positions along the crystal axis (z=2 mm, z=10 mm, z=18 mm)

to the PMT more or less light is collected and the position of the photopeak moves to

higher or lower values accordingly. The position of the photopeak relative to the centre of the crystal is plotted versus the position on the crystal axis. The data points are fitted with an exponential function:

$$N(z) = N_0 e^{-\frac{z}{\lambda_{eff}}} \tag{3.7}$$

Data acquisition is done with standard NIM electronic modules (Fig. 3.5) and a digital oscilloscope (Lecroy LT 344 waverunner series). The trigger is provided by the coincidence signal from all three PMTs. 500 pulses are recorded for both readout PMTs on the scope and further processed with a LabVIEW programme.
The data are analysed with a LabVIEW routine that creates three spectra: one spec-

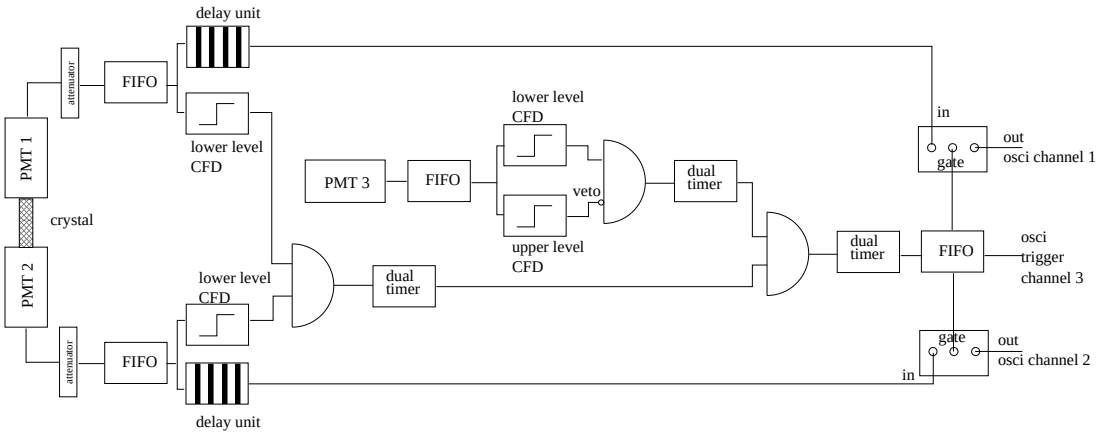

Figure 3.5: Schematic drawing of the tagging bench data acquisition

trum of the pulses from the PMTs at each end of the crystal (PMT 1 and PMT 2) and a sum spectrum (PMT 1 + PMT 2). The photopeaks of each spectrum are fitted with a Gaussian and the mean values μ_1 and μ_2 (centroid of the photopeak) and the standard deviations σ_1 and σ_2 are extracted. Then the asymmetry α is calculated pulse by pulse. Only pulses that lie in the interval $\mu_i \pm \sigma_i$ (i = 1 and 2) of their respective photopeaks are selected. α is calculated with

$$\alpha = \frac{LY_1 - LY_2}{LY_1 + LY_2} \tag{3.8}$$

The result is again plotted as a histogram and fitted with a Gaussian to obtain the mean and FWHM for α.

The asymmetry values are plotted versus the position in the crystal. The data points are fitted with a straight line. The DOI resolution is estimated by the slope of the linear fit of the asymmetry curve divided by the FWHM asymmetry peak.
The precision of the reconstruction of the coordinate of the interaction depends on the position of the excitation on the crystal, the light attenuation coefficient and the number of photons and their fluctuations. For the exact expression confer section 2.5.3.

The total energy deposited and the energy resolution for each position is derived from the sum spectrum.

3.3 Decay time

The decay time is measured based on the single photon counting technique first described by Bollinger and Thomas [4]. This method works by sampling the physical decay time process by measuring the arrival time of individual photons from the scintillator crystal after excitation. The crystal under investigation is placed on top of the Na-22 source between two PMTs perpendicular to each other. Fig. 3.6 shows a schematic drawing of the deacy time bench. A fast plastic scintillator is in contact

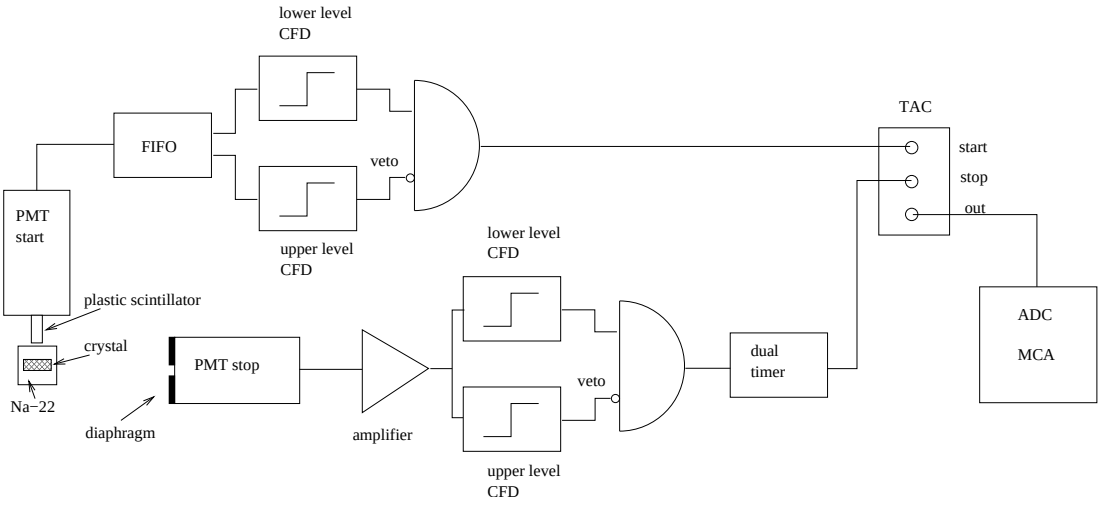

Figure 3.6: Schematic drawing of the decay time bench and data acquisition

with the PMT directly below the source. A positron emitted by the sodium annihilates with an electron and produces two collinear photons. One produces a light pulse in the plastic scintillator, which triggers the start signal, and the other excites the crystal. Eventually one photon produced in the crystal reaches the second PMT and sends the stop signal. The time difference is converted into an amplitude. The Maestro software is used to acquire and visualize the spectra. A conceptual spectrum composed of two components is drawn in Fig. 3.7. The decay time spectra are fitted with an exponential function in the case of L(Y)SO crystals (eq. 3.9) and with the sum of two exponentials in the case of Lu(Y)AP crystals (eq. 3.10) from 0 ns to 1600 ns.

$$N(t) = A_1 e^{-\frac{t}{\tau_1}} \tag{3.9}$$

$$N(t) = y_0 + A_1 e^{-\frac{t}{\tau_1}} + A_2 e^{-\frac{t}{\tau_2}} \tag{3.10}$$

y_0 represents the background, τ the time constants and A the amplitudes.

The ratio of the integral over the decay time curves for each time constant (τ_1 and τ_2) and the integral over the sum gives the fraction of light carried by each component (eq. 3.11). The upper limit of the integral is 150 ns, 300 ns or 1600 ns. These values are chosen because at 150 ns the ClearPET distinguishes between a pulse from a LSO

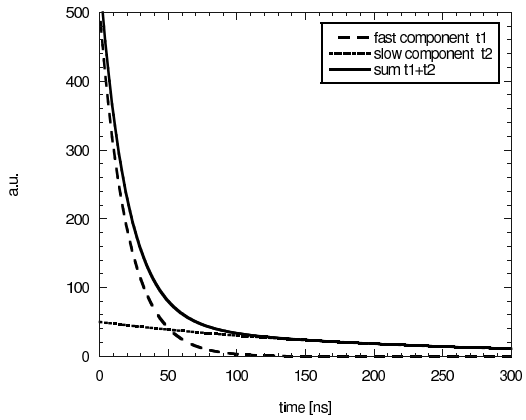

Figure 3.7: DT composed of two components

or LuAP crystal and after 1600 ns all the photons are emitted. The ratio between the overall light emitted after 300 ns and 1600 ns gives the percentage of light already released after 300 ns.

$$F_i = \frac{\int_0^t A_i e^{-\frac{t}{\tau_i}}\, dt}{\int_0^t A_1 e^{-\frac{t}{\tau_1}} + A_2 e^{-\frac{t}{\tau_2}}\, dt} \tag{3.11}$$

Three spectra are taken for each sample with approximately 10 events per second, requiring data taking for two hours each.

3.4 Transmission

The spectrophotometer compares the intensity of a monochromatic light beam passing through the crystal with its initial intensity. The transmission is scanned through a range of wavelengths around the emission wavelength of the scintillation light. The typical spectrum is recorded from 250 nm to 600 nm in 5 nm steps. The set-up of the system,shown in Fig. 3.8, includes a 150 W Xenon lamp serving as a light source. The emitted light from the lamp passes through several UV lenses and mirrors to focus and collimate the beam, as well as a monochromator and filters to eliminate upper order diffractions originating from the monochromator. The beam is split in two: the reference beam is deflected to pass above the crystal and the measurement beam passes through the crystal. A chopper with a rotational frequency of 50 Hz blocks alternatingly one beam from reaching the PMT. A white box around the PMT diffuses the light to ensure a uniform irradiation of the photocathode.
Before the measurements a reference spectrum without the crystal is recorded. It shows the intensity variations of the Xenon lamp with λ and is used to normalize the transmission spectra. The settings of the spectrophotometer, the data acquisition and analysis are automatically operated by a LabVIEW program.
For longitudinal transmission the beam enters via the small face and passes through

its total length. For a transversal measurement the crystal is placed perpendicular to the beam and the light goes only through the width of the crystal. The transmission

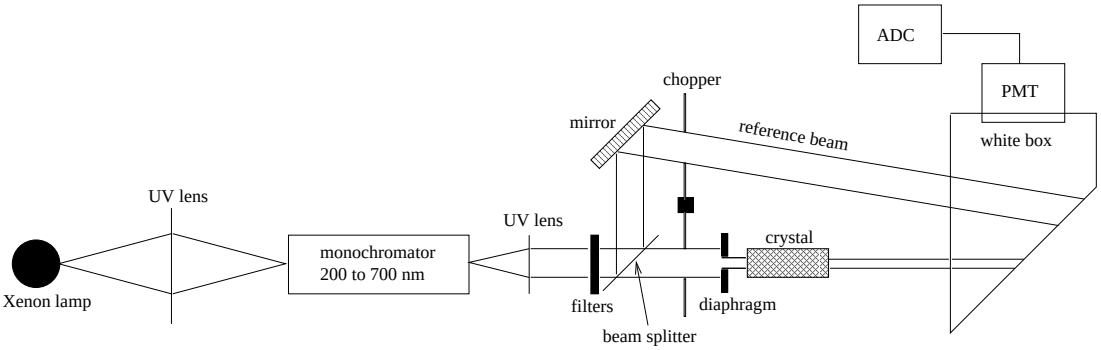

Figure 3.8: Schematic drawing of the spectrophotometer

spectrum is fitted with the equation [5]

$$T(\lambda) = p_3 e^{-e^{-\frac{\lambda - p_1}{p_2}}} \tag{3.12}$$

where p_1 is the cut-off wavelength and $1/p_2$ is proportional to the slope at the cut-off wavelength. The first and second derivatives are calculated to obtain the turning point of the curve (which is equal to the cut-off wavelength of the transmission) and the slope at the turning point.

Bibliography

[1] E.Sysoeva, V.Tarasov, O.Zelenskaya, Comparison of the methods for determination of scintillation light yield. Nucl Instr and Meth A 486 (2002) 67.

[2] M. Bertolaccini, S. Cova, C. Bussolati, A technique for absolute measurement of the effective photoelectron per keV yield in scintillation counters. Proc Nucl Electr Symp, paper no 8, Versailles, France 1968.

[3] Philips Photomultiplier Catalogue, 1990.

[4] L.M.Bollinger, G.E.Thomas, Measurement of the Time Dependence of Scintillation Intensity by a Delayed-Coincidence Method. Rev Sci Instrum 32 9 (1961) 1044.

[5] M.Montecchi, CMS Internal Note 2000/015.

Chapter 4

Results of the measurements of scintillator crystals

In this study scintillation materials from three different producers are compared to understand better the scintillation characteristics of the crystals, how these characteristics are influenced by their production history and how to improve their properties. What matters in the end is to find the most suitable material available.
Measurements of the light yield and non-proportionality, decay time and transmission are carried out on LuAP:Ce and mixed LuYAP:Ce crystals, which are new scintillation materials. The purpose is to compare the properties of these two crystals with respect to each other and to evaluate LuAP and LuYAP crystals produced by the Institute for Physical Research (IPR), Armenia in comparison to the crystals commercially available from Photonic Materials Ltd. (PML), Glasgow, UK as well as from the Bogoroditsk Techno Chemical Plant (BCTP) in Russia. On one side there are two commercial companies BTCP and PML and on the other side an independent research institute IPR. BTCP is an already well established crystal growing company which is not the case PML. Both companies have already provided crystals for the ClearPET, so a comparison of crystal characteristics suggests itself. At IPR fundamental research of scintillating materials is done to understand and ameliorate scintillation properties.
A second difference between the three producers is the production technique. There are two standard crystal-growing procedures: the Czochralski method, used by PML and BTCP, which produces crystals with small cerium concentration variations in the different samples; and the Bridgman-Stockbarger technique, used by the IPR where the cerium content in each sample may vary to a larger extent.
The cooperation with IPR led to a study of the influence of the cerium concentration on the crystal properties to understand in depth the properties of LuAP and the optimization in particular of the light yield.
The results are discussed in detail in the following sections and in [1]. All results are summarized in Appendix A.

A second study is performed on the depth of interaction (DOI) resolution of 20 mm

long LuAP and LYSO crystal pixels. The longer crystals are used in the ClearPEM and read out at both ends to determine at which position in the crystal the interaction with the γ-particle has occurred. A high DOI resolution is desired because this information reduces greatly the artefacts in an reconstructed image.

4.1 Materials

LuAP is a relatively new scintillation material [2]. LuAP crystals combine a high light yield, good energy resolution, short decay time and a good transparency at the wavelength of its own scintillation light at 365nm. However, LuAP crystals only show good scintillation properties in one of its three crystallographic phases: the Perovskite, which is difficult to grow, because its phase space in the phase diagram (cf. Fig. 1.1 inside the circle) is very limited and it is very sensitive to temperature variations. The addition

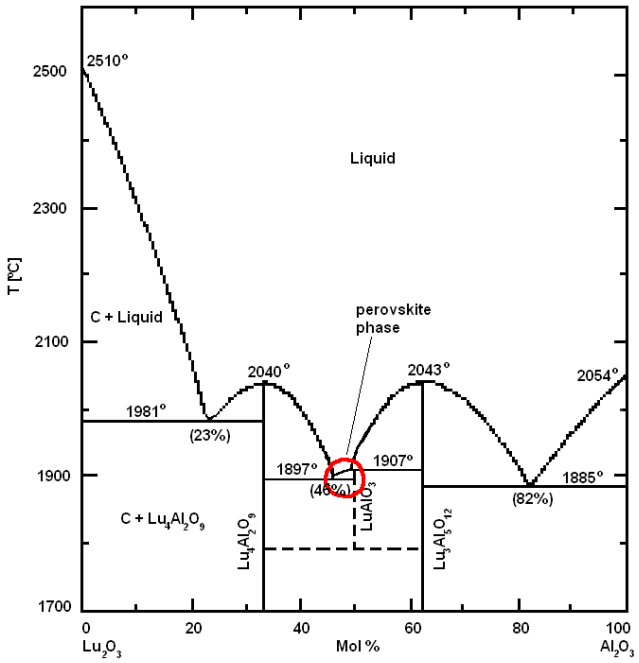

Figure 4.1: Calculated phase diagram for the Lu_2O_3-Al_2O_3 system [3]

of 30% to 35% of yttrium to the melt makes the crystal growth and the phase stability easier, at the price of a slightly reduced density. The crystal is then referred to as LuYAP. In addition a small amount of cerium (between 0.16% and 0.44%) has been included as well, which acts as an activator for the scintillation process.

The study was carried out on 157 LuAP and 12 LuYAP pixels (2 x 2 x 8 mm^3) from

IPR, 150 LuAP (2 x 2 x 8 mm^3) and 11 LuYAP pixels (2 x 2 x 10 mm^3) from PML and 20 LuYAP from BTCP , optically polished on all faces. For each study different crystals were chosen at random from these batches. The yttrium concentration in the IPR and BTCP pixels was 30% and in the PML pixels 35%. Only IPR provided the cerium concentration (Table A.2 in Appendix A). LuYAP crystals from IPR were intentionally doped with different cerium concentrations for studies on concentration dependence of optical and scintillation parameters.

4.2 Light yield and energy resolution

The light yield is measured in horizontal and vertical position (cp. 3.1).
For the light yield measurements 24 LuAP from PML and 41 from IPR were randomly selected from two batches. All 11 LuYAP crystals from PML, all 12 LuYAP from IPR) and also all 20 LuYAP from BTCP were used.
An example of a light yield spectrum of a crystal in horizontal and vertical positions is shown in Fig. 1.2 (a). The position of the photopeak measured in ADC channels is proportional to the light yield. The ratio between the light yield in horizontal and vertical position can be used to estimate the light absorption in the crystal. The full width of the peak at half the height (FWHM) together with the peak position give information about the energy resolution. Due to impurities or defects in the crystal the photopeak becomes broader or even splits into two peaks. The position and width of the photopeak are less defined and as a consequence the energy resolution becomes worse. For some of the LuAP crystals from IPR double peaks are observed in the light yield spectrum (Fig. 1.2 (b)). They can be found both in horizontal and/or vertical

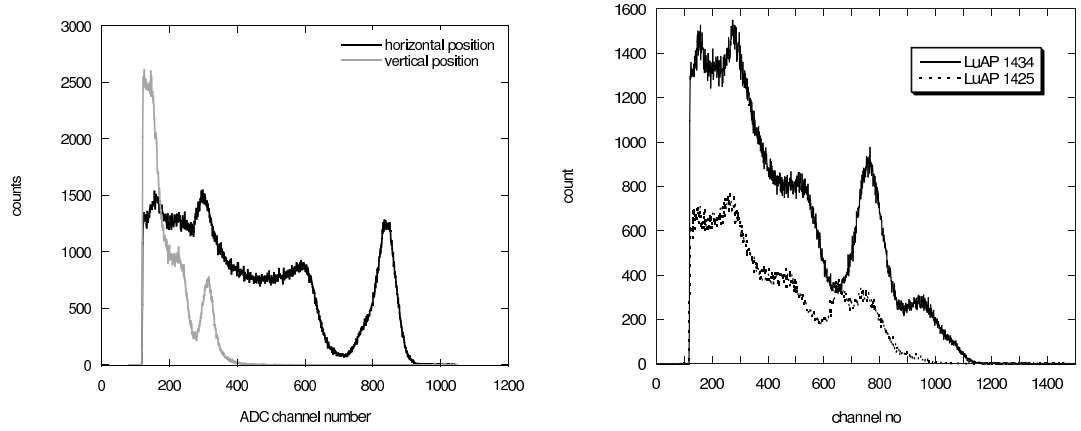

(a) (b)

Figure 4.2: Example of a light yield spectrum of a crystal taken in horizontal and vertical geometry (a) and two spectra in which double peaks appear

position (9 out of 30 crystals display well distinguishable double peaks and another 9 have suspiciously looking peaks, which look like an overlap of two peaks). Their light

output is comparable to the others, but their energy resolution is worse. Fig. 1.3 shows the correlation between the light yield and the energy resolution. It follows the expected $1/\sqrt{N_{ph}}$ relation. The correlations are good for all but LuAP crystals from IPR due to the double peaks in their energy spectra. The double peaks can be attributed to

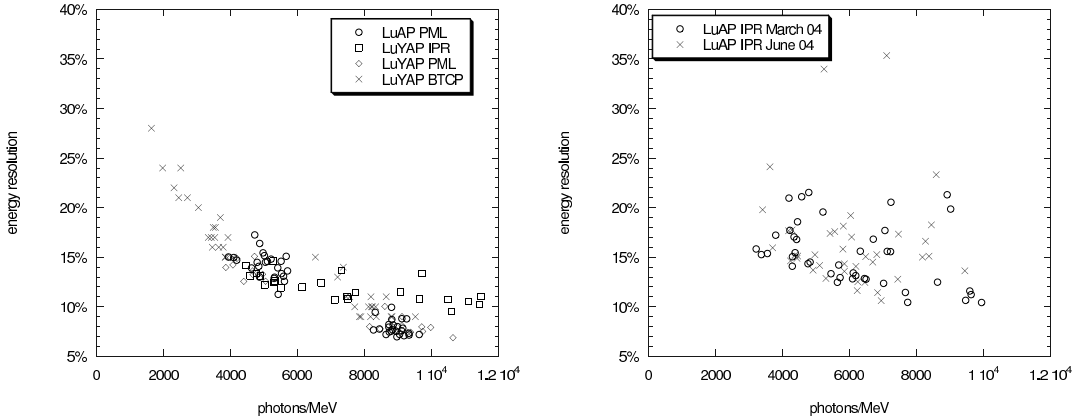

(a) (b)

Figure 4.3: Correlation between the light yield and energy resolution for LuAP and LuYAP (without double peaks in the light yield spectra) (a) and LuAP from IPR (with double peaks in the light yield spectra) (b)

inhomogeneities of the crystalline structure leading to more than one domain in the pixels. This is likely to happen in crystals which are not seeded. None of the LuYAP exhibited crystals double peaks in their spectra, although they were grown with the same technique. This may be attributed to the yttrium, which is added to stabilize the crystal growth.

4.2.1 LuAP

Fig. 1.4 (a) and (b) show the distributions of the light yields in vertical and horizontal positions of the LuAP crystals from the two producers. In vertical position LuAP pixels from both producers have a comparable light yield, but in horizontal geometry the LuAP PML are much better than LuAP from IPR. Balcerzyk et al. studied LuAP crystals also from PML of the same dimensions [4]. Their results for light yield and energy resolution are almost the same as for the LuAP crystals from this study.
Considering the energy resolution (the distributions are represented in Fig. 1.5 (a) and (b)) in vertical and horizontal geometry the PML crystals show the best results with an average of 8%. LuAP IPR crystals have lower energy resolution. In the case of LuAP IPR it is caused by the presence of double peaks in some spectra. The ratio of the light yield in vertical versus horizontal position (Fig. 1.6)is a measure for the absorption in the crystal. The closer it is to one, the smaller the light absorption. Therefore LuAP PML have a stronger light absorption than LuAP IPR. For IPR crystals an improvement was observed between the March and June production in 2004.

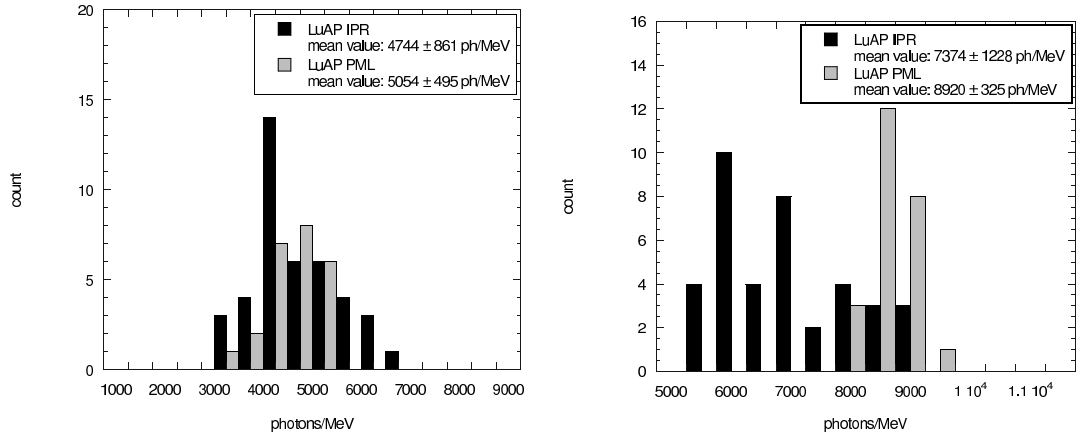

(a) (b)

Figure 4.4: Distribution of the light yield of LuAP in vertical (a) and horizontal (b) position

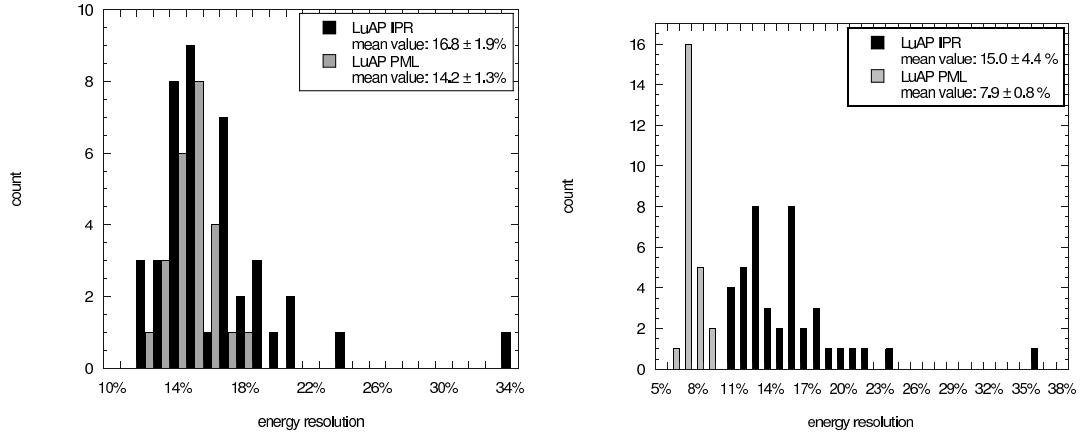

(a) (b)

Figure 4.5: Distribution of the energy resolution of LuAP in vertical (a) and horizontal (b) position

4.2.2 LuYAP

Fig. 1.7 (a) and (b) show the distributions of the light yields in vertical and horizontal positions of the LuYAP crystals from two producers. The LuYAP crystals from IPR are not included because they do not have the same length as the other LuYAP pixels and thus less absorption. PML samples show a higher light yield and better energy resolution in both vertical and horizontal position than BTCP pixels. The distributions of the energy resolution are represented in Fig. 1.8 (a) and (b) in vertical and horizontal geometry. In vertical geometry (Fig. 1.8 (a)) the energy resolution of LuYAP from PML and IPR is comparable within the standard deviation and the pixels' lengths.
Regarding the ratio of the light yield and therefore the absorption (Fig. 1.9) LuYAP

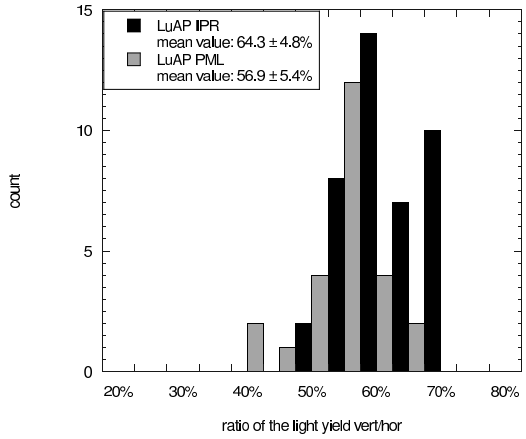

Figure 4.6: Distribution of the ratio of the light yield in vertical versus horizontal position for LuYAP crystals

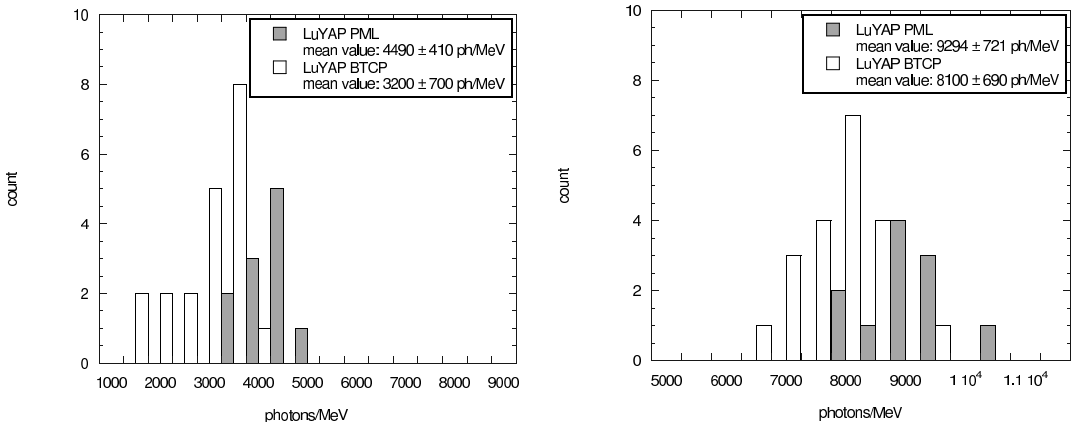

(a) (b)

Figure 4.7: Distribution of the light yield of LuYAP in vertical (a) and horizontal (b) position

BTCP have the strongest light absorption, followed by LuYAP PML and LuYAP IPR.

4.3 Non-proportionality and energy resolution

To compare the non-proportional energy response of the different crystals and producers, the light yield is measured with radioactive sources of different energies. The used sources and corresponding energies can be found in Table 1.1. The light yield at a certain energy is normalized to the light yield at the 662 keV γ-energy of Cs-137 [5]. The same is done for the energy resolution. Following [5] the energy resolution is presented together with the calculated intrinsic resolution as well as the statistical term origi-

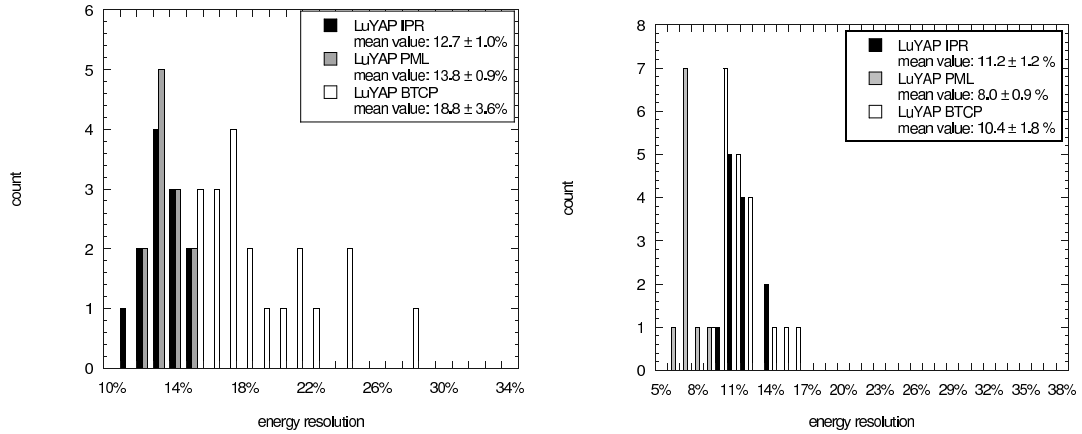

(a) (b)

Figure 4.8: Distribution of the energy resolution of LuYAP in vertical (a) and horizontal (b) position

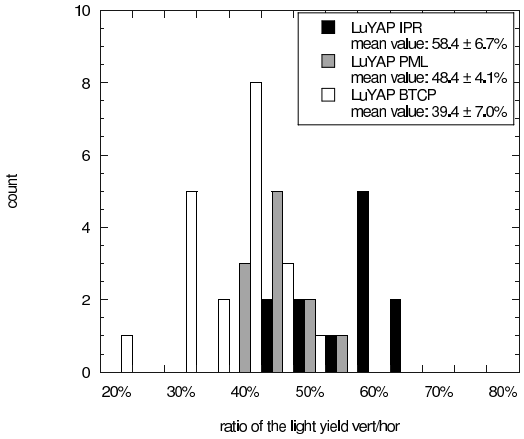

Figure 4.9: Distribution of the ratio of the light yield in vertical versus horizontal position for LuYAP crystals

nating from the photomultiplier (cf. section 2.5.2). All measurements were performed in horizontal geometry. The crystal with the highest light yield in horizontal position was chosen from each batch. As a different way to compare the individual scintillators, Dorenbos [6] proposed to calculate the degree of non-proportionality σ_{np}:

$$\sigma_{np} = \sqrt{\frac{1}{N} \sum_{i=1}^{N} \left(\frac{Y(E_i)}{Y(662)} - 1 \right)^2} \tag{4.1}$$

where $Y(E_i)$ is the light yield at energy E_i and $Y(662)$ is the light yield at 662 keV from Cs-137.
At the end of this section the results for a LYSO crystal are shown for comparison.

Table 4.1: Used radioactive sources and their γ-ray energies

Isotope	Energy of the photo peak [keV]
Cs-137	662
Na-22	1275
	511
Ba-133	356
	302
	81
	31
Co-57	122
Co-60	1333
	1173
Mn-54	835
Cd-109	88
Am-241	60

4.3.1 LuAP

Fig. 1.10 shows the relative light output at different excitation energies for the LuAP crystals. The value at 662 keV is taken as reference (100%). The relative light yield is

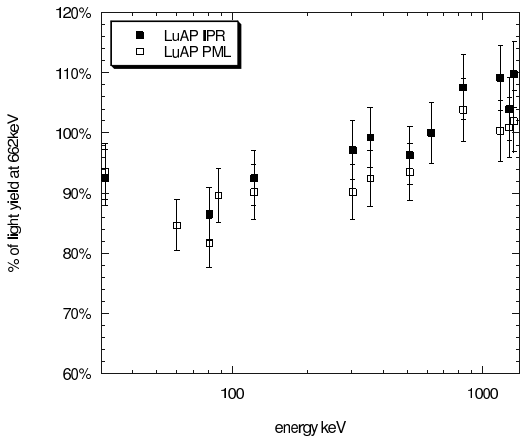

Figure 4.10: Non-proportional response of the light yield to different excitation energies of a LuAP crystal

fairly constant and starts to decrease below 662 keV towards lower energies. A minimum is reached at the K edge of Lutetium at 63keV. The light yield varies between 75% and 110% compared to the light yield obtained with Cs-137 662 keV γ-rays.
The non-proportionality is also found in the energy resolution (Fig. 1.11 (a) and (b)). In these plots the contribution to the energy resolution from the crystal (intrinsic resolution) and the statistical term and the total energy resolution are plotted together.

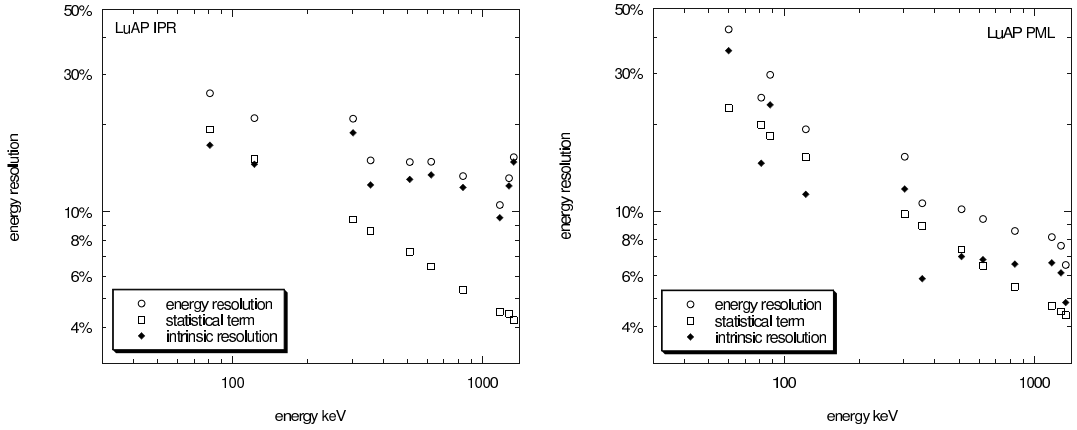

(a) (b)

Figure 4.11: Total energy resolution, statistical term and intrinsic resolution of the crystal at different excitation energies of a LuAP crystal from IPR (a) and PML (b)

In a double logarithmic graph the statistical term decreases linearly with increasing energy. The intrinsic resolution becomes constant at around 400 keV for LuAP PML crystals and is almost constant over the whole range for LuAP IPR. This indicates that the energy resolution is mainly governed by the statistical resolution below 400 keV.

4.3.2 LuYAP

The results in Fig. 1.12 for LuYAP crystals are similar to the results above for LuAP crystals. The same decrease of relative light output with decreasing excitation energy is found. The statistical term decreases with increasing energy for crystals produced by

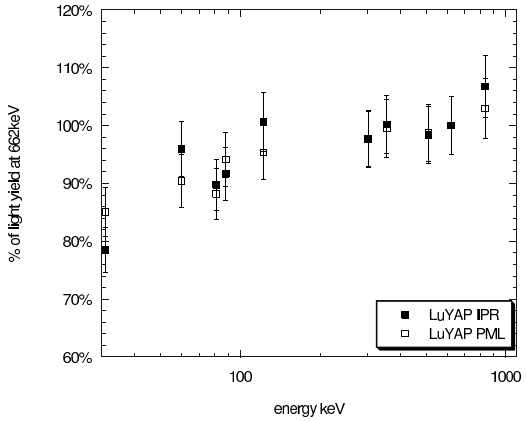

Figure 4.12: Non-proportional response of the light yield to different excitation energies of a LuYAP crystal

IPR and PML. After an initial decrease the intrinsic resolution becomes constant at

around 200 keV for LuYAP IPR crystal whereas it keeps decreasing for PML pixels and even lies below the statistical term. For these crystals the photomultiplier resolution does not have such a big influence.

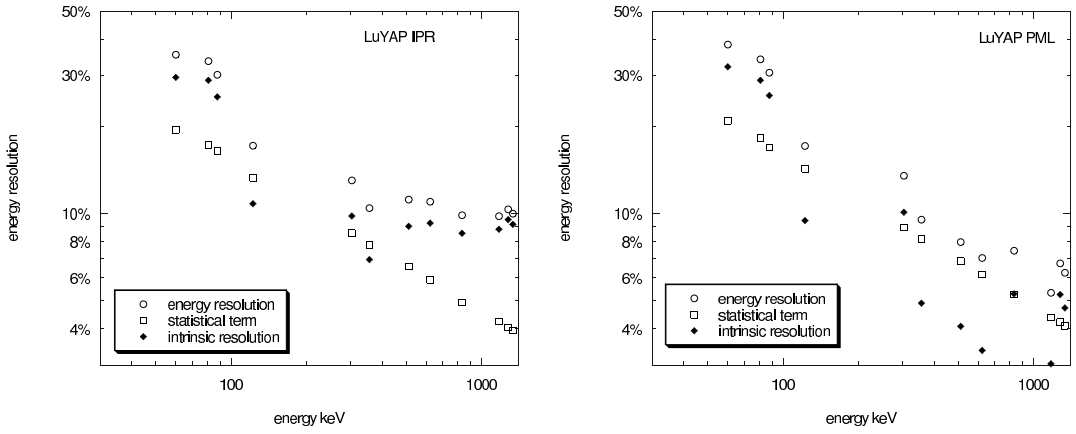

(a) (b)

Figure 4.13: Total energy resolution, statistical term and intrinsic resolution of the crystal at different excitation energies of a LuYAP crystal from IPR (a) and PML (b)

4.3.3 Comparison of LuAP and LuYAP to LYSO

The relative response of the light yield and the energy resolution for a LYSO crystal is plotted in Fig. 1.14 (a) and (b). The LYSO light yield drops to 50% at 31 keV; for

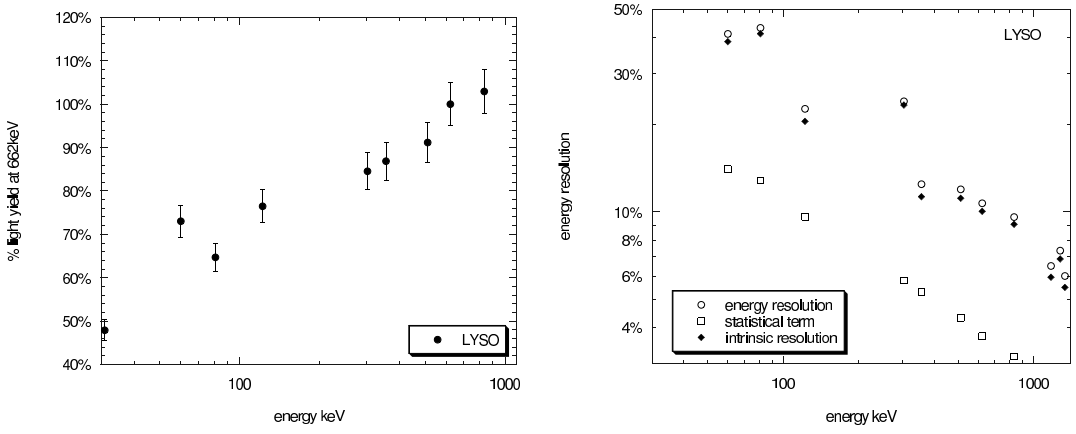

(a) (b)

Figure 4.14: Non-proportional response of the light yield (a) and the total energy resolution, statistical term and intrinsic resolution of the crystal at different excitation energies of a LYSO crystal

the LuAP and LuYAP crystals the decrease is less pronounced. The light yield does not decrease to less than 80%-85% for LuAP and LuYAP. For energy resolution the statistical term plays an important role in for the LuAP and LuYAP crystal but is less important for LYSO. The LYSO energy resolution is more affected by the intrinsic resolution. The measured curves are less flat than those reported by Kuntner et al [7] and Balcerzyk et al [4], but the decrease in light yield is similar.
Coming back to the degree of non-proportionality, the values for σ_{np} have been calculated for all five crystals. The σ_{np} values obtained were 0.072 for LuAP IPR, 0.089 for LuAP PML, 0.076 and 0.068 for LuYAP IPR and PML respectively and 0.220 for LYSO. Kuntner et al [7] found a value of 0.054 for a LuYAP from BTCP. Both types of crystals from both producers show a small degree of proprotionality and are superior to LYSO.

4.4 Decay time

For the decay time measurements 13 LuAP crystals from PML and 32 from IPR were randomly selected out of the two batches. All 11 LuYAP crystals from PML, all 12 from IPR and 16 LuYAP from BTCP were used.

4.4.1 LuAP

The values of the fast and slow time constants of the decay time of the LuAP crystals are reproduced in Fig. 1.15 (a) and (b). The fast components are comparable. Also the

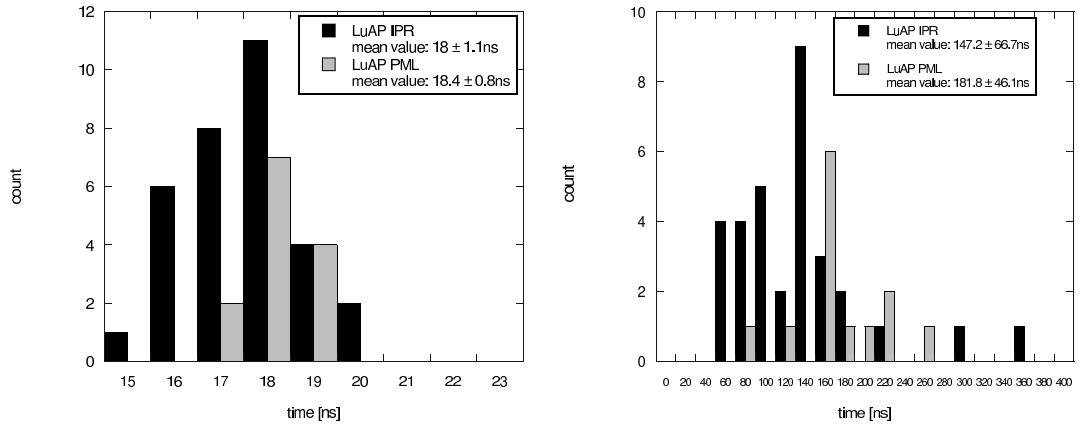

(a) (b)

Figure 4.15: Distribution of the fast (a) and slow (b) time constant of the decay time of LuAP crystals

slow component of LuAP IPR is not significantly shorter than the slow component of

LuAP PML. 80% of light lies in the fast component for the crystals of both producers (Fig. 1.16) and only 20% in the slow one.

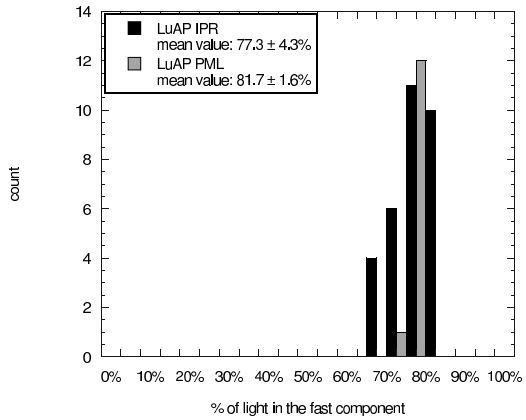

Figure 4.16: Distribution of the percentage of light in the fast component of LuAP crystals

4.4.2 LuYAP

The differences in the time constants between the three producers are marginal, which is clear from the distributions of the time constants in Fig. 1.17. The measurement error is less than 5% for the fast component and approximatly 10% for the slow component. For LuYAP PML and IPR crystals the amount of light in each component is almost

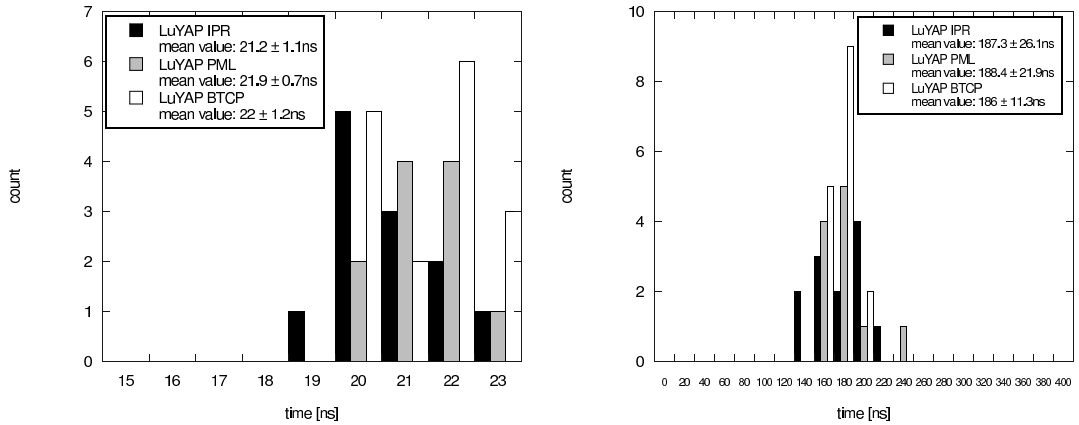

(a) (b)

Figure 4.17: Distribution of the fast (a) and slow (b) time constant of the decay time of LuYAP crystals

equal and for LuYAP crystals from BTCP there is less light in the fast component

(40%) than in the slow one (60%). The distribution of the percentage of light in the fast component is shown in Fig. 1.18.

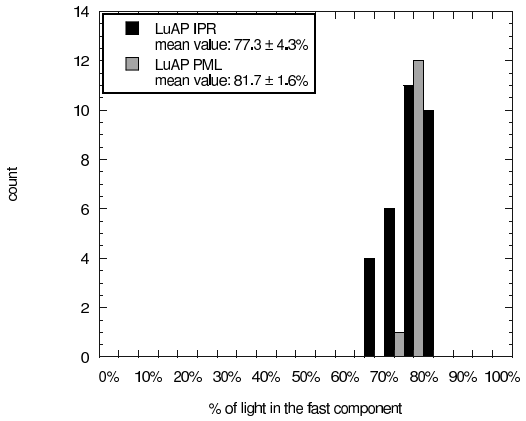

Figure 4.18: Distribution of the percentage of light in the fast component of LuYAP crystals

4.4.3 Comparison of LuAP and LuYAP

Compared to LuYAP, LuAP crystals have a faster time constant for both, the fast and the slow component. Regarding the percentage of light in each component, a big difference between LuAP and LuYAP crystals is observed. For LuAP crystals 80% of the light is emitted in the fast whilst for LuYAP it is close to 50%.
The "faster" slow component of the LuAP and the high percentage of light in the fast component gives LuAP crystals an advantage over LuYAP crystals. For most applications a slow component is not desirable because it deteriorates the timing behaviour and causes longer dead times. Researchers aim for complete suppression of the slow component in LuAP and LuYAP crystals. One exception is the ClearPET, where the slow component is used to obtain depth of interaction information.

4.5 Transmission

For the transmission measurements 25 LuAP from PML and 147 from IPR were randomly selected out of the two batches. All 11 LuYAP crystals from PML, all 12 from IPR and all 20 LuYAP from BTCP were used.
The transmission curves in Fig. 1.19 were calculated using the average value of each fit parameter for each type of crystal in longitudinal position. The band edge of IPR crystals (LuAP and LuYAP) is clearly at lower wavelengths than the band edge of the crystals produced by PML and BTCP. The distributions of the longitudinal cut-off wavelength are shown in Fig. 1.20 (a) and (b). The values of the cut-off wavelength are higher for PML and BTCP crystals. That means that these crystals have a higher

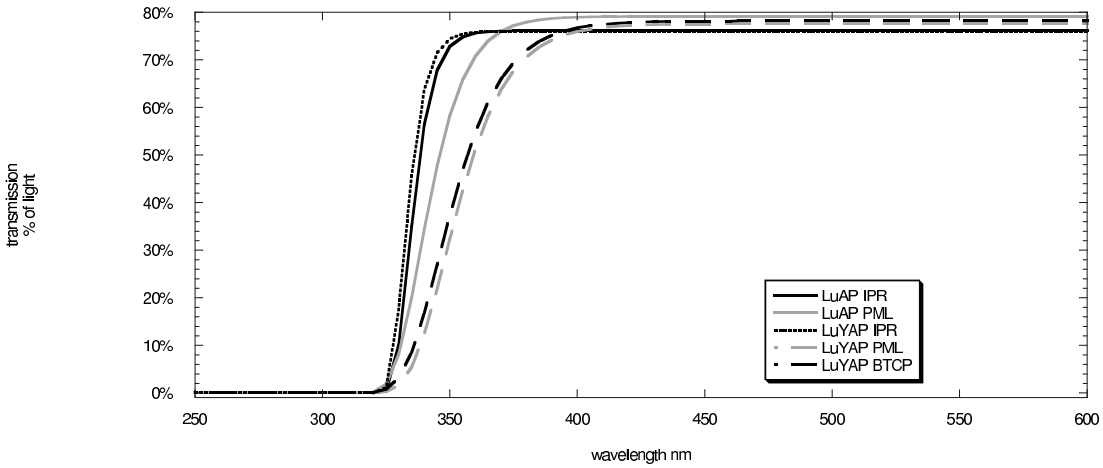

Figure 4.19: Averaged transmission spectra for LuAP and LuYAP crystal from all three producers

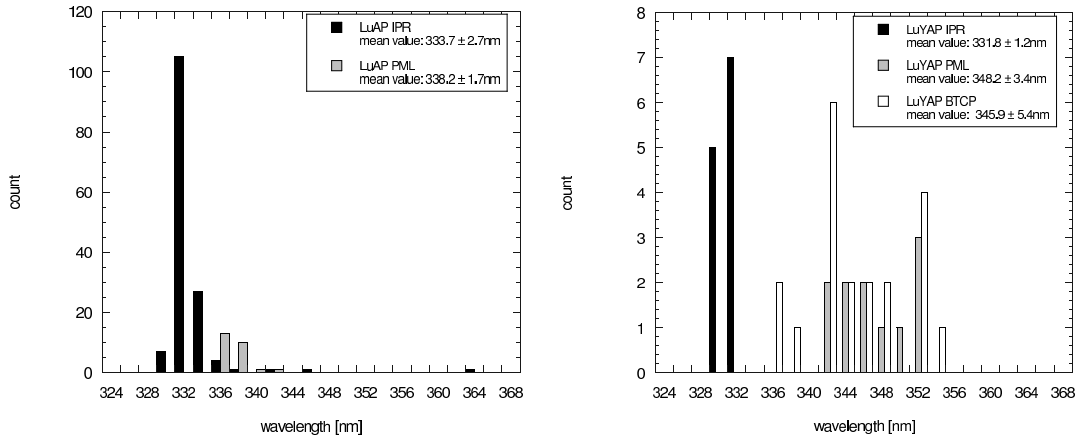

(a) (b)

Figure 4.20: Distribution of the longitudinal cut-off wavelength of LuAP (a) and LuYAP (b) crystals

absorption and is in agreement with the ratio of the light yield in vertical and horizontal position. This correlation between the cut-off wavelength for longitudinal transmission and the ratio of the light yield in vertical and horizontal position is shown in Fig. 1.21. The plot shows that a high ratio of vertical over horizontal light yields corresponds to a shorter cut-off wavelength. The correlation confirms that IPR crystals have less absorption (high light yield ratio and low band edge).

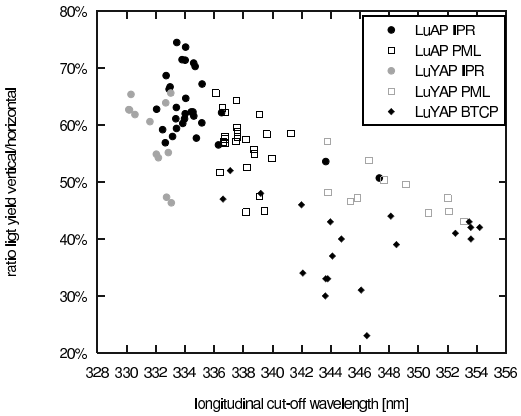

Figure 4.21: Correlation between the longitudinal cut-off wavelength and the ratio of the light yield in vertical over horizontal position

4.6 Influence of the cerium concentration

Together with A.Petrosyan from the Institute for Physical Research in Armenia the influence of the cerium concentration in the crystals on the light yield, time properties and absorption was studied. Two series of crystals with an increasing percentage of cerium were produced. All results are summarized in Appendix A Table A.2.
The cerium content varies between 0.22% and 0.42% in LuAP crystals and between 0.16% and 0.44% in LuYAP.
In Fig. 1.22 (a) and (b) the correlation between the light yield (measured in vertical and horizontal position) and the content of cerium is plotted. The light yield increases with

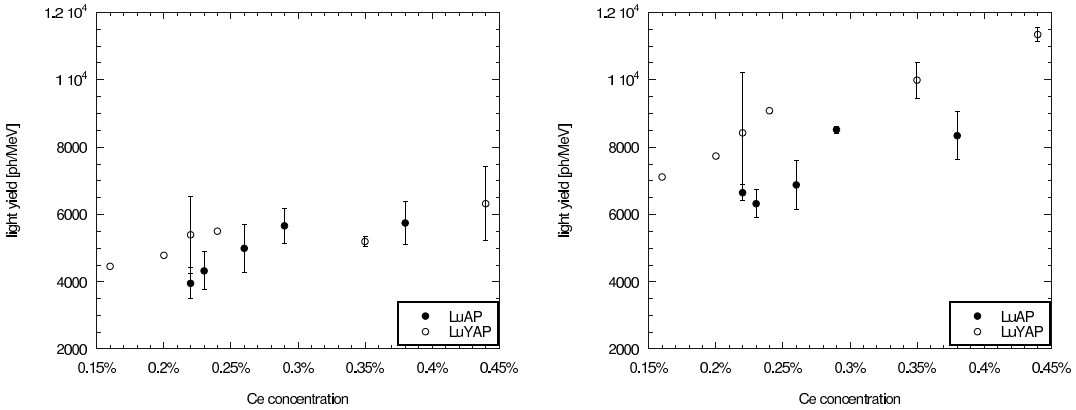

Figure 4.22: Correlation between the cerium concentration in the crystal and the light yield measured in vertical (a) and horizontal (b) position

the percentage of cerium in the crystal until a certain point because the cerium atoms are the main centres of scintillation light production. At a higher concentration the

curve for LuAP and LuYAP seems to reach saturation. Measurements with crystals with a cerium content higher than 0.44% are needed to confirm or disprove the assumpption of the light yield saturation. The same shape can be found in Dujardin et al [8] with the drop at a different concentration, but also the excitation energy was different (122 keV from Co-57). The shape of the light yield dependency curve is similar to the one found in Petrosyan et al [9], where they compare the position of the photo peak as a function of Ce-concentration. Unfortunately no clear conclusion can be made at this point, before crystals with an even higher Ce-concentration have been measured.
The Ce-concentration has a great influence on the time constants. There is a strong correlation between the timing properties and the cerium content is found, shown in Fig. 1.23 for the fast (a) and the slow (b) component of the decay time. The more cerium

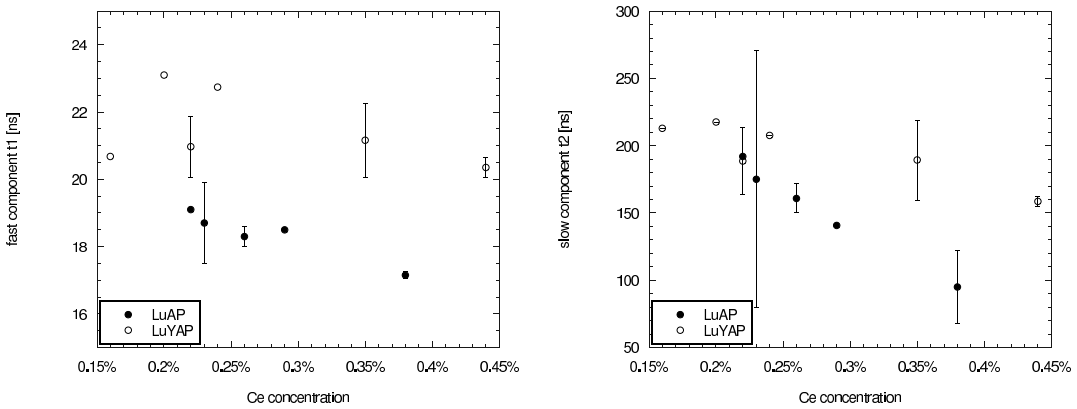

Figure 4.23: Correlation between the cerium concentration in the crystal and the fast (a) and slow (b) time constant of the decay time

in the crystals, the faster the light decays, probably due to concentration quenching.
For each cerium concentration the average of the fit parameters was calculated and then used to plot the transmission curves. Fig. 1.24 (a) and (b) show the part of the transmission curves close to the cut-off wavelength. The order of the curves from top to bottom follows the increase in cerium in the crystal. It is found that the cut-off wavelength and the absorption increases with the increasing percentage of cerium. Fig. 1.25 shows the correlation between the cerium concentration and the longitudinal cut-off wavelength. Since the light yield increases as well active absorption takes place in these cases. The photons get re-emitted after absorption by the fluorescence centres. Balcerzyk et al [4] suggest that the absorption is not chiefly dependent on cerium doping but on the properties of the host crystal itself. However, their study was performed with crystals from PML.

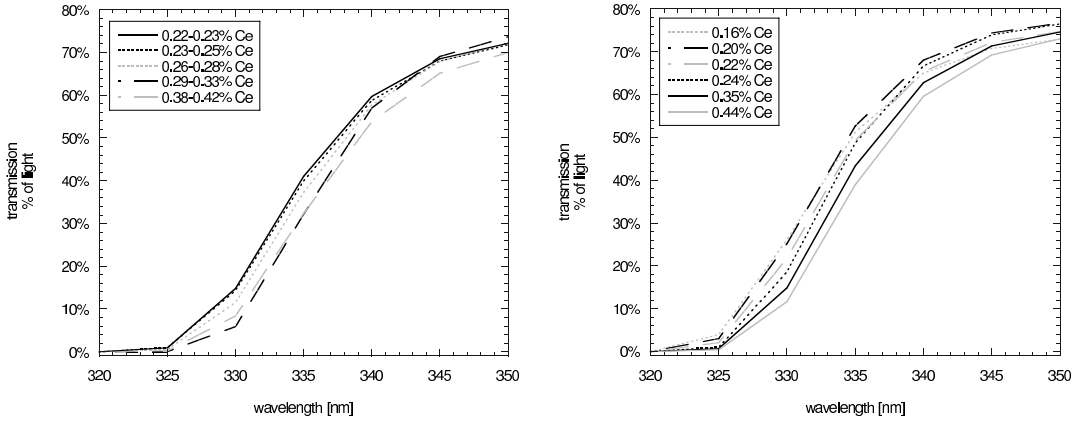

(a) (b)

Figure 4.24: Transmission curves of LuAP (a) and LuYAP (b) crystals with varying cerium content

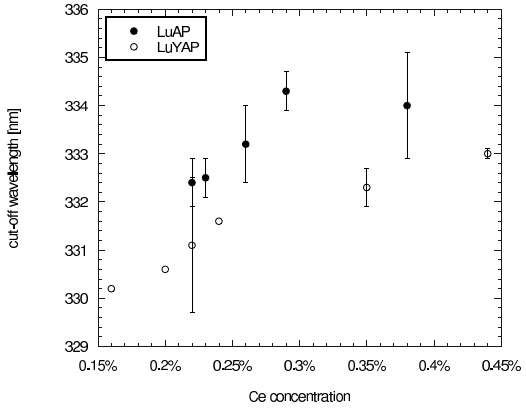

Figure 4.25: Cut-off wavelength as a function of cerium concentration for LuAP and LuYAP crystals

4.7 Depth of interaction resolution

The special scanner geometry for mammography, the small distance between the plates and the proximity to the body lead to considerable parallax errors (dx in Fig. 1.26) because many photons enter the crystal not perpendicularly to its surface but at an obtuse angle passing through the first pixel and producing scintillation in the neighbouring one. The precise measurement of the depth of interaction (DOI) is crucial for the high spatial resolution needed for the imaging of tumours in their early growth stage. In the ClearPEM every crystal is read out at both ends and the light yield difference is used to calculate the DOI. For this method to work the gradient of the light yield difference with distance has to be high enough. To enhance further the difference the crystal can be depolished (see below), an approach used for the ClearPEM. In the current design slightly depolished LYSO pixels of 20 mm length are used. In the specifications for the

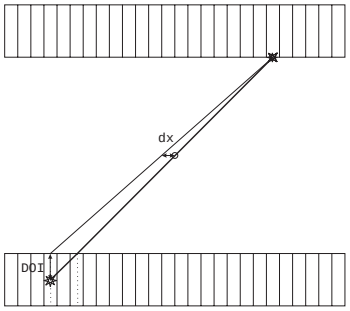

Figure 4.26: Parallax error

ClearPEM the value of the surface roughness of the LYSO pixels is laid down between 100 Å and 300 Å.
To see if it is possible to use LuAP crystals in a future design of the ClearPEM, the DOI resolution measurements are repeated with polished and depolished LuAP crystals. The influence of different reflector materials is also studied.

The transport of light in a perfect crystal takes place without losses by total reflection; absorption or scattering. Assuming also perfect coupling of the crystal to the photomultiplier the difference in photons arriving at both ends is only due to statistical fluctuations of emission angles. In this case the light absorption coefficient μ is zero and the attenuation length λ is ∞ (cf. 2.5.3). In order to obtain information of the DOI with acceptable resolution the attenuation length should be of the order of the length of the crystal. The attenuation length is determined by the physical and optical properties of the scintillator as well as its surface finish, coating and wrapping. Hence it is to change the attenuation length by changing the surface finish. This can be achieved either by choosing different reflective wrappings or by altering the surface itself, e.g. polishing or depolishing.
The idea to enhance the DOI resolution by depolishing one or more surfaces of a crystal is this: in contrast to a polished surface where specular reflection occurs, diffuse reflection takes place on a rough surface. In this way less photons will be reflected from one of the lateral exit surfaces and the difference in light yield between both ends increases. Thus the DOI resolution improves but with a reduction of the total light yield.

4.7.1 Materials

The studied crystals are LuAP and LYSO crystals with dimensions 2x2x20 mm^3. All pixels were produced by Photonics Materials Ltd. (PML), Glasgow, UK. The crystals were delivered polished on all surfaces. After the light yield and DOI measurements, one long surface was depolished, the light yield and DOI measurements redone and another long surface depolished. Two LYSO crystals, which were depolished professionally, are used for comparison. One is depolished according to the ClearPEM specifications, the other has the same surface roughness as the crystal depolished by hand.

The following is a list of the different wrappings used:

- no reflector material;
- Teflon^{TM}, 0.08 mm thickness;
- Tyvek^{TM};
- Mylar^{TM} foil, aluminized with 16 nm Al + 31 nm MgF_2.

All three are commonly used reflector materials with high reflectivity. Out of these, Teflon^{TM} and Tyvek^{TM} are diffuse reflective and aluminized Mylar^{TM} is specular reflective.

4.7.2 Depolishing

The crystal and a dummy crystal of the same dimensions are glued with Cyanolite onto a glass disc and loaded with a pressure of 25 N/cm^2. The holder is moved in a figure of eight over a glass surface wetted with Triefus Surfex diamond emulsion with a mean grain diameter of 8 μm. After each treatment the crystal is left in an Acetone bath for twelve hours to dissolve the glue. The pictures in Fig. 1.27 show the polished (a) and depolished (b) surface of the same LuAP crystal under a light optical microscope with a magnification of 200. The values for the surface roughness (R_a [μm]) are obtained

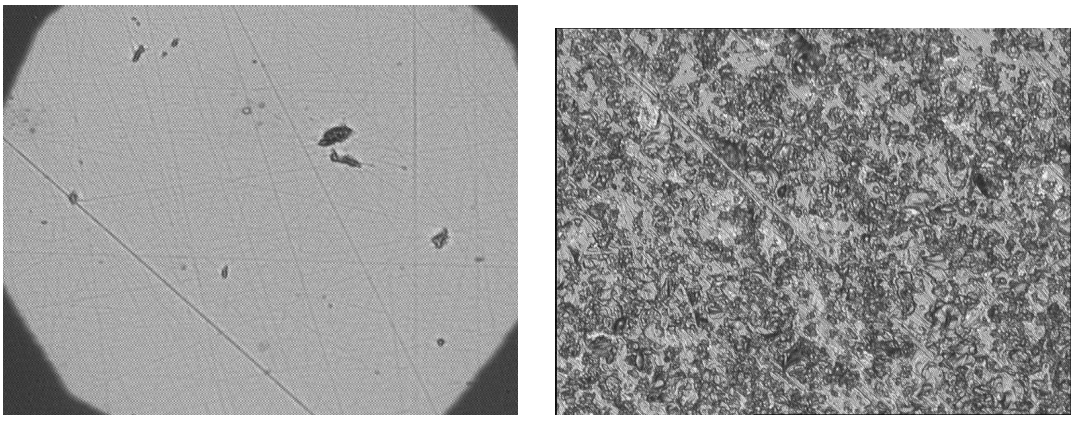

(a) (b)

Figure 4.27: Picture of the polished (a) and depolished (b) surface of a LuAP crystal under a light optical microscope with a magnification of 200

with a surface profile measuring instrument (Surtronic 3+, Rank Taylor Hobson, UK) with a 2% accuracy. An average value is calculated from three successive measurements taken at three different locations on the crystal (Tab. 1.2). It is interesting to note that after the same treatment the surface roughness R_a of the LYSO crystal is twice as big

as the surface roughness of the LuAP. This reflects the different unit cell parameters that are also twice as big for LYSO than for LuAP [10, 11]. The measurement on the polished LuAP crystal was performed by the CERN metrology department.

Table 4.2: Surface roughness values R_a

Crystal	Ra [μm]				
	face 1	face 2	face 3	face 4	
LuAP 1779	0.043	0.042	-	-	polished by producer
	0.16	0.25	0.17	0.17	depolished at CERN
LYSO 1011	0.11	0.14	0.09	0.13	depolished by producer
LYSO 1120	0.5	-	-	-	face 1 depolished by producer
LYSO 7070	-	-	-	-	polished by producer
	0.45	0.42	0.37	0.35	depolished at CERN

4.7.3 Depolishing tests

To test the influence of depolished surfaces on both light yield and depth of interaction resolution one completely polished LuAP and LYSO pixel were chosen. Both quantities are measured for each crystal as they are subsequently depolished.
As a reference and for comparison two professionally depolished LYSO crystals are characterized as well (cp. 1.7.1). The results are summarized in the table on the left in Fig. 1.28 and in Table A.3 in Appendix A. The plot on the right in Fig. 1.28 shows the reduction of the light yield caused by depolishing one, two, three and four long surfaces of the LuAP and LYSO. The light loss due to depolishing just one surface is already

Crystal	number of depolished surfaces	light yield relative to polished crystal
LuAP 1779	0	100%
	1	71%
	2	62%
	3	49%
	4	43%
LYSO 7070	0	100%
	1	89%
	2	70%
	3	39%
	4	38%

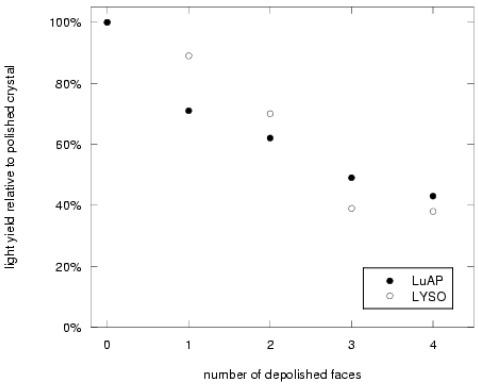

Figure 4.28: Light loss due to depolishing

30% for LuAP and 20% for LYSO and increases to around 60% for both crystals. This is less drastic for LYSO pixels because the initial value in number of photons/MeV is

ususally 2 to 4 times larger than the initial light yield of LuAP. In Fig. 1.29 the position of the photopeak is plotted versus the position of the γ- beam on the crystal (LuAP (a) and LYSO (b)). The graph shows only the peak position recorded with one photomultiplier (PM1). The curves recorded with the second PMT at the opposite end look the same but mirrored. The lines represent the exponential fits. The curves get steeper

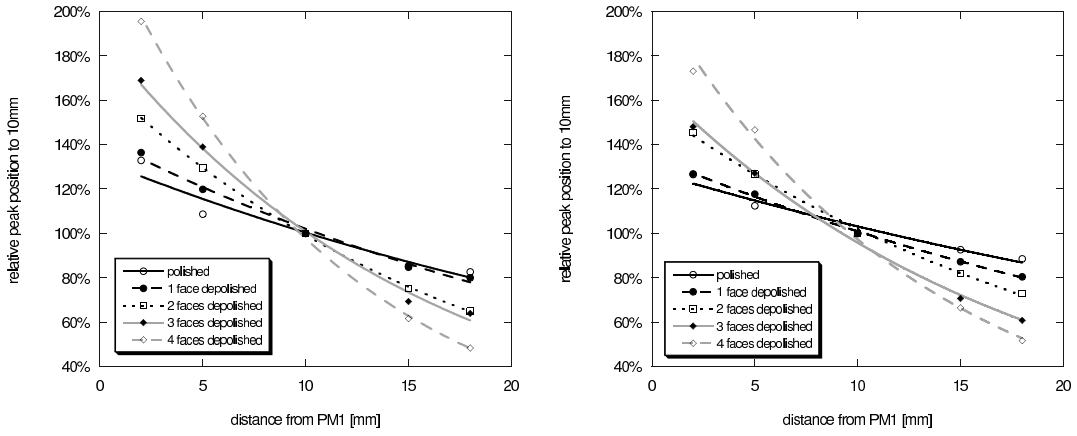

Figure 4.29: Correlation between the position of the photo peak and the excitation point of a LuAP (a) and LYSO (b) crystal with different numbers of depolished surfaces - the lines represent exponential fits

and steeper with the number of depolished faces and accompanying light loss. This fact reappears also in the shortening of the effective attenuation length. In the same manner that both light yield and effective attenuation length decrease the depth of interaction resolution increases (see Fig. 1.30 (a) and (b)). As expected λ_{eff} decreases with a higher

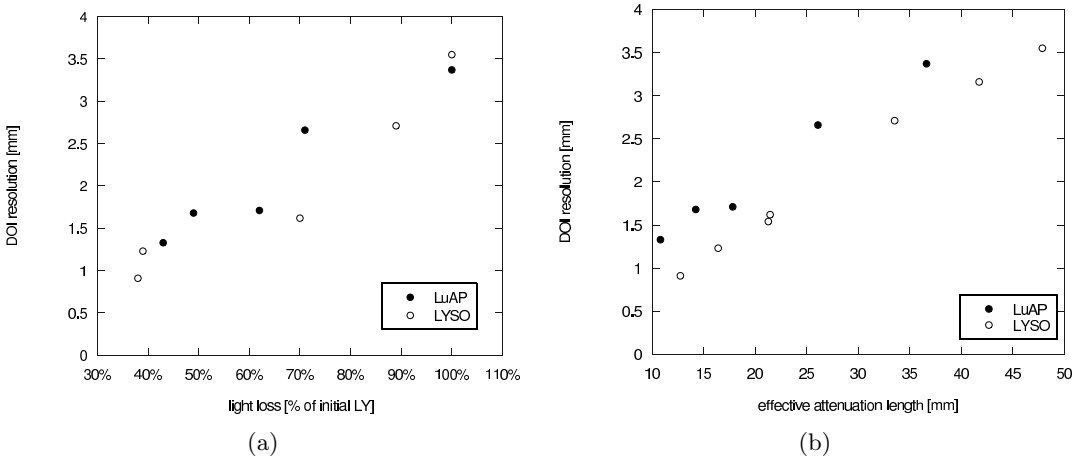

Figure 4.30: Correlation between the DOI resolution and the light loss (a) and between the DOI resolution and the effective attenuation length (b) with different numbers of depolished surfaces

number of depolished crystal faces. The value for λ_{eff} drops from 37 mm to 10 mm.

The depolishing of only two faces is enough to achieve an effective attenuation length in the range of the crystal length. For LYSO crystals the effective attenuation length decreases from 48 mm to 13 mm. In Fig. 1.31 (a) and (b) the asymmetry values are plotted against the position of the interaction in the crystal for LuAP and LYSO. The five measuring points were fitted with a linear curve.
The DOI resolution improves significantly with two depolished crystal faces and then

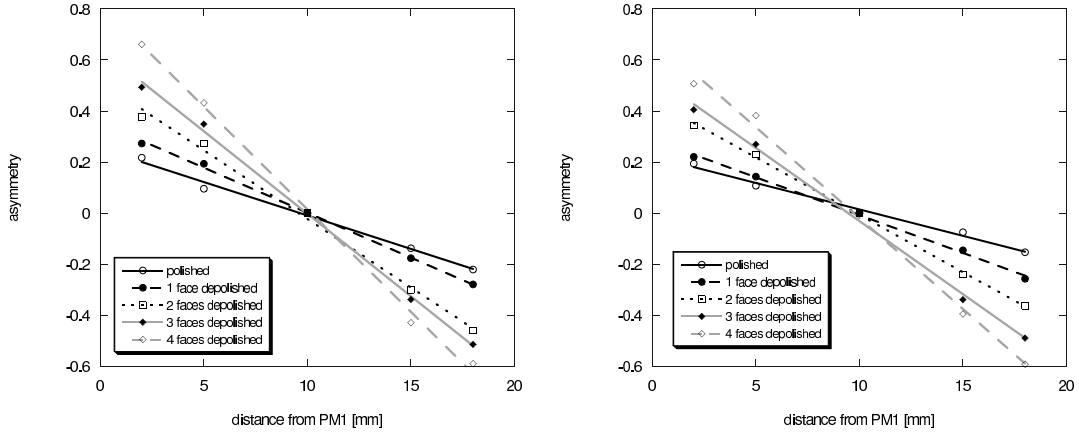

Figure 4.31: Correlation between the asymmetry and the excitation point of a LuAP (a) and LYSO (b) crystal with different numbers of depolished surfaces - the lines represent a linear fit

again with four. The depth of interaction resolution for the LYSO crystal decreases from 3.55 mm (polished), to 1.62 mm (two faces depolished) to around 1 mm (four faces depolished) and for the LuAP crystal decreases from 3.37 mm (polished), to 1.71 mm (two faces depolished) to 1.33 mm (four faces depolished). A LuAP crystal with two depolished faces already meets the DOI resolution requirements of the ClearPEM. The DOI resolution of the ClearPEM reference crystal is found to be 1.54 mm. The values are not corrected for the beam width ($\approx$ 1 mm)
The results on DOI resolution on 2x2x20 mm^3 LYSO crystals published by Santos et al [12] show a somewhat better resolution for the polished pixels. Their values for slightly polished and very rough crystal surfaces are in the same range of between 1.8 mm to 1.2 mm.
Fig. 1.32(a) for LuAP 1779 and (b) for LYSO 7070 show the depth of interaction resolution at the individual points along the crystal. The uniformity of the DOI resolution is very good for the polished LuAP but starts to deviate from a mean value more largely after the depolishing. This effect is worse for LuAP than LYSO. The most probable cause is the manual polishing, which produces an uneven surface finish. The LuAP proved to be more brittle than the LYSO crystal and several tiny bits broke off at the corners.

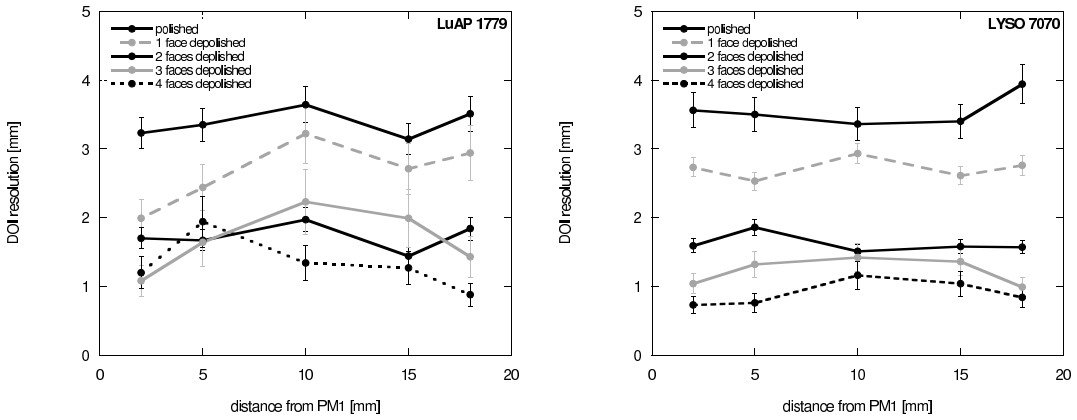

(a) (b)

Figure 4.32: Depth of interaction resolution of LuAP (a) LYSO (b) with different number of depolished surfaces

4.7.4 Reflector tests

As stated above the depth of interaction resolution depends on the attenuation length, which in turn depends on the surface finish. In a first trial different reflector materials are compared to the result obtained with a naked polished LuAP crystal. Fig 1.33 shows a comparison of the DOI resolution of a polished LuAP crystal to polished LuAP crystals wrapped in Teflon^{TM}, Tyvek^{TM} or Mylar^{TM}. Each point represents an average value of the DOI resolution measured at five different points along the crystal axis. As can be seen the reflector material has little influence on the attenuation length and the DOI resolution. All values lie around 5 mm and are equal within errors.

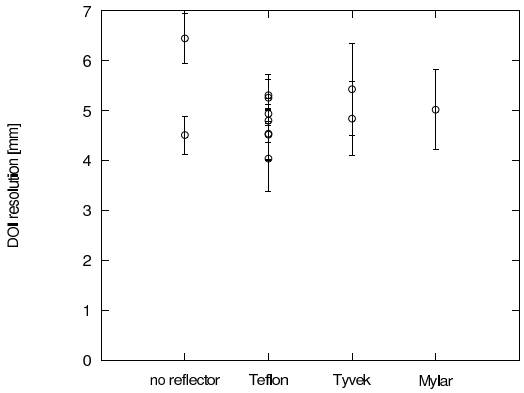

Figure 4.33: Comparison of the DOI resolution with different reflector materials

4.8 Conclusions

Data on light output, energy resolution and the non-proportionality of the scintillation response, as well as on decay time, transmission and the influence of the cerium concentration have been presented for LuAP and LuYAP crystals from three different producers.
The properties of the LuAP PML crystals were found to be very homogeneous inside the batch and no double peaks were observed in the energy spectra. Due to that, they also have higher energy resolution. The light yield values for all LuAP crystals do not differ significantly from one producer to the other, but LuAP PML crystals display more absorption. Regarding the decay time constants the difference between PML, IPR and BTCP lies in the longer slow component for PML.
Comparing the decay times of LuAP to LuYAP one finds a slower decay time for the fast and the slow component for LuYAP pixels.
PML and BTCP crystals show a higher absorption than IPR, confirmed by the ratio of the light yield and the transmission measurements. The calculated degrees of non-proportionality reveal that the light output of LuAP and LuYAP crystals is less influenced by the energy than the light output of LYSO crystals.
The cerium concentration has an influence on all properties of the crystal. An increase in the cerium concentration leads to a higher light output and faster time constants, at least until a value of 0.44% of cerium to which point the measurements are performed in this thesis.
It could be demonstrated that a LuAP crystal with two depolished faces already fulfils the requirements in DOI resolution for the ClearPEM. With increasing number of depolished surfaces of a crystal pixel, a significantly augmentation in the resolution of the depth of interaction can be obtained. However this gain in resolution goes hand in hand with a loss of photons.

In consideration of these results, LuAP crystals produced by IPR show the best overall performance. Their light yield is comparable to the light yield of LuAP crystals from PML and of LuYAP crystals, but LuAP PML exhibit the least absorption of scintillation light. Furthermore LuAP crystals have a slightly "shorter" fast component than LuYAP crystals with the added advantage of emitting more photons in the fast component. The relative light output of LuAP is less dependent on the energy than the relative light output of LYSO; the depth of interaction resolution of LuAP crystals is slightly better than of LYSO crystals and the scintillation in LuAP crystals is twice as fast as for LYSO.
LYSO crystals have a higher light yield than LuAP crystals but through the addition of more cerium atoms to LuAP crystals their light yield can be increased.

Unfortunately LuAP crystals are are not easily available in large quantities at a low price, but the price for LuAP crystals could drop if the demand increases (this has already happened for L(Y)SO).

Bibliography

[1] J.Trummer, E.Auffray, P.Lecoq, A.Petrosyan, P.Sempere-Roldan, Comparison of LuAP and LuYAP crystal properties from statistically significant batches produced with two different growth methods. Nucl Instr and Meth A 551 (2005) 339.

[2] P.Lecoq, M.Korzhik, New Inorganic Scintillation Materials Development for Medical Imaging. 2001 IEEE NSS-MIC Conference Record, San Diego, USA.

[3] P.Wu, A.D.Pelton, Coupled thermodynamic-phase diagram assessment of the rare earth oxide-aluminium oxide binary systems. J Alloys Compd 179 (1992) 259.

[4] M.Balcerzyk, M.Moszynski, Z.Galazka, M.Kapusta,A.Syntfeld, J.L.Lefaucheur, Perspectives for high resolution and high light output LuAP:Ce crystals. 2004 IEEE NSS-MIC Conference Record, 16.-22.Oct.2004, Ergife Palace Hotel, Rome, Italy.

[5] P.Dorenbos, J.T.M.de Haas, C.W.E.van Eijk, Non-Proportionality in the Scintillation Response and the Energy Resolution Obtainable with Scintillation Crystals. IEEE Trans Nucl Sci 42 (1995) 2190.

[6] P.Dorenbos, Light output and energy resolution of Ce^{3+}-doped scintillators. Nucl Instr and Meth A 486 (2002) 208.

[7] C.Kuntner, E.Auffray, P.Lecoq, C.Pizzolotto, M.Schneegans, Intrinsic energy resolution and light output of the $Lu_{0.7}Y_{0.3}$AP:Ce scintillator. Nucl Instr and Meth A 493 (2002) 131.

[8] C.Dujardin, C.Pedrini, W.Blanc, J.C.Gacon, J.C.van't Spijker, O.W.V.Frijns, C.W.E.van Eijk, P.Dorenbos, R.Chen, A.Fremout, F.Tallouf, S.Tavernier, P.Bruyndonckx, A.Petrosyan, Optical and scintillation properties of large $LuAlO_3$:Ce^{3+} crystals. J Phys Condens Matter 10 (1998) 3061.

[9] A.Petrosyan, G.O.Shirinyan, K.L.Ovanesyan, C.Pedrini, C.Dujardin, N.Garnier, S.Sowinski, P.Lecoq, A.Belsky, Potential of existing growth methods of LuAP and related scintillators. Nucl Instr and Meth A 486 (2002) 74.

[10] A.G.Petrosyan, G.O.Shirinyan, K.L.Ovanesyan, C.Pedrini, C.Dujardin, Bridgman single crystal growth of Ce-doped $(Lu_{1-x}Y_x)$AlO3, Journal of Crystal Growth 198/199 (1999) 492.

[11] C.L.Melcher, J.S.Schweitzer, Cerium-doped Lutetium Oxyorthosilicate: A Fast, Efficient New Scintillator, IEEE Trans Nucl Sci 39 (1992) 502.

[12] M.A.Abreu, J.D.Aguiar, F.G.Almeida, P.Almeida, P.Bento, B.Carrico, M.Ferreira, N.C.Ferreira, F.Goncalves, C.Leong, F.Lopes, P.Lousa, M.V.Martins, N.Matela, P.R.Mendes, R.Moura, J.Nobre, N.Oliveira, C.Ortigao, L.Peralta, R.Pereira, J.Rego, R.Ribeiro, P.Rodrigues, J.Sampaio, A.I.Santos, L.Silva, J.C.Silva, P.Sousa, I.C.Teixeira, J.P.Teixeira, A.Trinidade, J.Varela, Design and evaluation of the Clear-PEM scanner for positron emission mammography. IEEE Trans. Nucl. Sci. 53-1 (2006) 71.

Chapter 5

Monte Carlo simulations

Simulations are a necessary tool to understand detector behaviour and predict performance characteristics, like sensitivity, count rates and background noise. Moreover simulations aid understanding of the effects of changes to the detector design such as additional material in the detector area.
This chapter touches briefly upon the features of the simulation software and some detector properties which are studied in the simulation.

5.1 Simulation software

GATE [1] (Geant4 Application for Tomographic Emission) is a general purpose simulation platform for positron emission tomography (PET) and single photon emission computed tomography (SPECT) applications. It is built as an upper layer for the Geant4 [2] simulation toolkit. It combines the well validated physics model, the geometry description and the visualization and 3D rendering tools from Geant4 with specific software dedicated to PET and SPECT. GATE also includes the modelling of time dependent processes. The code is written in C++, but the full set-up and control of the simulation is performed using interactive scripting or execution of macros. GATE was developed by the OpenGATE Collaboration, which includes 21 laboratories in 9 countries in Europe, Asia and the US. The first public release of the code was in May 2004.

Each simulation is organized in the same general architecture:

1 Verbosity and visualization

2 Geometry

3 Physics

Initialization

4 Digitizer

5 Sources

6 Output

7 Data acquisition.

In the first step the user has to decide which software to use for visualization and how much information is displayed during a simulation - the verbosity.

In principle any geometry can be built in GATE, but there are also five predefined scanner geometries available: scanner, cylindricalPET, CPET, SPECThead and ecat. Each system has its own geometrical constraints and data output options. In this step the different shapes, dimensions, materials and movements of the parts of the detector are specified. If a phantom is used, its type, position, material and movement is defined. Finally the sensitive detectors (SD) have to be assigned to the different components. Only in SD components information about particle interaction is stored. In a volume allocated with a phantomSD only Compton and Rayleigh interactions are counted whereas in a volume with crystalSD more information is recorded: the type of interaction inside the volume, energy deposition, position of interaction, origin of particle, ...

After the geometry selection the types of particles which will be produced and transported in the simulation have to be set. Physics processes which will be taken into account have to be enabled or disabled for every particle type.

With this information, the simulation can be initialized, the geometry is then built and all the cross section tables for all the particle interactions in the defined materials are loaded.

The digitizer is a module to reproduce the behaviour of the components, electronics and readout chain. The digitizer options include readout depth, energy and time blurring, dead time, energy thresholds, coincidence time window, noise, ...

Sources are determined by the type of particle, the shape and the initial activity. For the most commonly used positron emitters in PET (F-18, O-15, C-11) a more detailed description is available, including half-life and energy spectrum of the e_+. It is possible to add a voxelized source. The image data has is converted to an activity via a translation table. If several sources are implemented in the simulation each one is identified by its own source ID number.

The user can choose between six different file formats: ASCII, ROOT, Interfile, sinogram, ECAT7 and LMF. For every photon that interacts with the detector information on its position, energy, undergone interactions, ... are stored. For a full list and description refer to Table B.1 in Appendix B.

In a final step the simulation time is set and the acquisition started.

5.1.1 Body phantom

In more realistic simulations a voxelized phantom is used to generate the background activity originating in the body and different organs. The phantom is split in two, the breast and the torso with the organs. The breast is simulated in a hanging uncompressed state. Fig. 5.1 gives some typical values for breast width and thickness. The width is the dimension of the breast in the transverse plane and the thickness is the dimension in the coronal plane. Average values are chosen for the breast phantom used in the GATE simulations. The breast phantom is fragmented into 1621 cubic voxels with a volume of 0.42 ml each. (Fig. 5.2). The NURBS[1]-based cardiac torso (NCAT) phantom [3] is

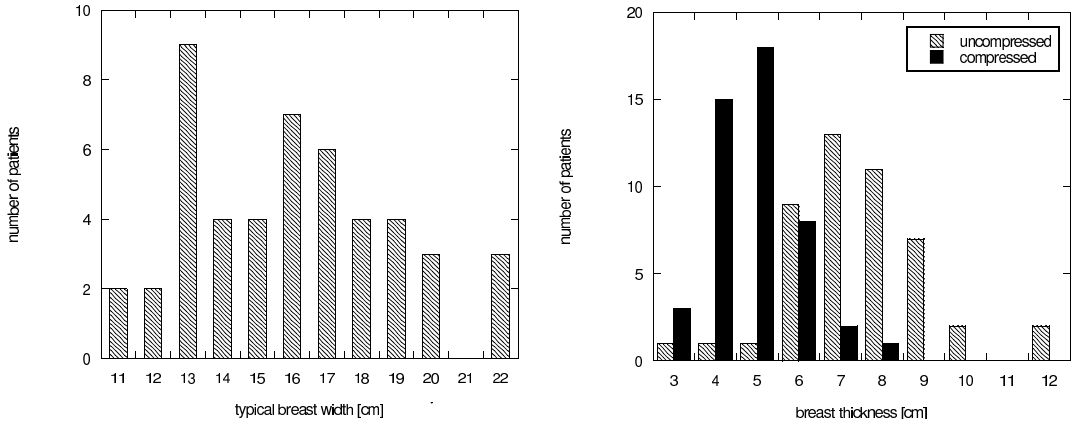

(a) (b)

Figure 5.1: Typical values for breast width (a) and thickness (b) [4]

Dimensions	
width [cm]	13.5
thickness [cm]	9.0
depth [cm]	10.5
voxel size [mm^3]	7.5 x 7.5 x 7.5
number of voxels	1621

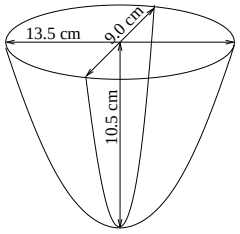

Figure 5.2: Dimensions for the breast model used

implemented into the GATE simulation to represent the torso together with the organs. The model data is based on CT scans from the Visible Human project.
The programme generates an ASCII integer file from a parameter file. This file contains the dimension of the body, the voxel size and the selection of organs to be taken into account. Fig. 5.3 shows the graphically processed raw data. The activity in each voxel

[1] non-uniform rational B-splines

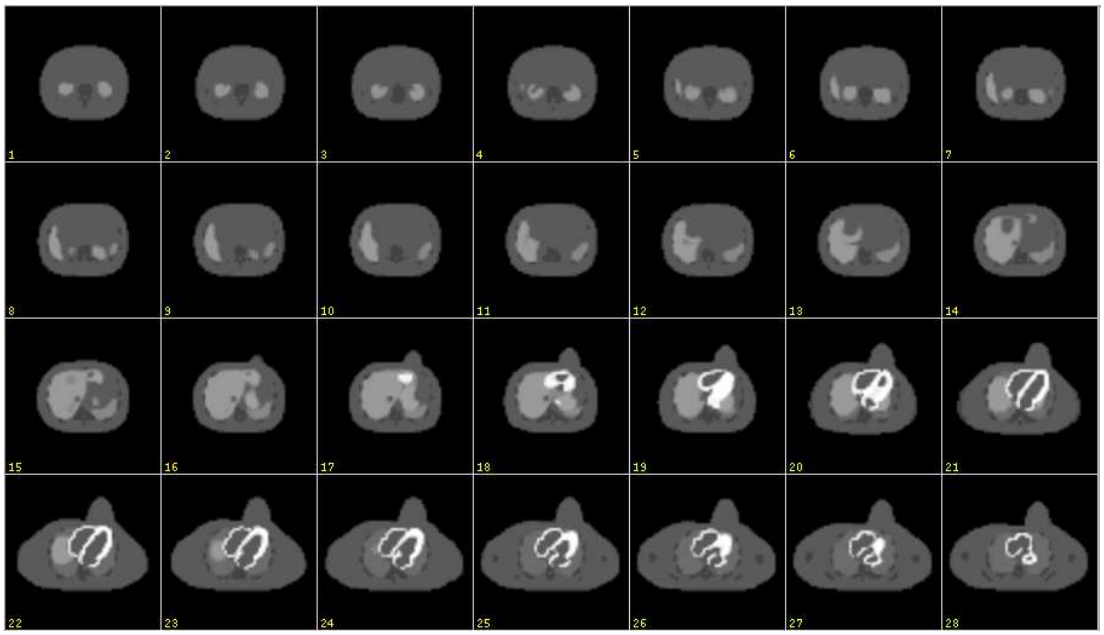

Figure 5.3: Data generated from the NCAT phantom model

is calculated using the standardized uptake values (SUV).

$$SUV = \frac{tissue\ activity[\mu Ci/ml]}{\frac{injected\ activity[\mu Ci]}{body\ weight[g]}} \tag{5.1}$$

The SUV is commonly used in FDG PET imaging [5]. In this study an average weight of 70 kg for a woman is chosen.

Fig. 5.4 shows the phantom model and the activity values of FDG for each organ and the background used in the GATE simulations. The values are taken from Trindade et al [6], members of the Crystal Clear Collaboration. They also provided simulation data for the ClearPEM utilizing specially developed Geant4 modules. The tumour is situated in the anterior half of the breast and has a volume of 10 ml. It is simulated with a lesion to background ratio of 1:10. This is an optimistic assumption which is nevertheless made to assure a tumour signal that clearly lies above the noise. Real lesion to background ratios can vary significantly between 1:2 and 1:20 depending on the type and diameter of the lesion and its location within the body [7]. From the initial injected activity, 0.37% of the activity is absorbed in normal breast tissue. In total 13.4% is taken up by the torso phantom including the organs.

Organ	Activity [kBq/ml]	Organ to background ratio
body	2.1	1.00
heart	21.9	10.38
liver	9.1	4.31
spleen	6.2	2.94
lung	2.0	0.95
kidney	8.6	4.08
stomach wall	9.8	4.64
tumour	21	10.00

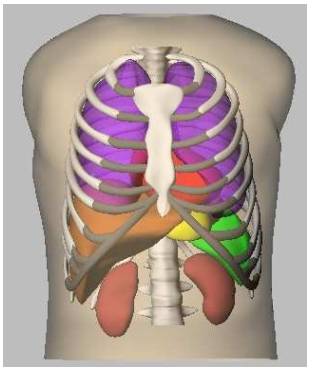

Figure 5.4: Activity in each organ for 370 MBq injected FDG

5.2 Simulation

If it is not stated specifically in this text the ClearPEM was modelled in the simulation using the geometry and materials described in the sections below.

5.2.1 Scanner geometry and electronics chain

To simplify the simulation not all mechanical parts are included although the dimensions and the spaces and the gaps created by these components are meticulously preserved within the simulation as air. The crystals are LYSO pixels with a dimension of 2x2x20 mm^3 with an energy blurring of 13% to 18% at 511 keV.
Each matrix is read out by a simple module which adds temporal blurring and dead time. The initial estimation of 1 ns (FWHM) time resolution of the scanner had to be corrected upwards. First measurements on the prototype plates at the Laboratorio de Instrumentacao e Fisica Experimental de Particulas (LIP) in Lisbon, Portugal suggest that the actual value is closer to 2 ns to 3 ns (FWHM). The length of the coincidence window is 4 ns as found in the specifications.

5.2.2 Materials

The materials used in the simulation are air, plastic (PMMA[2]), $BaSO_4$, which is the reflector material that is cast around the 32 LYSO crystals to form a matrix. The different body parts are all represented by one tissue material. The definitions from the GATE material database are reproduced in Table 5.1.

[2]polymethylmethacrylate

Table 5.1: Composition of the materials used in the simulation

material	density [g/cm^3]	element	mass fraction or number of atoms
Air	$1.29{\cdot}10^{-3}$	Nitrogen	0.755268
		Oxygen	0.231781
		Argon	0.012827
		Carbon	0.000123
Plastic	1.18	Carbon	5
		Hydrogen	8
		Oxygen	2
$BaSO_4$	4.502	Barium	1
		Sulphur	1
		Oxygen	4
LYSO	7.1	Lutetium	0.73972
		Yttrium	0.01978
		Silicon	0.06250
		Oxygen	0.17800
Tissue	1.020	Oxygen	0.5270
		Carbon	0.3320
		Hydrogen	0.1060
		Nitrogen	0.0300
		Sulphur	0.0020
		Sodium	0.0010
		Phosphor	0.0010
		Chlorine	0.0010

5.3 Detector parameters

Some parameters to define a detector and to compare its performance with other systems are the sensitivity or true coincidence count (TCC) rate, the scatter fraction (SF), the random fraction (RF) and the noise equivalent count rate (NECR).
The parameters are defined as:

$$sensitivity = \frac{T}{number\ of\ \beta^+ - decays} \tag{5.2}$$

$$SF = \frac{S}{T+S} \tag{5.3}$$

$$RF = \frac{R}{T+S+R} \tag{5.4}$$

where T is the true coincidence rate, S the scattered coincidence rate and R the random coincidence rate. The relation between the activity, in fact the singles rate s per detector plate, and the true coincidences is linear. The random coincidence rate increases

quadratically with the singles rate (eq. 5.5).

$$R = 2\Delta t s^2 \tag{5.5}$$

$2\Delta t$ is the length of the coincidence time window.

5.3.1 Noise equivalent count rate

Although the true coincidence count rate as a function of activity (sensitivity) is a good parameter to characterize any detector, there is no direct link between TCC rates and image quality. The noise equivalent count rate incorporates the image noise and connects signal-to-noise ratios to scattered and random coincidences.
The noise equivalent count rate is defined as follows:

$$NECR = \frac{T^2}{T + S + 2kR} \tag{5.6}$$

where T is the true coincidence rate, S the scattered and R the random coincidence rate. k is a geometrical parameter, giving the ratio of the diameter of the phantom to the diameter of the scanner. The NECR depends strongly on the event rate and the dead time of the detector.

5.3.2 Dead time behaviour

Dead time is the minimum time two events must be temporally separated in order to be recorded as two events. The amount of time is influenced by the detector itself and by associated electronics and data acquisition. True events might be lost because they occur too quickly one after the other. These losses can become quite serious with high count rates.
Two models are commonly used to describe dead time behaviour: paralysable and non-paralysable. In both models each event produces a dead time of a certain constant interval. Any event that occurs during the dead time is lost. In the non-paralysable model these events have no effect on the detector. In the paralysable model each event that hit the detector in the dead period extends the dead time by another interval. Thus more events are registered assuming a non-paralysable dead time especially at high count rates and long dead time periods. In a plot of the observed rate versus the true rate a non-paralysable system will approach an asymptotic value (the inverse of the dead time) whereas for a paralysable system the curve has a maximum [8].

Bibliography

[1] D.Strul, G.Santin, D.Lazaro, V.Breton, C.Morel, GATE (Geant4 Application for Tomographic Emission): a PET/SPECT general-purpose simulation platform. Nuclear Physics B (Proc. Suppl.) 125 (2003) 75.

[2] S.Agostinelli et al, GEANT4 - a simulation toolkit. Nucl Instr and Meth A 506 (2003) 250.

[3] W.P.Segars, Development of a new dynamic NURBS-based cardiac-torso (NCAT) phantom., PhD dissertation, The University of North Carolina, May 2001.

[4] R.Pani, A.Soluri, R.Scafe, R.Pellegrini, G.De Vincentis, M.N.Cinti, M.Betti, R.Inches, F.Garibaldi, F.Cusanno, M.Gambaccini, A.Fantini, A.Taibi, A.Olivo, S.Pani, L.Rigon, D.Bollini, N.Lanconelli, A.Del Guerra, Feasibility study for SPECT Mammography based on compact imagers rotating around breast vertical axis. 1st topical symposium on Functional Breast Imaging with Advanced Detectors, Istituto Superiore di Sanita - Viale Regina Elena 299, Rome April 18-21, 2001.

[5] S.C.Huang, Anatomy of SUV. Nuclear Medicine & Biology 27 (2000) 643.

[6] A.Trindade et al, Breast cancer imaging studies by Monte Carlo simulation with Clear-PEM, 2005 IEEE-NSS Conference Record (2005) 2103-2107

[7] M.B.Imran, K.Kubota, S.Yamada, H.Fukuda, K.Yamada, T.Fujiwara, M.Itoh, Lesion-to-Background Ratio in Nonattenuation-Corrected Whole-Body FDG PET Images. J Nucl Med 39 (1998) 1219.

[8] G.F.Knoll, Radiation detection and measurement - 3rd ed. New York, NY: Wiley, 2000.

Chapter 6

Simulation results

In this chapter the results of the GATE simulations are presented. The ClearPEM is simulated as specified on page 25. First the sensitivity of the ClearPEM is presented for different geometries. Then the influence of immobilization plates on the detector and a new approach to reduce the random background is shown, a veto counter. Several configurations of the veto counter are compared with regard to their effectiveness of background reduction. Finally, noise equivalent count rates (NECR) are calculated from the simulated rates.

6.1 Sensitivity

The sensitivity is an important characteristic of any detector. The sensitivity of a PET is defined as the ratio of the number of detected true coincidences to the number of β^+-decays. It depends on the position of the source in the detector, the solid angle covered by the detector and the area of dead space in the detector. In medical imaging the sensitivity has a direct influence on the length of the examination and thus the radiation exposure and cost.

The new CCC project that integrates an ultrasound probe into the ClearPEM make changes to the geometry of the ClearPEM necessary to accommodate first, the probe itself and second a breast stabilization device, e.g. immobilization plates (IP). Stabilization of the breast is required for the ultrasound examination and image fusion with the result from the PET.
Fig. 6.1 (a) shows a schematic drawing of the ClearPEM with IP (a is the height of the IP, b is the thickness of the IP, d1 is the distance between the IP and d2 is the distance between the detector plates). The use of immobilization plates requires a larger distance between the detectors for rotary motion. The additional widening depends also on the size of the breast, the degree of compression and the dimensions of the immobilization plates. As an example, IPs that are 5 mm thick, 10 cm wide and 10 cm apart require

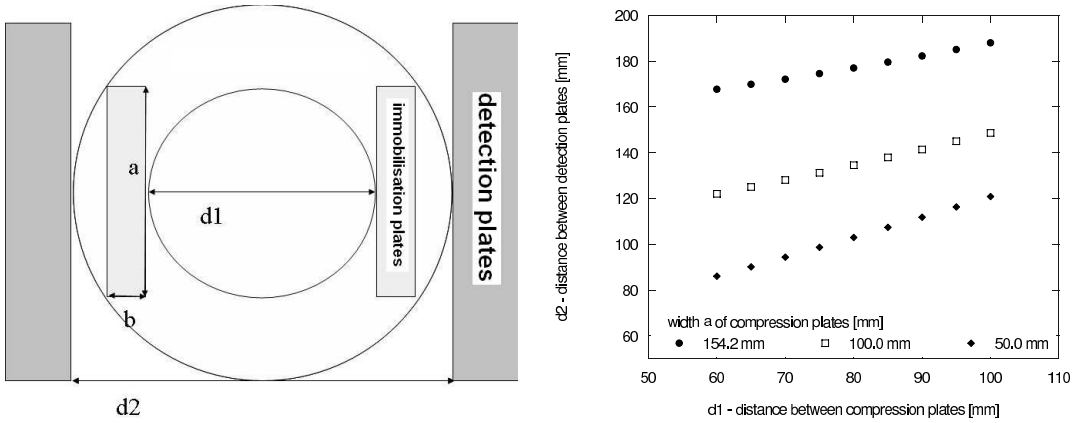

(a) (b)

Figure 6.1: Schematic drawing of the ClearPEM detector with immobilization plates (a) and a comparison of the distance between the immobilization plates and the necessary distance between the detection plates for rotary motion (b)

a distance between the detectors of almost 15 cm. Fig. 6.1 (b) illustrates the distances that are necessary between the detection plates when using compression plates. In all three cases the IP are 5 mm thick but vary between 50 mm and 154.4 mm in width. 154.4 mm is the width of the detection plates.

The first simulations are of the ClearPEM alone, increasing only the distance between the detection plates and the source in the centre of field of view. The simulations of the axial sensitivity of the machine are performed with a 1 MBq Fluorine-18 source which is displaced axially from the centre of field of view (FOV). The ratio between detected true coincidences and generated decay events is calculated.
As expected a loss of sensitivity is observed which decreases quadratically with distance between the detector plates as an effect of the reduction of the solid angle (Fig. 6.2 (a)). The sensitivity value at the centre of FOV drops from 7.55% to 4.71% when increasing the space between the detectors d2 from 10 cm to 15 cm. The change in axial sensitivity is shown in Fig. 6.2 (b) for these two different detector spacings. These results are consistent with independent simulations described in [1] for the ClearPEM scanner, which indicate a 6.6% system sensitivity for a 10 cm detector spacing and a 350-700 keV energy window. The next plot (Fig. 6.3) shows the change of the sensitivity for different angles between the immobilization and the detector plates. Two things become clear. The extra material of the IPs in the path of the photons does almost not reduce the sensitivity. The sensitivity decreases from a maximum of 4.71% to 4.39%. The highest value is of course reached when the IPs are perpendicular to the detection plates.

Another important feature concerns the percentage increase of random coincidences with larger distance between the detector heads. This is studied by adding a uniform torso background was added to the simulation. The position of the annihilation in the torso of the detected random coincidences and their detection position on the plates are

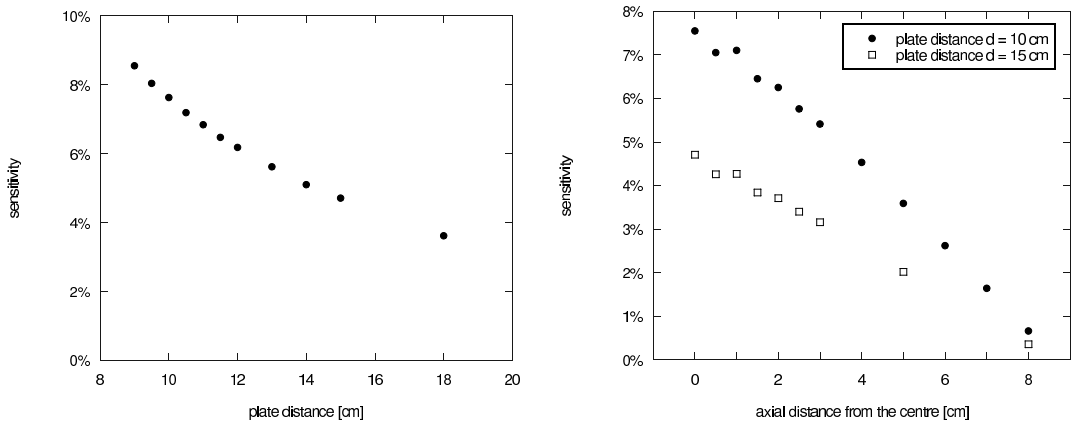

(a) (b)

Figure 6.2: Sensitivity in the centre of FOV as a function of distance between the detection plates (a) and sensitivity as a function of axial displacement from the centre of FOV for two fixed distance between the detection plates (b)

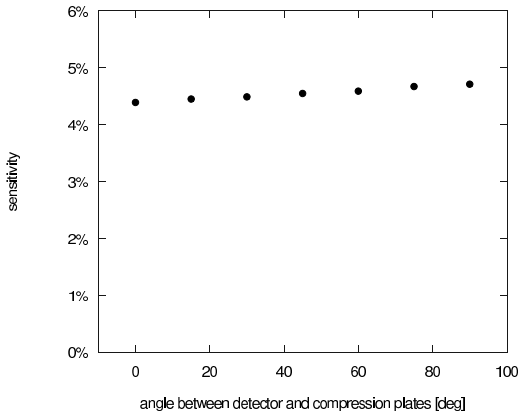

Figure 6.3: Sensitivity at the centre of FOV for different rotating angles between immobilization and detection plates

shown in Fig. 6.4 (a). In Fig. 6.4 (b) the percentage of the random coincidences is plotted versus the plate distance. Random coincidences do not constitute the background alone. True coincidences that originate anywhere else but the cancer contribute as well. The values represented by the squares also include the true coincidences originating in the body. True coincidences from the body are likely to happen in the area very close to the scanner. Immobilization plates introduce a break in symmetry for rotation which requires a larger distance between the detector heads. This reduces the sensitivity and increases the contribution from the body to the random and background rate (includes true coincidences which originated from the body). A symmetric shape might therefore be a better choice for an immobilization system, e.g. a cylinder or cup. On the other hand the additional material in the detector area has a marginal influence on the sensitivity.

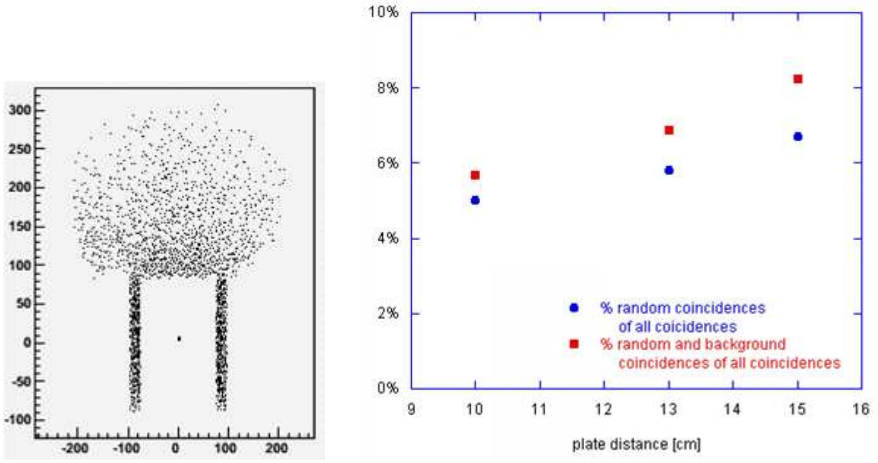

(a) (b)

Figure 6.4: Points of origins and detection of random coincidences (a) and random fraction as a function of plate distance (b)

6.2 Veto counter

The most commonly used radio pharmaceutical in PET is FDG, a glucose molecule with a F-18 atom as a ligand. Glucose is used in all cells to produce energy. Cells with a high energy uptake such as fast growing or very active cells (tumour cells but also heart or brain cells) will accumulate more FDG. The activity distribution of the phantom in all three planes are shown in Fig. 6.5 (a) to (c). The hot spots can be clearly identified as the heart and the liver. (Note that only the decay events that produced a

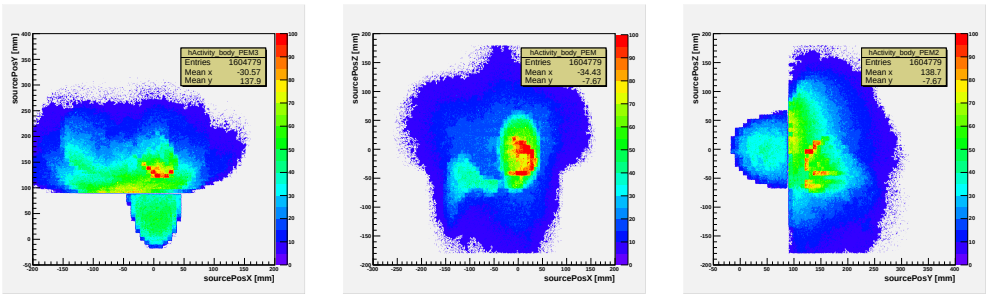

(a) (b) (c)

Figure 6.5: Projections of the FDG activity in the body to the xy- (a), xz- (b) and yz- (c) plane

detected single photon are represented in the pictures.)
To demonstrate the huge amount of photons constituting the background, a profile of the source is shown in Fig. 6.6, which shows the number of detected single photons in the PEM, according to their position of emission. The tiny peak at a distance of around 10 mm is the contribution from the cancer. Profiles along the detection plates in z-

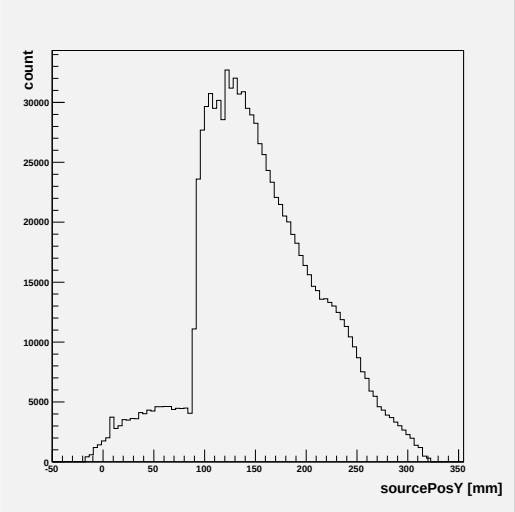

Figure 6.6: Activity

direction show the high amount of true and random coincidences being detected close to the chest (Fig. 6.7). The effect of the random coincidences to the PEM images is also

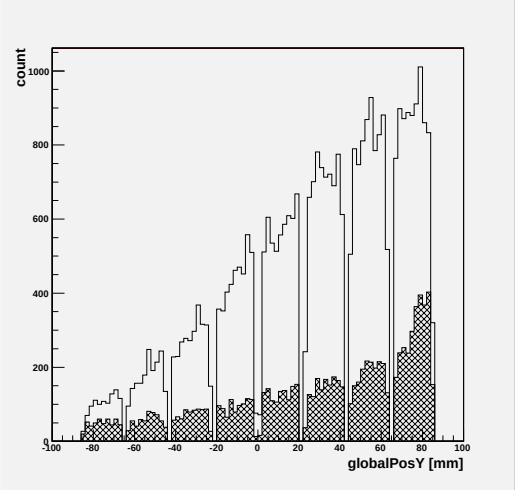

Figure 6.7: Distribution along the plate of true (plain columns) and random (quadrilled columns) coincidences

demonstrated in Fig 6.8 taken from [2]. It shows the intensity profile of a reconstructed image from simulated data of a breast PEM scan. A 5 mm lesion was simulated at a distance of 6 cm of the centre of field of view in the direction towards the breast. Adding the torso background reduces the image contrast by 18%. The close presence of the heart and other organs to the breast leads to a high background noise level in the scanner. This makes it difficult to find small tumours especially those close to the chest.

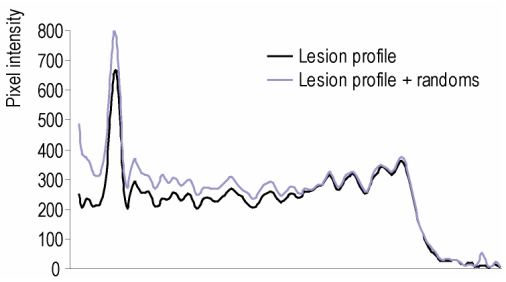

Figure 6.8: Comparison of the image contrast of a reconstructed breast scan with and without torso background

A veto counter could reduce the background.

The working principle of the veto counter is to reduce the background noise by reducing the random coincidences in the final data before reconstruction. The idea is to look for three photons arriving at the detector in a certain time window, so-called triple coincidences. The sorting algorithm opens an individual time window for every detected single event and calculates the time difference between the arrival of the next photons. If the time difference between the first and the second photon as well as the time difference between the second and third photon is less or equal than the chosen coincidence time window (4 ns in this study) a triple coincidence is recorded. Triple coincidences can happen between all possible combinations of the plates: three photons in one PEM plate, three photons in the veto counter, two photons in the veto counter and the third in the PEM plate, etc. ... Whenever a triple coincidence occurs between both plates of the PEM detector and the veto counter the event is rejected. Among the rejected triples, the coincidence in the PEM plates can be a true or random coincidence (Fig. 6.9).

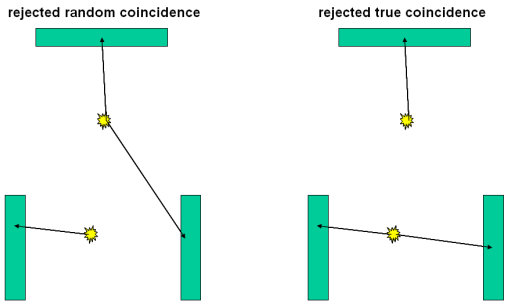

Figure 6.9: Rejected random and true coincidences

The proposed design for a veto counter is a third detection unit behind or around the patient's chest. The model and the dimensions used for the simulation are shown in Fig. 6.10. The figure shows the configuration for the left breast. The geometry of the veto counter in the simulation consists of three parallel rings of twelve plates each. The gaps between each plate in a ring are 5.5 cm and the distance between the rings in z-direction

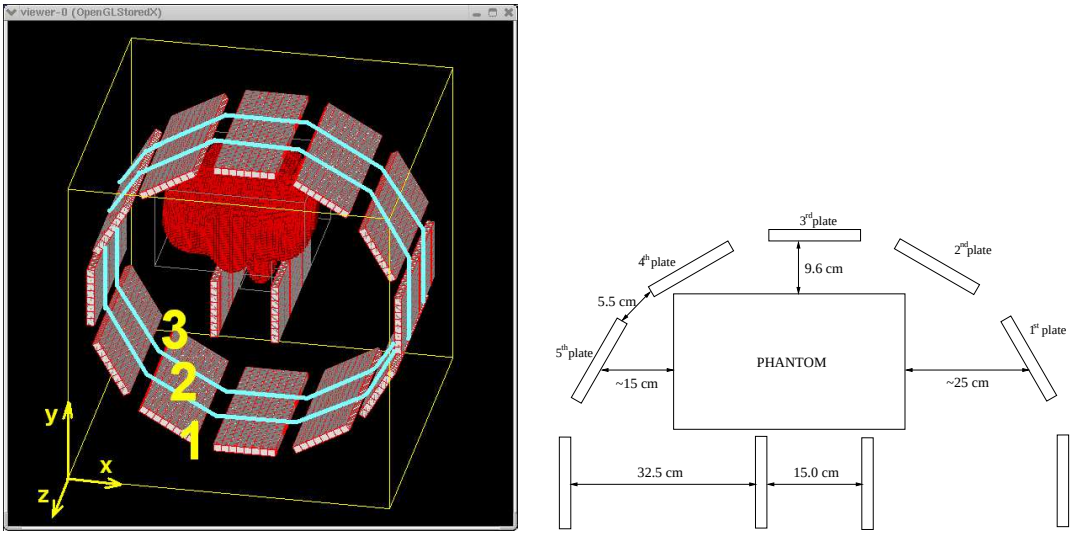

(a) (b)

Figure 6.10: 3-D views of the simulation model with three rings (a) and schematic (b) for the left breast

is 2 mm. In the simulation the plates for the veto counter have the same dimension and configuration as the two PEM plates. This was a necessary compromise because of constraints imposed by the simulation software. The PEM plates have considerable dead space because of the APDs and the small crystals. In addition, photons get lost in the gaps between the plates and the rings. This leads to only 66% coverage of the upper body.
For the analysis the data file of all single photons detected anywhere in the detector is sorted into:

- single photons detected in the PEM plates
- single photons detected in the PEM plates and the plates of the veto counter according to the chosen configuration of the veto counter
- coincidences between the PEM plates - "double" coincidences
- triple coincidences between both PEM plates and the veto counter

All coincidences (double and triple) are further separated according to their origin (cancer, breast or body), their location of detection and whether the two photons in coincidence in the PEM plates are a true or a random coincidence. To evaluate the benefit of the veto counter the important parameters are:

- the ratio of triple coincidences to "double" coincidences in the PEM plates
- the ratio of rejected random coincidences to random "double" coincidences in the PEM plates

- the ratio of rejected true coincidences to true "double" coincidences in the PEM plates
- location of the rejected events on the PEM plates

These parameters are calculated for different configurations of the veto counter. The number of plates is increased from one to a maximum of fifteen.

In Fig. 6.11 all studied configurations are shown with the corresponding plate framed in turquoise. In the configuration where only three plates are used they are either arranged to follow the spine or perpendicular to the spine to cover most of the area above the ribcage. This structure is later extended to encompass the sides. To the three plates along the spine two more plates are added above the ribs to form a cross. The simulations show that in order for the veto counter to be useful and to have any noticeable effect it needs to cover quite a large area behind the patient. One plate alone reduces the random coincidences only by 2.28% while at the same time rejecting 1.19% of true coincidences. The fraction of rejected random coincidences increases with the number of included plates. The number is 6.66% or 7.31% for three plates and 9.73% or 11.81% for five plates in each case depending on the position of the plates. Finally full body coverage leads to 27.72% rejected random coincidences. The number of rejected true coincidences increases simultaneously but never exceeds 5%. The results are plotted in Fig. 6.12 (a) and (b). As a figure of merit the ratio of rejected random to rejected true coincidences can be used. Thus the five plates arranged in a cross is the most efficient configuration (Fig. 6.13). Fig.r̃efhTrueY illustrates where the rejected true (a) and rejected random (b) coincidences are located on the detection plates. Most of the rejected random coincidences lie in the region closest to the chest. This is also the critical region in which most of the random coincidences occur and the signal-to-noise ratio is lowest. The proportion of rejected random to detected random coincidences is almost constant along the x-direction on the plate. The ratio is slightly higher at the far end of the plate (Fig. 6.15). These examples are for the full veto counter when the maximum number of fifteen plates are included.

Table 6.1: Results for different plate configurations of the veto counter

number of veto plates		triple/double	rejected random coincidences	rejected true coincidences	rejected random/ rejected true
1		0.85%	2.28%	1.19%	1.92
3	along the spine	2.53%	6.66%	1.71%	3.89
3	along the ribs	2.64%	7.31%	2.20%	3.32
5	along the ribs	3.52%	9.73%	2.90%	3.36
5	cross	4.24%	11.81%	2.05%	5.76
9		7.29%	21.54%	3.92%	5.50
15		9.42%	27.72%	4.95%	5.60

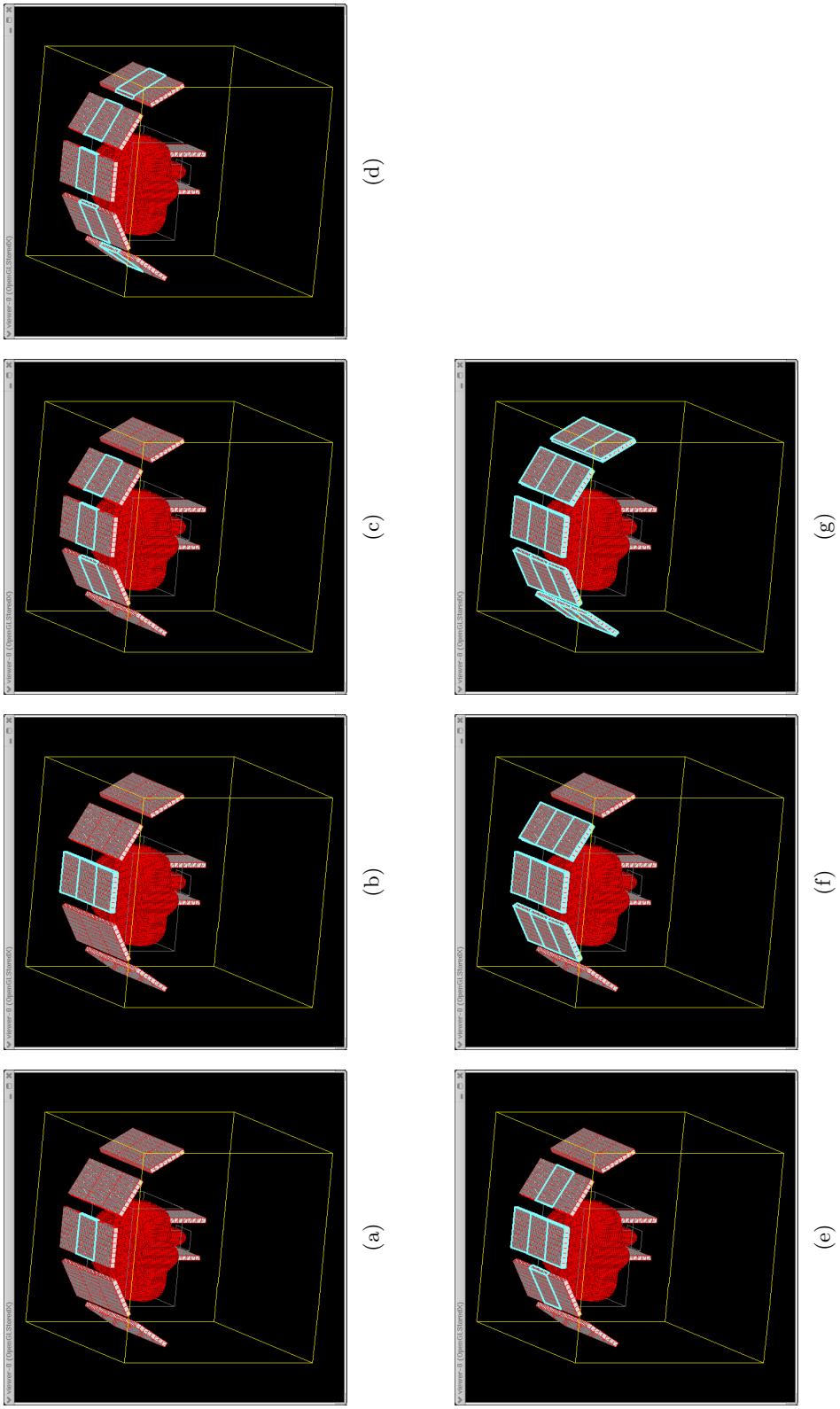

Figure 6.11: Different configurations for the veto counter: 1 plate (a), 3 plates along the spine (b), 3 plates along the ribs (c), 5 plates along the ribs (d), 5 plates in a cross (e), 9 plates (f) and 15 plates (g)

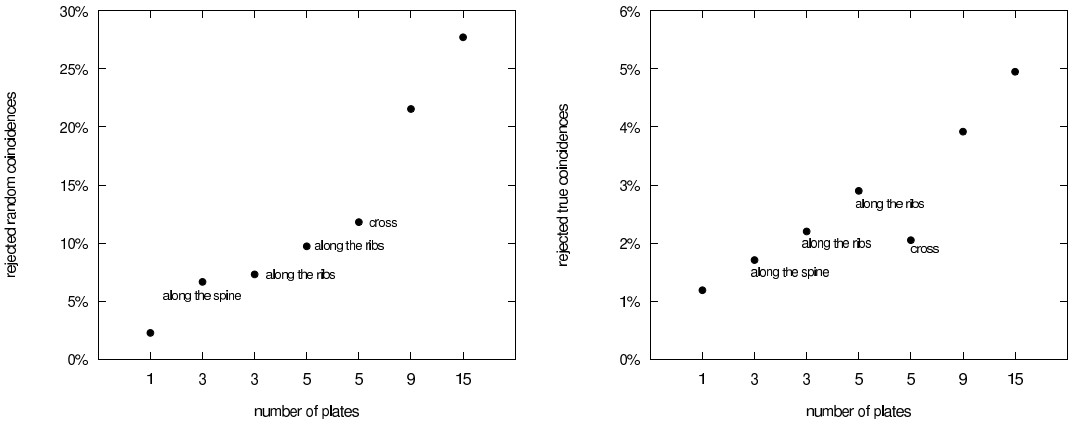

Figure 6.12: Percentage of rejected random (a) and true (b) coincidences as a function of the number of plates in the veto counter

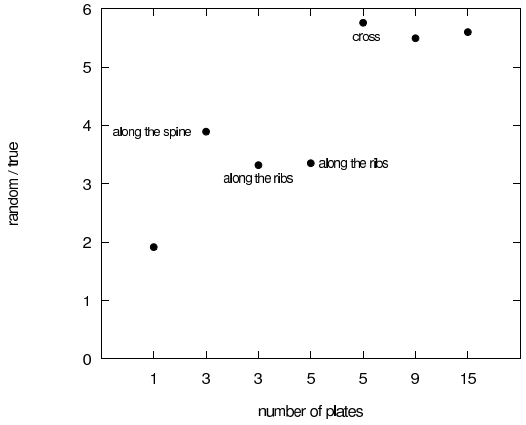

Figure 6.13: Ratio of rejected random over rejected true coincidences as a function of the number of plates in the veto counter

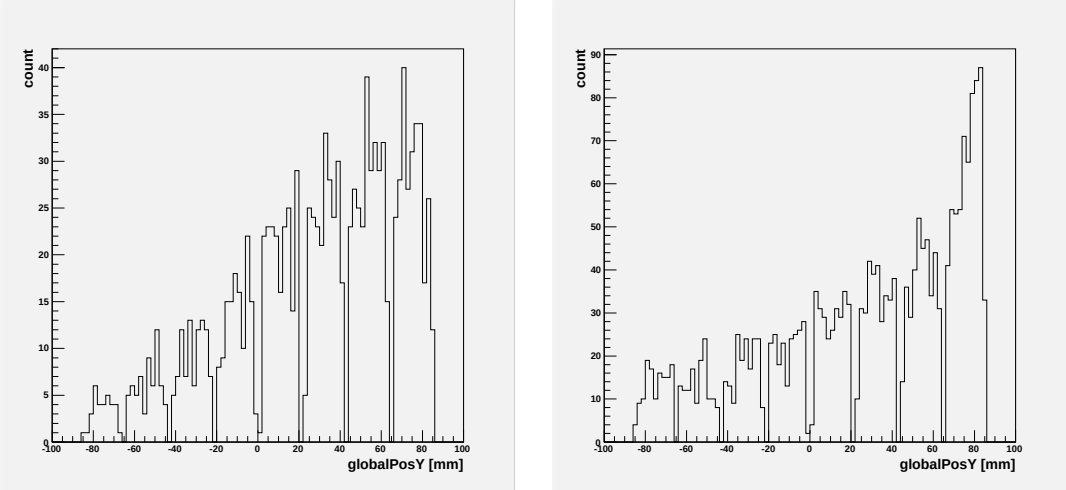

(a) (b)

Figure 6.14: Distribution along the plate of rejected true (a) and random (b) coincidences

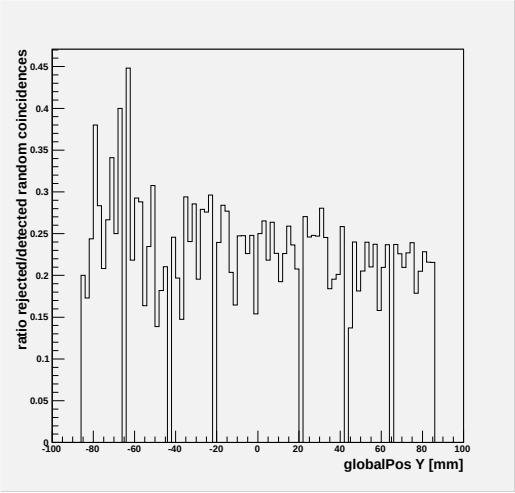

Figure 6.15: Ratio of rejected random coincidences of all detected random coincidences along the detection plates

6.3 Count rate performance

It is important to know what activity to expect in a detector under "real" conditions (detailed patient model and associated activity) to choose the electronics and data acquisition system accordingly. The components have to be able to deal with the expected count rates and not to create unnecessary dead time. Long dead times and an activity that is too high increase the number of random coincidences (cf. 5.3). This decreases the image quality and/or increases the examination time.

The count rate simulations are performed with the NCAT body phantom. The study concentrates on prompt, true, scattered and random coincidences as a function of injected FDG activity. The prompt coincidences are the sum of the true, scattered and random coincidences. The injected FDG activity is varied from 50 MBq up to 3000 MBq in some cases, using the background to organ ratios tabulated in Fig. 5.4. Only 1.34% of the injected activity actually contributes to the detected activity, i.e. 370 MBq injected FDG activity equal 49.6 MBq of total activity in the phantom (sum of organ, tissue and cancer activity). The count rates are used evaluate the changes of detector performance with respect to the length of the coincidence time window, crystal size and dead time.
No dead time is applied to the detector in the first studies. Later 200 ns, 500 ns, 700 ns and 1μs of dead time per plate is included in the simulation. For each dead time value both the paralysable and the non-paralysable dead time models are chosen.

6.3.1 Time window

The distribution of coincidence times of true and random coincidences in Fig. 6.16 (a) illustrates that over 90% of the true coincidences occur in an interval of 2 ns between the first and second photon. A time blurring of 1 ns FWHM of the time of arrival of the photons is assumed in the simulation. Two photons that arrive with a time difference larger than 2 ns are most likely from two different annihilations. Fig. 6.16 (b) shows the true, scattered, random and total coincidence rates as a function of the coincidence time window used in the coincidence sorting algorithm. The curves for the true and scattered coincidences saturates at an value between 2 ns and 3 ns. For larger coincidence windows only random coincidences increase.
It is possible to influence the percentage of random coincidences by varying the length of the coincidence time windows. At present the measured time resolution of the ClearPEM is also around 2 ns at FWHM. This implies an optimum coincidence time window of 4 ns.

6.3.2 Crystal size

The lateral crystal cross section is increased from 2x2 mm^2 to 2.1x2.1 mm^2 and finally to 2.2x2.2 mm^2. 2.2mm is the maximal possible crystal size in order to have still 1 mm

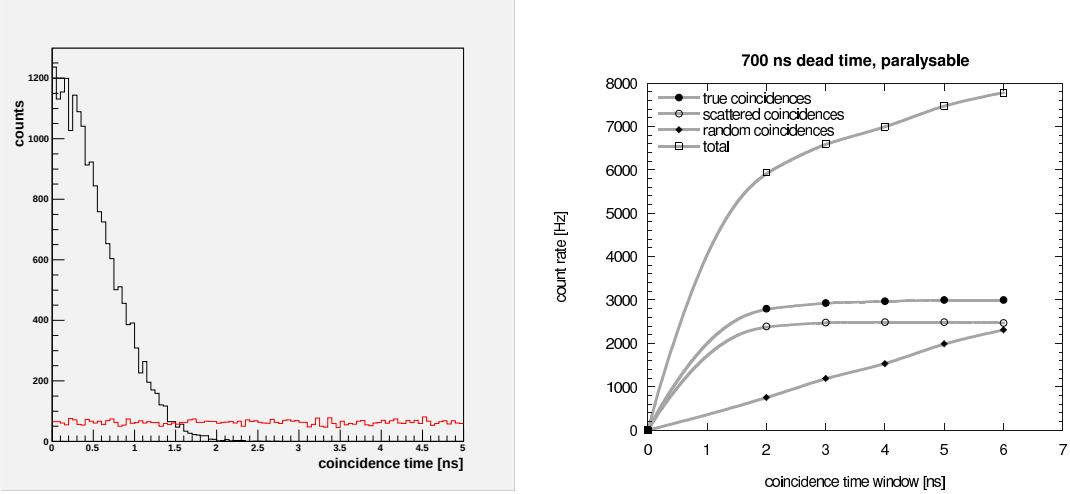

(a) (b)

Figure 6.16: Distribution of the coincidence times of true coincidences (black) and random coincidences (red) (a) and true, scattered, random and total coincidence count rates as a function of the coincidence time window with an injected FDG activity of 370 MBq and 700 ns paralysable dead time(b)

of reflector material between the pixels in a crystal matrix (cf. Fig. 1.10 in 1.6.1). By increasing the crystal cross section the dead space decreases from 36.23 % to 29.69 % to 22.84 % respectively. In a future design just by using slightly bigger crystals the sensitivity can be enhanced.
Consequently the total prompt (Fig. 6.17), true (Fig. 6.18 (a)) and random (Fig. 6.18 (b)) coincidence rates increase with activity and crystal size.

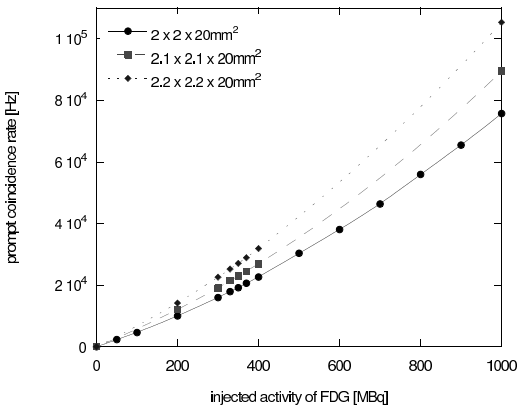

Figure 6.17: Prompt coincidence rate for three different lateral pixel cross sections

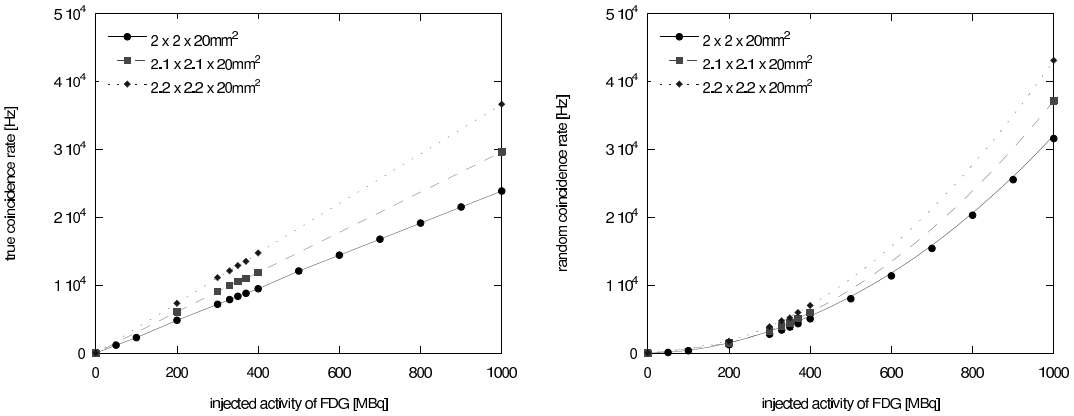

(a) (b)

Figure 6.18: True coincidence count rate (a) and random coincidence count rate (b) for three different lateral pixel cross sections

6.3.3 Noise equivalent count rate

In the subsequent studies dead times of 200 ns, 500 ns, 700 ns and 1 μs are added per plate in the simulation (700 ns is the measured dead time value of the ClearPET system and thus the dead time of the ClearPEM is likely to be in the same range). Both the paralysable and the non-paralysable model are used. The changes to the true and random coincidence count rates can be observed in Fig. 6.19 (a) and (b). It is trivial that the count rates are higher with shorter dead times and also that

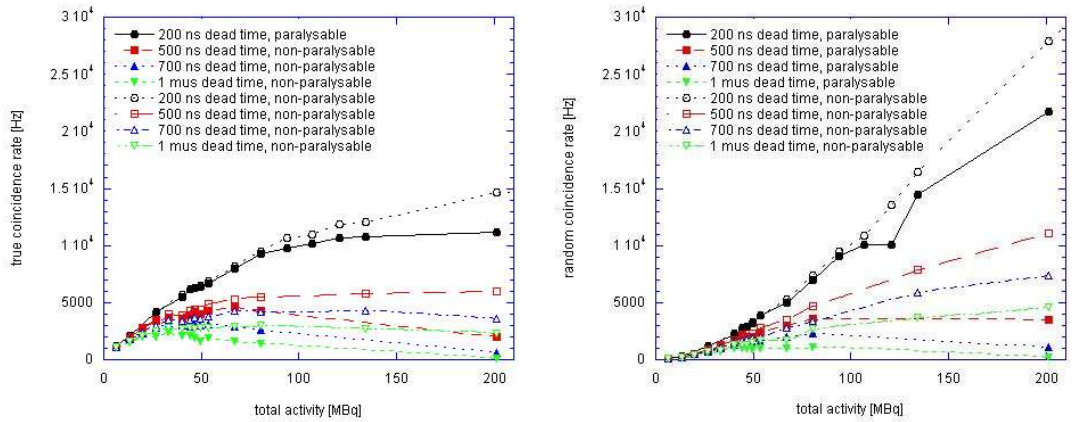

(a) (b)

Figure 6.19: True coincidence (a) and random coincidence (b) count rates for paralysable and non-paralysable dead times (200 ns, 500 ns, 700 ns and 1 μs) as a function of the total activity

the rates are lower with the paralysable dead time model because the dead time is accumulating. The number of true coincidences per second increases until a saturation

point for the simulations in which the non-paralysable dead time model is used. The non-paralysable dead time is responsible for the coincidence rate reaching a maximum and decreasing afterwards. It can also be seen that at a certain activity the random rate surpasses the true coincidence rate. If possible, the activity in the detector area should be kept below this value for an optimal detector performance. The noise equivalent count rates (NECR) (Fig. 6.20) will give a better estimation of the maximum activity. The NECR curves augment sharply until they reach a maximum. For the shortest non-

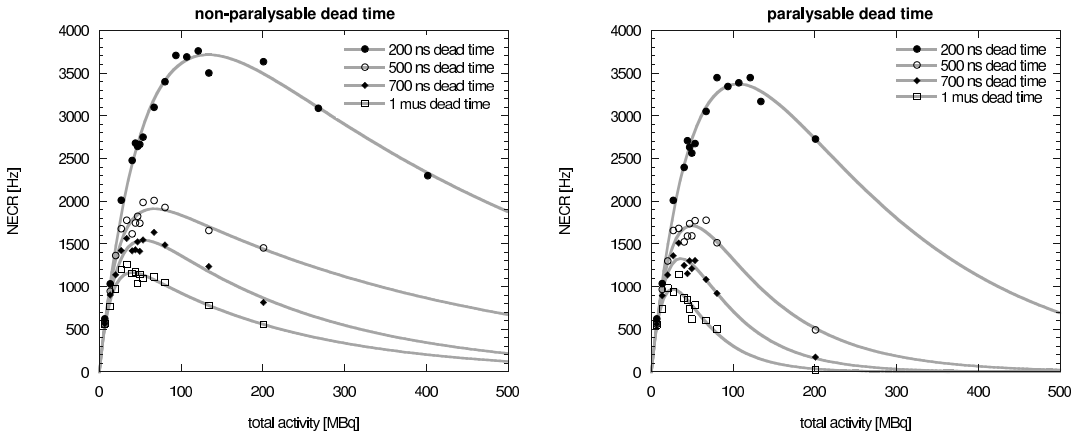

(a) (b)

Figure 6.20: Noise equivalent count rates for non-paralysable (a) and paralysable (b) dead times (200 ns, 500 ns, 700 ns and 1 μs)

paralysable dead time this maximum lies around 120 MBq of total activity (100 MBq for paralysable dead time) which corresponds to 800 MBq (900 MBq) of injected FDG activity. Again the different response functions due to the two dead time models can be observed. With longer dead time values the maximum moves towards lower activity values (Table 6.2). The maximum of the NECR curves corresponds to the activity at

Table 6.2: Total activity corresponding to the maximum of the NECR curves as a function of dead time

dead time [ns]	activity at NECR maximum [MBq]	
	non-paralysable dead time	paralysable dead time
200	120	100
500	60	50
700	50	35
1000	35	20

which the true coincidence rate reaches its maximum and where the true and random count rates becomes equal. To demonstrate this with the example of a dead time of 700 ns the true, scattered and random coincidence rates are plotted in Fig. 6.21 (a) and (b). The scatter fraction at the NECR maximum is 45% and the random fraction

25%. The scatter and random fraction for all simulated cases are shown hereafter. The

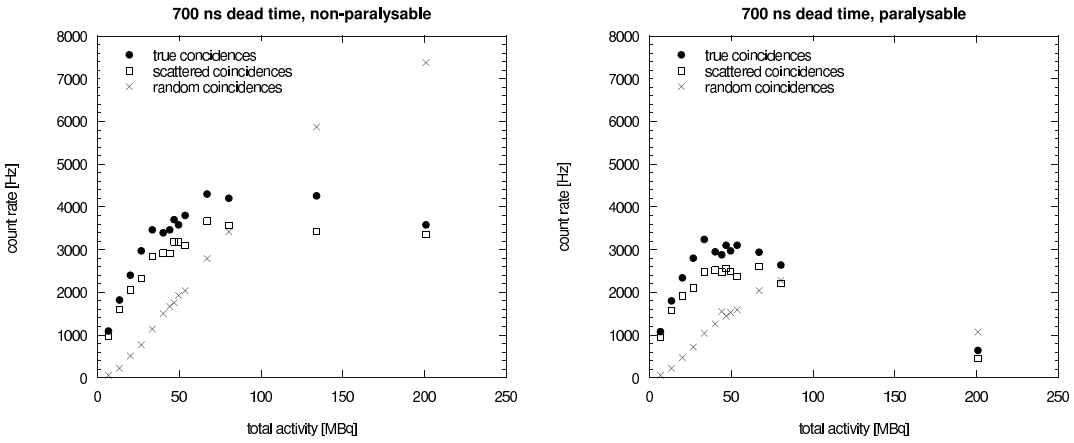

(a) (b)

Figure 6.21: True, scattered and random coincidence count rates for a non-paralysable (a) and a paralysable (b) dead time of 700 ns

scatter fraction in Fig. 6.22 (a) with the whole body phantom of uniform tissue density is fairly constant at 45% over the whole range of activity whereas the random fraction in Fig 6.22 (b) increases. This can only be expected because a higher activity increases the dead time which in turn results in more random coincidences.

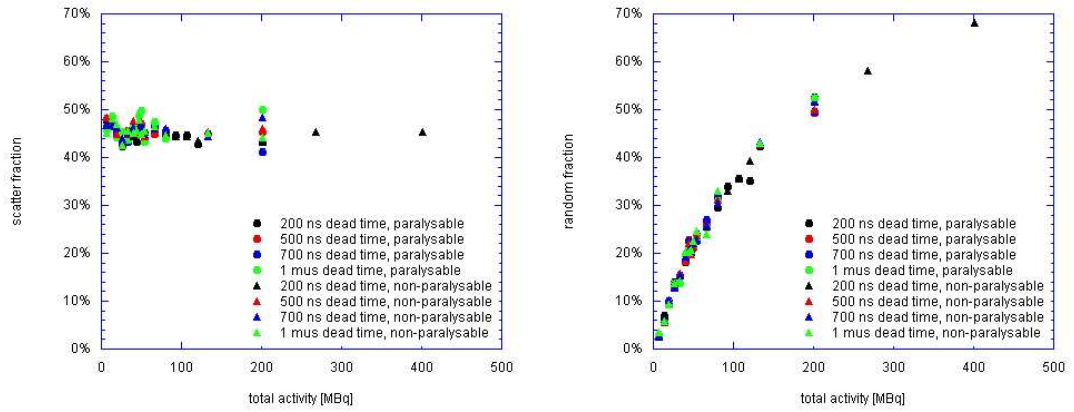

(a) (b)

Figure 6.22: Scatter fraction (a) and random fraction (b) for paralysable and non-paralysable dead times (200 ns, 500 ns, 700 ns and 1 μs) as a function of activity

6.4 Conclusions

In order to incorporate an ultrasound device into the ClearPEM system, changes to its geometry are necessary. It is also agreed that a retention system for the breast is required. Immobilization plates are a first option, but they introduce a break in the symmetry which requires a larger distance between the detector heads for rotation. This reduces the sensitivity and introduces a higher random coincidences and background rate from the body. A symmetric shape might therefore be a better choice for an immobilization system, e.g. a cylinder or cup. The additional material in the detector area has a marginal influence on the sensitivity of the system.

Random coincidences pose a problem to image reconstruction in mammography and cancer detection, especially in the region closest to the chest. A novel concept to reduce this background is a veto counter above the patient's back. The simulation results show that such a system can be effective provided that a large enough area is covered by the veto counter. A 27% reduction of the random background can be achieved with at the same time rejecting only 5% of the true coincidences.

Calculations of the noise equivalent count rates help to understand the detector performance. In the present case it is shown that an activity of more than 120 MBq in the detector with PEM specifications is not desirable. Random coincidences become the dominating fraction of the detected events. To achieve a better performance, the cross section of the crystals can be slightly increased. The importance of timing properties is demonstrated both in the dependence of the NECR on the dead time and the dependence of the number of coincidences on the time window.

Once the prototype of the ClearPEM is finished the results should be compared to real measured data.

There are several possibilities to enhance the performance of the ClearPEM system. A veto counter would work to reduce the amount of random coincidences and thus increase the image quality. The effectiveness depends on the size of the veto counter. A veto counter might be not the right solution for a commercial system. For good coverage a fairly large system would have to been built which would turn out to be too big and heavy and impractical in use. Many scintillation crystal are required which makes a veto counter also very expensive.
A second option for improvement is to ameliorate the timing since good timing resolution has an effect on the random coincidences rate, dead time, examination time and radiation exposure as is shown in this work. Better timing requires faster crystals to shorten the time to accumulate enough photons for integration, better APDs with smaller signal fluctuations and fast electronics which can keep up with the crystals. Components with these specifications exist but at the moment are too expensive to be used in a commercial scanner.

Bibliography

[1] A.Trindade et al, Breast cancer imaging studies by Monte Carlo simulation with Clear-PEM, 2005 IEEE-NSS Conference Record (2005) 2103-2107.

[2] A.Trindade, Estimation of Clear-PEM Counting Rates. Crystal Clear Collaboration Meeting, 3-4 October 2005, Lisboa.

Chapter 7

Summary and Outlook

Positron emission tomography has been proven to be a valuable tool for cancer diagnosis and medical research. Clinical systems are not yet optimized for certain applications due to the coarse spatial resolution or the lack of anatomical information. The future of PET lies in dedicated machines with ever better spatial resolution and the combination of two different imaging modalities in one machine.

A lot of research is done to understand the physical and scintillation properties of the crystals, because advances in PET scanner performance cannot be achieved without taking great care of the development and improvement of scintillating materials.
The investigations of scintillating materials, in particular LuAP and LuYAP crystals, in this thesis have shown several things: the production process of these crystals plays an important role in the determination of their properties. Light yield, time constants and most importantly internal absorption can differ significantly between crystals from different manufacturing companies.
The influence of cerium on the crystal properties is now better understood. Adding cerium increases the light yield and reduces the decay time.
By depolishing only two sides of a LuAP crystal it is possible to measure the depth of interaction with a precision better than 2 mm. This precision can be further improved by depolishing two additional faces although it is not yet clarified if the remaining light yield is high enough. The best compromise between the various scintillation properties has yet to be found.

Two new trends are emerging in medical imaging. Small dedicated PET systems with higher spatial resolution than the existing whole-body PETs and the combination of different imaging modalities into one machine. The Crystal Clear Collaboration is pursuing both directions. On one side a dedicated PET scanner for mammography, the ClearPEM is being built and on the other side the ClearPEN Sonic project - a PET/ultrasound device.
In this thesis the ClearPEM has been studied in computer simulations. Ways to im-

prove the image quality of the mammograph by reducing the background noise with a veto counter above the patient's back have been also investigated. A proof of principle of the veto counter has been given in this thesis. A random background reduction of 27% can be achieved.
Preliminary investigations to modifications of the ClearPEM design to accommodate an ultrasound probe and breast fixation system show that Immobilization plates demand a widening of the detection plates to allow for rotary motion. This leads to a decreased sensitivity. The best option would be a cylindrically symmetric holder, like a cup or cone.
Both ClearPEM projects are well under way. In the next months the clinical trial of the ClearPEM will start in Portugal and the ClearPEM Sonic has been approved in the frame of Cerimed, the European Centre for Research in Medical Imaging which has been newly founded in Marseille, France.

Appendix A

Detailed results on scintillator crystals

Table A.1: Average values of the density, light yield, energy resolution, decay time and transmission for LuAP and LuYAP crystal from IPR, PML and BTCP

		LuAP IPR		LuAP PML	LuYAP IPR	LuYAP PML	LuYAP BTCP
		March 04	June 04				
Size [mm]		2 x 2 x 8	2 x 2 x 8	2 x 2 x 8	2 x 2 x 8	2 x 2 x 10	2 x 2 x 10
Density [g/cm^3]		8.24±0.06	8.33±0.04	8.40±0.04	7.44±0.03	7.21±0.02	7.08±0.04
Light yield [ph/MeV]	vertical	4591±845	4876±877	5054±495	5456±905	4490±410	3200±700
	horizontal	7587±1392	7161±1063	8920±325	9434±1663	9294±721	8100±690
Ratio v/h		60.7±4.3%	67.9±5.2%	56.9±5.4%	58.4±6.7%	48.4±4.1%	39.4±7.0%
Energy resolution	vertical	16.3±2.7%	17.3±1.0%	14.2±1.3%	12.7±1.0%	13.8±0.9%	18.8±3.6%
	horizontal	14.2±3.4%	15.8±5.4%	7.9±0.8%	11.2±1.2%	8.0±0.9%	10.4±1.8%
Decay time [ns]	$t1$	17.5±1.1	18.5±1.0	18.4±0.5	21.2±1.1	21.9±0.7	22.0±1.2
	$t2$	131.3±56.4	163.0±76.9	181.8±46.1	187.3±26.1	188.4±21.9	186.0±11.3
Intensity	$F1$	74.9±5.4%	79.7±3.1%	81.7±1.6%	51.4±5.9%	53.9±5.8%	39.2±2.5%
	$F2$	25.1±5.4%	20.3±3.1%	18.4±1.6%	48.5±5.8%	46.1±5.7%	60.8±5.4%
Cut-off wavelength [nm]	longitudinal	333.9±4.2	333.5±1.1	338.2±1.7	331.8±1.2	348.2±3.4	345.9±5.4
	transversal	-	327.6±0.4	329.8±0.4	326.9±1.5	331.9±2.0	-

Note that for three LuYAP crystals the Cerium concentration was not known, but rather estimated: the 3 crystals marked with a *, were known to be of different Ce-concentrations (0.16%, 0.20%, 0.24%), but not the matching sample IDs, so the correspondency is assumed from the results of the light yield measurements.

Table A.2: Cerium concentrations and average values of the light yield, decay time and transmission for LuAP and LuYAP crystals from IPR

Sample	Ce content	Light yield [ph/MeV]			Decay time [ns]		Cut-off wavelength [nm]	
		vertical	horizontal	ratio v/h	$t1$	$t2$	longitudinal	transversal
LuAP	0.22-0.23%	3952±465	6647±235	59.4±4.9%	19.1	192.0	332.4±0.5	-
	0.23-0.25%	4325±565	6319±414	68.2±5.0%	18.7±1.2	175.1±95.7	332.5±0.4	327.4±0.5
	0.26-0.28%	4991±723	6877±729	72.4±3.0%	18.3±0.3	160.8±10.8	333.2±0.8	327.8±0.2
	0.29-0.33%	5663±526	8519±100	66.5±6.9%	18.5	140.8	334.3±0.4	-
	0.38-0.42%	5746±639	8341±718	68.8±3.0%	17.2±0.1	95.0±26.8	334.0±1.1	-
LuYAP	0.16%*	4458	7114	62.7%	20.7	212.9	330.2	324.9
	0.20%*	4784	7734	61.9%	23.1	217.6	330.6	325.0
	0.22%	5393±1146	8425±1791	64.0±1.3%	21.0±0.9	188.6±24.6	331.1±1.4	326.3±1.7
	0.24%*	5503	9081	60.6	22.7	207.6	331.6	326.3
	0.35%	5195±152	9991±539	52.3±4.2%	21.2±1.1	189.3±29.7	332.3±0.4	327.4±0.5
	0.44%	6320±1104	11345±199	55.7±9.7%	20.4±0.3	158.6±4.0	333.0±0.1	328.5±0.1

Table A.3: Averaged values of the depth of interaction resolution, effective photon attenuation length and energy resolution for LYSO and LuAP crystal with different number of depolished faces

Crystal	number of depolished surfaces	DOI resolution [mm]	effective photon attenuation length λ_{eff} [mm]	energy resolution
LuAP 1779	0	3.37 ± 0.16	36.62 ± 12.1	27.6 ± 1.5 %
	1	2.66 ± 0.36	26.09 ± 2.5	31.4 ± 5.2 %
	2	1.71 ± 0.14	17.81 ± 0.3	28.7 ± 3.4 %
	3	1.68 ± 0.35	14.23 ± 1.0	30.8 ± 2.6 %
	4	1.33 ± 0.25	10.80 ± 0.4	25.7 ± 3.4 %
LYSO 1011	4	1.54 ± 0.11	21.27	20.0 ± 2.1 %
LYSO 1120	1	3.16 ± 0.15	41.72	23.0 ± 1.2 %
LYSO 7070	0	3.55 ± 0.16	47.85 ± 11.2	22.5 ± 3.1 %
	1	2.71 ± 0.11	33.52 ± 1.5	23.6 ± 1.4 %
	2	1.62 ± 0.10	21.45 ± 0.9	22.4 ± 1.5 %
	3	1.23 ± 0.17	16.40 ± 1.2	22.4 ± 2.8 %
	4	0.91 ± 0.15	12.74 ± 1.1	17.3 ± 2.2 %

Appendix B

Monte Carlo simulations

Table B.1: Stored variables and their meaning for the cylindricalPET geometry

variable	description
runID	ID number of the run
eventID	ID number of the positron decay (two photons have the same event ID if the originate from the same positron annihilation
gantryID	ID number of the gantry in which the photon is detected
rsectorID	ID number of the rsector in which the photon is detected
moduleID	ID number of the module in which the photon is detected
submoduleID	ID number of the submodule in which the photon is detected
crystalID	ID number of the crystal in which the photon is detected
layerID	ID number of the layer in which the photon is detected
sourceID	ID number of the source from which the positron originates
sourcePosX	x-coordinate of he position of the annihilation in world referential
sourcePosY	y-coordinate of he position of the annihilation in world referential
sourcePosZ	z-coordinate of he position of the annihilation in world referential
time	time stamp of the single (time of detection)
energy	deposited energy in the crystal
globalPosX	x-coordinate of he position of the detection in world referential

Table B.1: (continued)

variable	description
globalPosY	y-coordinate of he position of the detection in world referential
globalPosZ	z-coordinate of he position of the detection in world referential
comptonPhantom	number of Compton interactions in the phantom before reaching the detector
comptonCrystal	number of Compton interactions in the crystal before detection
RayleighPhantom	number of Rayleigh interactions in the phantom before reaching the detector
RayleighCrystal	number of Rayleigh interactions in the phantom before detection
axialPos	axial position of the scanner (for moving scanner)
rotationAngle	angular position of the scanner (for rotating scanner)
comptVolName	name of the part of the detector where a Compton interaction occurs
RayleighVolName	name of the part of the detector where a Rayleigh interaction occurs

B.1 A complete example of a ClearPEM simulation

concentric_main.mac

```
/control/verbose 2
/random/resetEngineFrom
    /afs/cern.ch/user/j/jtrummer/gate/gate_v2.1.0/
    randoms/endOfRun_4job1.rndm
/control/execute /afs/cern.ch/user/j/jtrummer/gate/gate_v2.1.0/
    ClearPEM/scanner/scanner_vis.mac
/tracking/storeTrajectory 1
/gate/geometry/enableAutoUpdate
/control/execute /afs/cern.ch/user/j/jtrummer/gate/gate_v2.1.0/
    ClearPEM/scanner/concentric_scanner.mac
/control/execute /afs/cern.ch/user/j/jtrummer/gate/gate_v2.1.0/
    ClearPEM/voxel_ascii_phantom_breast.mac
/control/execute /afs/cern.ch/user/j/jtrummer/gate/gate_v2.1.0/
    ClearPEM/voxel_ascii_phantom_body.mac
```

```
/control/execute /afs/cern.ch/user/j/jtrummer/gate/gate_v2.1.0/
    ClearPEM/ClearPEM_physics.mac

/run/initialize

/control/execute /afs/cern.ch/user/j/jtrummer/gate/gate_v2.1.0/
    ClearPEM/scanner/scanner_digi.mac

/gate/systems/scanner/describe

/control/execute /afs/cern.ch/user/j/jtrummer/gate/gate_v2.1.0/
    ClearPEM/scanner/scanner_out1.mac

#/control/execute /afs/cern.ch/user/j/jtrummer/gate/gate_v2.1.0/
    ClearPEM/scanner/source_fluor_1to10.mac
/control/execute /afs/cern.ch/user/j/jtrummer/gate/gate_v2.1.0/
    ClearPEM/scanner/source_fluor.mac
/control/execute /afs/cern.ch/user/j/jtrummer/gate/gate_v2.1.0/
    ClearPEM/voxel_ascii_source_breast.mac
/control/execute /afs/cern.ch/user/j/jtrummer/gate/gate_v2.1.0/
    ClearPEM/voxel_ascii_source_body.mac

/gate/source/fdg/gps/centre 0. 0.5 0. cm

/gate/application/setTimeSlice 1. s
/gate/application/setTimeStart 0. s
/gate/application/setTimeStop 1. s

/gate/application/startDAQ

exit
```

scanner_vis.mac

```
#OpenGLX
/vis/open OGLSX
#/vis/open DAWNFILE
/vis/viewer/reset
/vis/viewer/set/viewpointThetaPhi 45 45
/vis/viewer/zoom 10
/vis/viewer/set/style surface

/vis/drawVolume
/tracking/storeTrajectory 1
/vis/scene/endOfEventAction accumulate
/gate/geometry/enableAutoUpdate
```

concentric_scanner.mac

```
#W O R L D
/gate/world/geometry/setXLength 800. cm
```

```
/gate/world/geometry/setYLength 800. cm
/gate/world/geometry/setZLength 800. cm
/gate/world/setMaterial Air

#/control/execute /afs/cern.ch/user/j/jtrummer/gate/gate_v2.1.0/
    ClearPEM/source_container.mac

#S Y S T E M
/gate/world/daughters/name cylindricalPET
/gate/world/daughters/insert cylinder
/gate/cylindricalPET/setMaterial Air
/gate/cylindricalPET/geometry/setRmax 160. mm
/gate/cylindricalPET/geometry/setRmin 65. mm
/gate/cylindricalPET/geometry/setHeight 172.8 mm
/gate/cylindricalPET/vis/forceWireframe

#R S E C T O R
/gate/cylindricalPET/daughters/name plate
/gate/cylindricalPET/daughters/insert box
/gate/plate/placement/setTranslation 7.6 0 0 cm
/gate/plate/geometry/setXLength 20. mm
/gate/plate/geometry/setYLength 172.8 mm
/gate/plate/geometry/setZLength 152.4 mm
/gate/plate/setMaterial Air
/gate/plate/vis/setColor cyan
/gate/plate/vis/forceWireframe

#M O D U L E
/gate/plate/daughters/name matrix
/gate/plate/daughters/insert box
/gate/matrix/geometry/setXLength 20. mm
/gate/matrix/geometry/setYLength 20.60 mm
/gate/matrix/geometry/setZLength 11.7 mm
/gate/matrix/setMaterial Air
/gate/matrix/vis/setColor red
/gate/matrix/vis/forceWireframe

#S U B M O D U L E
/gate/matrix/daughters/name teflon
/gate/matrix/daughters/insert box
/gate/teflon/geometry/setXLength 20. mm
/gate/teflon/geometry/setYLength 18.12 mm
/gate/teflon/geometry/setZLength 9.22 mm
/gate/teflon/setMaterial BASO
/gate/teflon/vis/setColor white
/gate/teflon/vis/forceSolid

#C R Y S T A L
/gate/teflon/daughters/name scint
/gate/teflon/daughters/insert box
```

```
/gate/scint/geometry/setXLength 20. mm
/gate/scint/geometry/setYLength 2. mm
/gate/scint/geometry/setZLength 2. mm
/gate/scint/setMaterial LYSO
/gate/scint/vis/forceSolid
/gate/scint/vis/setColor yellow

#R E P E A T S C I N T
/gate/scint/repeaters/insert cubicArray
/gate/scint/cubicArray/autoCenter true
/gate/scint/cubicArray/setRepeatNumberX 1
/gate/scint/cubicArray/setRepeatNumberY 8
/gate/scint/cubicArray/setRepeatNumberZ 2
/gate/scint/cubicArray/setRepeatVector 0. 2.3 2.3 mm

/gate/scint/repeaters/insert linear
/gate/scint/linear/setRepeatNumber 2
/gate/scint/linear/setRepeatVector 0 0 4.9 mm

#R E P E A T M A T R I X
/gate/matrix/repeaters/insert cubicArray
/gate/matrix/cubicArray/autoCenter true
/gate/matrix/cubicArray/setRepeatNumberX 1
/gate/matrix/cubicArray/setRepeatNumberY 8
/gate/matrix/cubicArray/setRepeatNumberZ 12
/gate/matrix/cubicArray/setRepeatVector 0. 21.6 12.7 mm

#R E P E A T P L A T E S
/gate/distributions/name radial_deltas_table
/gate/distributions/insert Manual
/gate/distributions/radial_deltas_table/addPoint 50 mm
/gate/distributions/radial_deltas_table/addPoint 280 mm

/gate/distributions/name radial_nof_table
/gate/distributions/insert Manual
/gate/distributions/radial_nof_table/addPoint 2
/gate/distributions/radial_nof_table/addPoint 12

/gate/distributions/name first_angles_table
/gate/distributions/insert Manual
/gate/distributions/first_angles_table/setUnitY deg
/gate/distributions/first_angles_table/addPoint 0
/gate/distributions/first_angles_table/addPoint 0

/gate/plate/repeaters/insert radial
/gate/plate/radial/setDeltaAxis 1 0 0 mm
/gate/plate/radial/setRepeatNofRings 2
/gate/plate/radial/enableAutoRotation true
/gate/plate/radial/setRepeatNumberPerRingTable radial_nof_table
/gate/plate/radial/setFirstAngleTable first_angles_table
/gate/plate/radial/setDeltaAlongAxisTable radial_deltas_table
```

```
#A T T A C H to S Y S T E M
/gate/systems/cylindricalPET/rsector/attach plate
/gate/systems/cylindricalPET/module/attach matrix
/gate/systems/cylindricalPET/submodule/attach teflon
/gate/systems/cylindricalPET/crystal/attach scint

#A T T A C H L E V E L S D
/gate/scint/attachCrystalSD
#/gate/cont/attachPhantomSD
/gate/teflon/attachPhantomSD
#/gate/ell/attachPhantomSD

voxel_ascii_phantom_breast.mac
gate/world/daughters/name ncat_phantom
/gate/world/daughters/insert parameterizedBoxMatrix

/gate/ncat_phantom/geometry/insertReader image
/gate/ncat_phantom/imageReader/insertTranslator range
/gate/ncat_phantom/imageReader/rangeTranslator/readTable
    /afs/cern.ch/user/j/jtrummer/gate/gate_v2.1.0/ClearPEM/range.dat
/gate/ncat_phantom/imageReader/rangeTranslator/describe 1
/gate/ncat_phantom/imageReader/readFile
/afs/cern.ch/user/j/jtrummer/ncat/m000-Uint32-
    cl_64_breast_only_act_av.dat
/gate/ncat_phantom/placement/setTranslation 0. 2.6 0. cm

#/gate/ncat_phantom/placement/setRotationAxis 1 0 0
#/gate/ncat_phantom/placement/setRotationAngle 270 deg

/gate/ncat_phantom/attachVoxelPhantomSD
#/gate/ncat_phantom/addOutput doseOutput
#/gate/output/doseOutput/saveUncertainty true
#/gate/ouput/doseOutput/setFileName ncat_paraDose.bin

range.dat
2
0 0 Air false 0.0 0.0 0.0 0.0
1 5 Breast true 1.0 0.0 0.0 0.0

m000–Uint32-cl_64_breast_only_act_av.dat

voxel_ascii_phantom_body.mac
/gate/world/daughters/name ncat_phantom2
/gate/world/daughters/insert parameterizedBoxMatrix

/gate/ncat_phantom2/geometry/insertReader image
/gate/ncat_phantom2/imageReader/insertTranslator range
/gate/ncat_phantom2/imageReader/rangeTranslator/readTable
/afs/cern.ch/user/j/jtrummer/gate/gate_v2.1.0/ClearPEM/range.dat
/gate/ncat_phantom2/imageReader/rangeTranslator/describe 1
/gate/ncat_phantom2/imageReader/readFile
```

```
/afs/cern.ch/user/j/jtrummer/ncat/m000-Uint32-
    cl_64_body_only_act_av.dat
/gate/ncat_phantom2/placement/setTranslation 0. 20. 0. cm

#/gate/ncat_phantom2/placement/setRotationAxis 1 0 0
#/gate/ncat_phantom2/placement/setRotationAngle 270 deg

/gate/ncat_phantom2/attachVoxelPhantomSD
#/gate/ncat_phantom2/addOutput doseOutput
#/gate/output/doseOutput/saveUncertainty true
#/gate/ouput/doseOutput/setFileName ncat_paraDose.bin

range.dat

m000-Uint32-cl_64_body_only_act_av.dat
```

ClearPEM_physics.mac

```
#P H Y S I C S
/gate/physics/gamma/selectCompton standard
/gate/physics/gamma/selectPhotoelectric standard
/gate/physics/gamma/selectRayleigh inactive
/gate/physics/setXRayCut 1 GeV
/gate/physics/setDeltaRayCut 1 GeV
/gate/physics/setElectronCut 30 m
```

scanner_digi.mac

```
#D I G I T I Z E R
/gate/digitizer/convertor/verbose 0
/gate/digitizer/Singles/insert adder
/gate/digitizer/Singles/adder/verbose 0
#readout
/gate/digitizer/Singles/insert readout
/gate/digitizer/Singles/readout/setDepth 2
/gate/digitizer/Singles/readout/verbose 0
#upper and lower threshold
/gate/digitizer/Singles/insert thresholder
/gate/digitizer/Singles/thresholder/setThreshold 300. keV
/gate/digitizer/Singles/insert upholder
/gate/digitizer/Singles/upholder/setUphold 700. keV
/gate/digitizer/Singles/thresholder/verbose 0
#coincidence sorter
/gate/digitizer/name Coincidences
/gate/digitizer/insert coincidenceSorter
/gate/digitizer/Coincidences/setWindow 4. ns
/gate/digitizer/Coincidences/minSectorDifference 1
```

```
/gate/digitizer/Coincidences/MultiplesPolicy takeAllGoods
```

scanner_out1.mac

```
#O U T P U T
#root
/gate/output/root/setFileName scanner_output_job1
/gate/output/root/setRootNtupleFlag 0
/gate/output/root/setRootHitFlag 0
/gate/output/root/setRootSinglesFlag 1
/gate/output/root/setRootCoincidencesFlag 1
/gate/output/root/setSaveRndmFlag 0

#ascii
/gate/output/ascii/disable
/gate/output/ascii/setOutFileHitsFlag 0
/gate/output/ascii/setOutFileCoincidencesFlag 0

#lmf
/gate/output/lmf1/disable
```

source_fluor_1to10.mac

```
#F L U O R
/gate/source/addSource fdg
/gate/source/fdg/setActivity 20145 Bq
/gate/source/fdg/gps/particle e+
/gate/source/fdg/setForcedUnstableFlag true
/gate/source/fdg/setForcedHalfLife 6586 s
/gate/source/fdg/gps/energytype Fluor18
/gate/source/fdg/gps/angtype iso

/gate/source/list
```

voxel_ascii_source_breast.mac

```
#A S C I I S O U R C E
/gate/source/addSource ncat_source voxel

/gate/source/ncat_source/reader/insert image
/gate/source/ncat_source/imageReader/translator/insert range
/gate/source/ncat_source/imageReader/rangeTranslator/readTable
/afs/cern.ch/user/j/jtrummer/gate/gate_v2.1.0/ClearPEM/activityRange.dat
/gate/source/ncat_source/imageReader/rangeTranslator/describe 1
/gate/source/ncat_source/imageReader/readFile
```

```
/afs/cern.ch/user/j/jtrummer/ncat/m000-Uint32-
    cl_64_breast_only_act_av.dat

/gate/source/ncat_source/setPosition -4.5 -2.65 -6.75 cm

/gate/source/ncat_source/setType backtoback
/gate/source/ncat_source/gps/particle gamma
/gate/source/ncat_source/gps/energytype Mono
/gate/source/ncat_source/gps/monoenergy 511. keV
/gate/source/ncat_source/gps/angtype iso
/gate/source/ncat_source/gps/mintheta 0. deg
/gate/source/ncat_source/gps/maxtheta 180. deg
/gate/source/ncat_source/gps/minphi 0. deg
/gate/source/ncat_source/gps/maxphi 360. deg
/gate/source/ncat_source/gps/confine NULL

/gate/source/ncat_source/dump 1

activityRange.dat
2
0 0 0.
1 5 850.

m000-Uint32-cl_64_breast_only_act_av.dat
```

voxel_ascii_source_body.mac

```
#A S C I I S O U R C E
/gate/source/addSource ncat_source2 voxel

/gate/source/ncat_source2/reader/insert image
/gate/source/ncat_source2/imageReader/translator/insert range
/gate/source/ncat_source2/imageReader/rangeTranslator/readTable
/afs/cern.ch/user/j/jtrummer/gate/gate_v2.1.0/ClearPEM/activityRange.dat
/gate/source/ncat_source2/imageReader/rangeTranslator/describe 1
/gate/source/ncat_source2/imageReader/readFile
/afs/cern.ch/user/j/jtrummer/ncat/m000-Uint32-
    cl_64_body_only_act_av.dat

/gate/source/ncat_source2/setPosition -21.375 8.75 -9. cm

/gate/source/ncat_source2/setType backtoback
/gate/source/ncat_source2/gps/particle gamma
/gate/source/ncat_source2/gps/energytype Mono
/gate/source/ncat_source2/gps/monoenergy 511. keV
/gate/source/ncat_source2/gps/angtype iso
/gate/source/ncat_source2/gps/mintheta 0. deg
/gate/source/ncat_source2/gps/maxtheta 180. deg
/gate/source/ncat_source2/gps/minphi 0. deg
/gate/source/ncat_source2/gps/maxphi 360. deg
/gate/source/ncat_source2/gps/confine NULL
```

/gate/source/ncat_source2/dump 1
activityRange.dat
m000-Uint32-cl_64_body_only_act_av.dat

List of Figures

List of Tables

Curriculum vitae

Julia Trummer

date of birth	04.03.1978
nationality	Austrian
address	Axerweg 49 7000 Eisenstadt Austria

education

2004-2007	doctoral thesis in physics as part of the Austrian Doctoral Students program at CERN, Geneva, Switzerland and the Vienna University of Technology, Vienna, Austria "Study of a Positron Emission Mammograph"
10/2004	Diplom Ingenieur (master degree in physics) "Untersuchungen zur Bioverträglichkeit von Metall-Metall Hüft-Totalendoprothesen mittels elektrochemischer Impedanzspektroskopie"
1996-2004	diploma studies in physics at the Vienna University of Technology, Vienna, Austria
2001-2002	Universite Paul Sabatier, Toulouse III as part of the ERASMUS student exchange program
05/1996	Matura, Gymnasium der Diözese Eisenstadt, Austria (A levels)

work

11/2006	CERN, Geneva, Switzerland "Comparison of irradiated epitaxial silicon detectors from different producers"
04-05/2003	Vienna University of Technology, Vienna, Austria "Haftfestigkeitsmessungen und Wachszugversuche"
04-06/2002	Service National des Champs Magnetiques Pulses (SNCMP), Toulouse, France "Oscillations rapides de la magnetoresistance du sel du Bechgaard $(TMTSF)_2NO_3$"
07-08/2001	SIEMENS PSE, Austria Visual Basic programming
06-07/2000	International Atomic Energy Agency (IAEA) "Nuclear threat factor calculations"

publications

- C.Wolner, G.Nauer, J.Trummer, V.Putz, S.Tschegg, Possible reasons for the unexpected bad biocompatibility of metal-on-metal hip implants. Mater Sci Eng C 26 (2006) 34.

- J.Trummer, E.Auffray, P.Lecoq, A.Petrosyan, P.Sempere-Roldan, Comparison of LuAP and LuYAP crystal properties from statistically significant batches produced with two different growth methods. Nucl Instr and Meth A 551 (2005) 339.

- J. Trummer, D. Aimard, E. Auffray, G. Chevenier, C. Laffay, P. Lecoq, P. Sempere-Roldan, O. Teller, Scintillation Properties of LuYAP and LYSO Crystals Measured with MiniACCOS, an Automatic Quality COntrol System. IEEE NSS Conf Rec (2005) 2807.